UNIVERSITÀ DEGLI STUDI DI PAVIA
DOTTORATO DI RICERCA IN FISICA – XXXVI CICLO

GENERATOR PRODUCTION OF ^{155}TB WITH NATURAL TARGETS

Alessandro Colombi

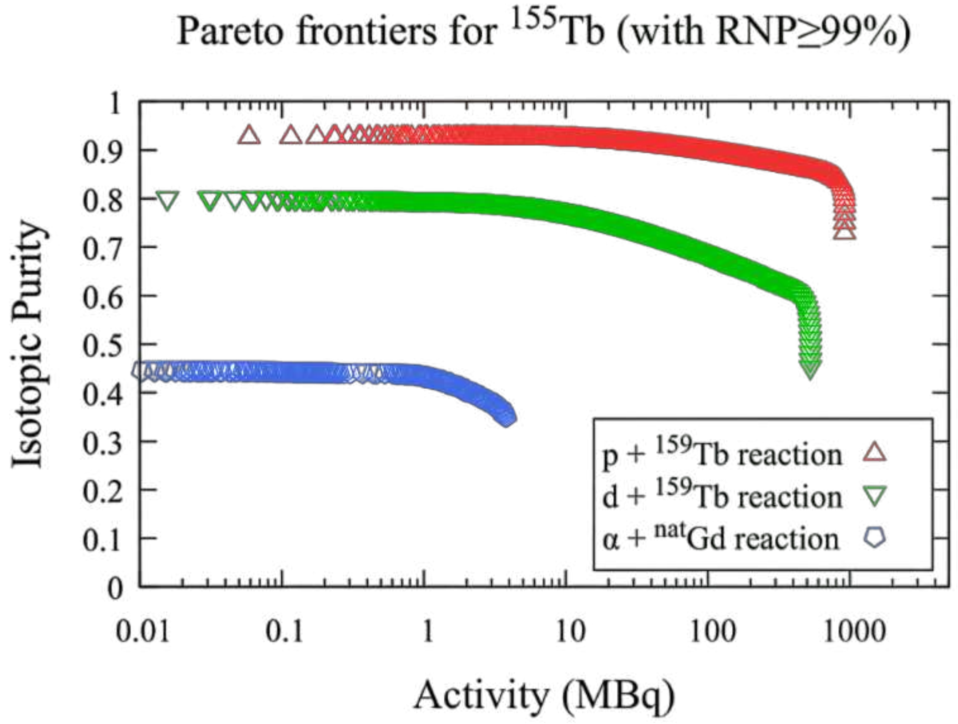

Tesi per il conseguimento del titolo

Full Title:
Generator production of ^{155}Tb with natural targets

Alessandro Colombi
December 2023

Università degli Studi di Pavia
Dipartimento di Fisica

DOTTORATO DI RICERCA IN FISICA – XXXVI CICLO

GENERATOR PRODUCTION OF ^{155}TB WITH NATURAL TARGETS

dissertation submitted by
Alessandro Colombi

Submitted to the Graduate School of Physics in partial fulfilment of the requirements for the degree of
DOTTORE DI RICERCA IN FISICA
DOCTOR OF PHILOSOPHY IN PHYSICS

Supervisors: Dr. Andrea Fontana (National Institute for Nuclear Physics – Section of Pavia)
Prof. Francesca Ballarini (University of Pavia)

Referee: Prof. Lembit Sihver (Vienna University of Technology)

Referee: Prof. Vincenzo Patera (Sapienza – University of Rome)

Cover: Graphical abstract of the thesis. Pareto frontiers of the three indirect reactions for ^{155}Tb production: the data points indicate all the solutions of the simultaneous optimization of activity and isotopic purity of ^{155}Tb, considering different irradiation and cooling configurations and the constraint RadioNuclidic Purity ≥ 99%.

Generator production of ^{155}Tb with natural targets
Alessandro Colombi
PhD thesis - University of Pavia
Pavia, Italy, December 2023

Contents

List of Abbreviations ix

Introduction 1

1 Theranostics and terbium 5
- 1.1 The Swiss Army knife for nuclear medicine 7
- 1.2 Why ^{155}Tb? SPECT and Auger therapy 9
  - 1.2.1 SPECT: definition, functioning and innovations 9
  - 1.2.2 Auger therapy 14
- 1.3 The INFN REMIX project 15
- 1.4 Review of experimental data 19

2 Nuclear reaction modeling for Tb production 27
- 2.1 Theory: optical potential, direct reactions, compound nucleus and pre-equilibrium processes 27
- 2.2 Models: the TALYS code 35
  - 2.2.1 Numerical considerations: energy binning 37
  - 2.2.2 Physical considerations on the different nuclear processes 38
- 2.3 A Monte Carlo approach: the PHITS code 45
- 2.4 Production studies 46
  - 2.4.1 Production rates and Bateman equations 47
  - 2.4.2 Yields and purities 51

3 Cross section results 55
- 3.1 Reactions with protons 56
- 3.2 Reactions with deuterons 69
- 3.3 Reactions with α particles 77

4 Production studies of ^{155}Tb 85
- 4.1 Chemical separation model 85
  - 4.1.1 Energies for the production rate 86
  - 4.1.2 Decay schemes and processing times for Bateman equations 87

4.2 Yield and purities optimization 94
4.2.1 Pareto frontier 97

5 Comparative analysis of optimized ^{155}Tb production routes 105
5.1 Comparison with standard calculations 105
5.2 A promising reaction for ^{155}Tb production? 107
5.2.1 Comparison of generators 107
5.2.2 Comparison with direct production on enriched targets . 109
5.3 Additional analysis in a realistic scenario 111

Conclusions 115

Appendix A 117

Appendix B 122

Bibliography 133

Ringraziamenti 145

List of abbreviations

CERN	European Council for Nuclear Research
CT	Computed Tomography
DWBA	Distorted Wave Born Approximation
EC	Electron Capture
EOB	End Of Bombardment
FDA	U.S. Food and Drug Administration
FI	Fluorence Imaging
FLUKA	Fluctuating Cascade
GDH	Geometry Dependent Hybrid
GEANT4	GEometry And Tracking
GEM	Generalized Evaporation Model
HFM	Hartree-Fock Method
IAEA	International Atomic Energy Agency
INCL	Intra-Nuclear Cascade of Liège
INFN	National Institute for Nuclear Physics
LNL	National Laboratories of Legnaro
IP	Isotopic Purity
ISOL	Isotope Separation On Line
ISOTOPIA	abbreviation for the IAEA Medical Isotope Browser
IT	Isomeric Transition
JAEA	Japanese Atomic Energy Agency
JENDL	Japanese Evaluated Neutron Data Library
JLM	Jeukenne Lejeune Mahaux
KD	Koning-Delaroche

KEK	High Energy Accelerator Research Organization
LARAMED	LAboratory of RA-dioisotopes for MEDicine
LET	Linear Energy Transfer
MCNP	Monte Carlo N-Particle
MRI	Magnetic Resonance Imaging
MSC	MultiStep Compound
MSD	MultiStep Direct
NCA	No-Carrier Added
PET	Positron Emission Tomography
RBE	Relative Biological Effectiveness
REMIX	Research on Emerging Medical radioIsotopes from the X-sections
RIST	Research Organization for Information Science and Technology
RNP	RadioNuclidic Purity
SA	Specific Activity
SPECT	Single Photon Emission Computed Tomography
SPES	Selective Production of Exotic Species
TENDL	TALYS Evaluated Nuclear Data Library

Introduction

Since the discovery of radioactivity, the scientific community has realized the potential applicability of radioisotopes to Nuclear Medicine, both for diagnostic and/or therapeutic purposes. Different applications were soon identified for selected natural radioisotopes, depending on their physical properties, as their half-life and the energy of the particles emitted in the decay (α, β^+, β^-, γ and Auger electrons). The scenario was further enriched by the discovery of artificial radioactivity and by the development of the technologies that led in the following years to nuclear reactors and cyclotrons.

In this context it is interesting that one of the first methods to produce medical radionuclides, namely the radionuclide generator, was invented at the beginning of the last century, even before important studies and developments in Modern Physics, like for example the discovery of the neutron, the development of Quantum Mechanics or the construction of the first cyclotrons. In a generator, the nuclide of interest is obtained from the decay of its parent nucleus with a timing schedule dictated by the natural half-lifes involved: the first generator device was based on the ^{226}Ra/^{222}Rn decay chain and, since the product could be made available each day, it was also named "milk cow".

Nowadays, this production route is referred to as an indirect method and is often presented as a third option alongside the use of nuclear reactors or cyclotrons, which instead allow the direct production of radioisotopes. Radioisotope generators have been developed and contribute to the production of some of the most widely used radionuclides, such as the ^{99m}Tc from ^{99}Mo/^{99m}Tc generator, ^{68}Ga from ^{68}Ge/^{68}Ga or ^{90}Y from ^{90}Sr/^{90}Y and many others. Obviously, in these systems, the progenitors of the nuclides of interest are produced using reactors or cyclotrons. The latter are steadily increasing as they allow to overcome certain limitations presented by the use of reactors, like the high costs for the materials and for the reactor maintenance as well as the safety of the involved workers. Great interest is currently devoted to the study of reactions to produce innovative radionuclides using cyclotrons of low energy (typically available in hospitals) or of medium energy (in research centres) and possibly also natural targets, further reducing the target production and enrichment costs.

Recently the attention of the applied nuclear physics community, involving the International Atomic Energy Agency (IAEA), the European Council for Nuclear Research (CERN) and the National Institute for Nuclear Physics (INFN) to cite a few, has been particularly involved in the production of radiopharmaceuticals that can be used in theranostics. This term is the fusion of two words, therapy and diagnosis, and refers to the use of a single molecule carrying particular radionuclides that emit radiation useful both for therapeutic and diagnostic purposes. The use of this new term was firstly reported in 1998 by John Funkhouser, even if already in 1941 the concept of using radioactive iodine (^{131}I), for imaging and treatment of patients with hyperthyroidism and later thyroid cancer, was applied by Saul Hertz. Only later (in 1951) the U.S. Food and Drug Administration (FDA) approved sodium iodide for use in patients with thyroid disease, and from there the investigation of new theranostic nuclides has increased, initially with the use of neutron-induced reactions in nuclear reactors to produce for instance ^{131}I and ^{186}Re. Coming to recent times, charged-particles-induced reactions are prevailing and alternative routes are studied to produce the already established radionuclides as well as new promising ones (like ^{67}Cu and ^{47}Sc) with physical and biological features of great interest for medical applications. For this reason different projects have been proposed by international research groups and an example is given by the project REMIX (Research on Emerging Medical radIonuclides from the X-sections), which has been recently funded by INFN. The project is focused on the production of a variety of different theranostic radionuclides, in particular terbium (Tb) that is a very interesting element. In the periodic table terbium is the only element with four radionuclides (^{149}Tb, ^{152}Tb, ^{155}Tb and ^{161}Tb) that can be used for different purposes in medicine: to perform diagnosis with Positron Emission Tomography (PET) and Single Photon Emission Computed Tomography (SPECT), and therapy with α and β^- particles and with Auger electrons.

This thesis presents how the knowledge of the nuclear reactions and radioactive decay physics is at the foundations of medical radionuclide production. Specifically, a simulation study of the following generator reactions is described to indirectly produce ^{155}Tb (T$_{1/2}$=5.32 d):

$$\begin{aligned} p + {}^{nat}\mathrm{Tb} &\rightarrow {}^{155}\mathrm{Dy} + 5n \rightarrow {}^{155}\mathrm{Tb}, & (1)\\ d + {}^{nat}\mathrm{Tb} &\rightarrow {}^{155}\mathrm{Dy} + 6n \rightarrow {}^{155}\mathrm{Tb}, & (2)\\ \alpha + {}^{nat}\mathrm{Gd} &\rightarrow {}^{155}\mathrm{Dy} + xx \rightarrow {}^{155}\mathrm{Tb}. & (3)\end{aligned}$$

In all cases, by using protons, deuterons and α particles on different natural targets, the aim is to produce ^{155}Dy which, decaying with an half-life T$_{1/2}$=9.9 h, generates the nuclide of interest, ^{155}Tb. All the three reactions have been studied experimentally and the measurements available in literature show that the cross section peak of ^{155}Dy lies in the region from 30 to 70 MeV. Therefore the nuclide has to be produced and studied with an intermediate energy cyclotron, like for example the Selective Production of Exotic Species (SPES) cyclotron of the INFN National Laboratories of Legnaro (INFN-LNL), operating in the range of 35-70 MeV. The reaction represents an opportunity also from the nuclear physics points of view, since new measurements and studies are necessary to identify the optimal conditions for the production of ^{155}Tb with high purity: the number of produced nuclides have to be carefully evaluated, considering the problem of the different channels generated in the reaction and taking into account the radioactive decay chains that also produce contaminants.

In the first chapter, after an introduction to the subject, the description of the terbium nuclides useful in nuclear medicine is presented. The physical principles of the SPECT imaging technique in which ^{155}Tb will find its main use are also reviewed. An overview of the available experimental data for each reaction is also shown to get the first general insights for the theoretical investigation of the three reactions. In particular, new experimental measurements are planned in the REMIX project, but are not available yet and they could not be used to support the calculations. In the second chapter an overview of the theory of nuclear reactions is discussed, with emphasis on the aspects that have been particularly important in this study, namely the optical potential, the rotational effects due to the collective motions of heavy nuclei, the pre-equilibrium process and the nuclear level density of the produced nuclides. Attention is also given to the features provided by the nuclear reaction code TALYS which has been used to obtain the results. In this context the definitions of the important quantities, such as yields and purities, are presented in a general formalism applicable both to direct and indirect productions.

In the last three chapters the original results of the thesis are presented. In particular in Chapter 3, on the basis of the theory presented, an accurate analysis of the cross sections is shown, also with a comparison with standard calculations. Cross section plots are presented and discussed for each reaction and the values of the TALYS parameters found in this study are reported allowing the replicability of the obtained results. In Chapter 4 the results of the calculation of the activities and purities of the final product are presented. A particular methodology to optimize the production of a medical radionuclide is presented for the first time: a multi-criteria analysis is applied to select yield and purities achievable in the optimal conditions for each generator. Different scenarios are explored within the limits posed by the European Pharmacopoeia. For the reactions with protons and α particles, the results are compared with the experimental yields and purities found in the literature in similar conditions. For deuterons, this work represents the first quantitative study for the production of ^{155}Tb. In the last chapter, the three generators are compared among each other and with the direct production route via the (p,n) channel on ^{155}Gd, which is today the only practical way to produce ^{155}Tb in hospitals for clinical use. This allows to find the most promising reaction for the production of ^{155}Tb and to indicate in the conclusions guidelines to optimize the production of ^{155}Tb.

Chapter 1

Theranostics and terbium

In the last years the interest for applications of Nuclear Physics to Medicine has incredibly increased and has provided an effective contribution to help physicians to improve health conditions of cancer patients. The attention has been focused on the study of the effect of ionizing radiation on living systems. In general two are the possible approaches: the use of external radiation, like X rays in radiation therapy or charged particles (protons and other ions as carbon) in hadrontherapy; the use of internal radiation with radioactive nuclides administered to patients. In particular, the production of innovative radioisotopes, which can be obtained by irradiating a target with projectile beams of specific current and energy, has raised the attention of the community [1, 2]. In nuclear medicine radioactive isotopes have represented powerful tools [3] since the discovery of radioactivity thanks to the creation of radiopharmaceuticals. These drugs are mainly composed of a radioactive nucleus which is part of an atom bound to a specific molecule with chemical and biological features to match a targeted cell. Depending on the half-life and on the energies of the emitted particles, the radionuclides can be used in:

- **diagnosis**: to study possible critical pathologies and the metabolic effects of the radionuclides used in therapy, using γ emitters for SPECT (Single Photon Emission Computed Tomography) or also positron emitters for PET (Positron Emission Tomography).
- **therapy** to treat cancer cells using α, β^-, Auger and/or internal conversion electrons.

Among the different techniques used in Nuclear Medicine, the use of radiopharmaceuticals is increasingly growing thanks to the development and improvement of the technologies of nuclear reactors and accelerators applied to the production of radioisotopes. In general, research on new imaging radionuclides involves the investigation of nuclei with radiation similar in energy and intensity to the one of the most common radionuclides already used in clinics. The reasons are mainly two and are related to both imaging and therapy.

Nuclide	$T_{1/2}$	Decay mode	$E_{\beta+}$ (max) (keV)	E_γ (keV) (%)
^{64}Cu	12.7 h	β^+ (17.8)	653	1346.0 (0.53)
^{67}Cu	2.58 d	β^- (100)	577	184.6 (48.6)
^{44g}Sc	3.9 h	β^+ (94.3)	1470	1157 (99.9)
^{47}Sc	3.35 d	β^- (100)	610	159.4 (68)
^{124}I	4.18 d	β^+(22)	2137	602.7 (61)
^{131}I	8.02 d	β^- (100)	607	364.5 (82)

Table 1.1: Main decay data of few theranostic pairs [5].

For diagnostic purposes, the same detectors can be used: some of them (scintillating crystals) are already well established and used thanks to their high detection efficiency and energy resolution of the emitted gamma rays. The most used nuclides are ^{18}F for PET and ^{99m}Tc for SPECT. The properties and use of the latter radionuclide are described in Section 1.2.1. In therapy, radionuclides with similar features (emitted particles and their energies) can induce the same effect after their interaction with matter (tissues and biological structures). In particular, the ionizing radiation interacts with the medium and releases energy, stopping inside it or continuing to travel, depending in general on the incoming energy and on the thickness of the material. From a physical point of view there are two important quantities useful for both external and internal radiotherapy. They are the range of the particle (the average distance travelled by the particle in the medium) and the Linear Energy Trasfer (LET) defined for charged particles as the mean energy loss per unit path length. The latter quantity allows to describe the distribution of the energy released in the tissues. Radionuclides emitting particles with short range and high LET can damage irreversibly the biological structures near the concentration region of the injected radiopharmaceutical. An example of this effect is shown in Section 1.2.2. On another hand, from a biological point of view, a further important and useful quantity (especially used in external radiotherapy) is the Relative Biological Effectiveness (RBE), which is the ratio between the dose of a reference radiation (typically X-rays or γ-rays) and the dose of a radiation of interest, to obtain the same biological effect (isoeffect). It is a dimensionless quantity that requires the specification of the type of radiation, of the type of the target cell/organ and of the biological endpoint (DNA strand breaks, mutations, ...). If one of these quantities is not fixed, different RBE definitions can be obtained [4].

On this basis, few nuclides can be found that provide both diagnostic and therapeutic radiation and can be used to achieve a more personalized treatment for the patient. This represents the *theranostic* approach and is realized using a single radionuclide with different decay modes or a couple of radioiso-

Nuclide	$T_{1/2}$	Decay mode and branching	E_α (MeV)	$<E_\beta>$ (MeV)	E_γ (MeV)	I_γ
^{149}Tb	4.12 h	α (16.7%), β^+ (83.3%)	3.967	0.730	165.0	26.4
					352.2	29.4
					388.6	18.4
					652.1	16.2
^{152}Tb	17.5 h	β^+ (100%)	–	1.140	271.1	9.5
					344.3	63.5
					586.3	9.2
					778.9	5.5
^{155}Tb	5.32 d	EC (100%)	–	–	86.6	32
					105.3	25.1
					180.1	7.5
					262.3	5.3
^{161}Tb	6.91 d	β^- (100%)	–	0.154	25.6	23.2
					48.9	17.0
					74.6	10.2

Table 1.2: Decay characteristics of the four terbium radionuclides [6, 8, 9]. (EC=electron capture)

topes of the same chemical element (or of different elements but with similar chemical properties). In this way, the labelled-radiopharmaceuticals have the same biological distribution and their concentration is localized in the same regions inside the human body. Different elements are currently investigated and few matched pairs of radionuclides are found for this purpose, like ^{64}Cu–^{67}Cu, ^{44g}Sc–^{47}Sc and ^{124}I–^{131}I to name a few, for a combination of PET and internal radiotherapy (Tab. 1.1). However also single radionuclides are used, as the case of ^{177g}Lu which is a β^- emitter and has γ–rays suitable for SPECT imaging [5].

In this work the attention is focused on terbium due to its very interesting properties for theranostics applications in nuclear medicine [6, 7, 8]. In the following, the potentialities of some terbium isotopes are presented with particular consideration on ^{155}Tb, illustrating its innovative production routes.

1.1 The Swiss Army knife for nuclear medicine

Recently, many groups have carried out studies on innovative theranostic radionuclides and have identified terbium as a very promising and versatile element for medical applications thanks to its four interesting radioisotopes: ^{149}Tb, ^{152}Tb, ^{155}Tb, ^{161}Tb. Their physical properties, reported in Tab. 1.2,

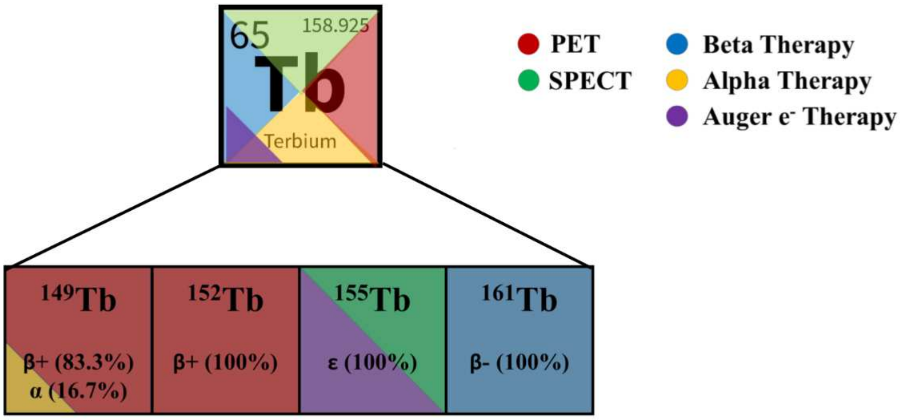

Figure 1.1: Principal clinical applications of terbium radionuclides.

make them suitable for PET, SPECT, Auger electrons and $\alpha-$ and $\beta-$particle therapy [8, 9, 10] (as represented in the Fig. 1.1). For this reason terbium is referred to as the *"Swiss Army knife"* for nuclear medicine [7].

A first *in-vivo* study has been performed by Müller et al. [8] confirming the potential use of these radionuclides in Nuclear Medicine, alone or combined in matched pairs for theranostic applications. In particular, Ref. [8] has represented the first report on the pre-clinical application of the four terbium radioisotopes using the same targeting agent, suggesting further studies on these radionuclides and on new tumor-targeting molecules.

The radionuclide ^{149}Tb emits short range α particles [11] which are characterized by a high LET that allows to induce critical DNA damage in cancer cells. Among radiolanthanides ^{149}Tb is the only one suitable for α therapy thanks to its half-life of 4.14 h, as already proved in literature [8, 12]. Moreover it is also a positron emitter and its potential application for PET imaging has been recently demonstrated [12], therefore allowing the use of a single radionuclide for imaging and α therapy.

The radionuclide ^{152}Tb is suitable for PET imaging, since it emits positrons of an average energy of 1.080 MeV. This nuclide has already been used for preclinical studies [13] and also for the first human multimodal PET/CT scan [14]. The latter study compares ^{152}Tb with a common PET nuclide, ^{68}Ga ($T_{1/2}$=68 min). Terbium provides a lower image quality with respect to Ga, but can be really useful for pre-therapeutic dosimetry thanks to its longer half-life.

The radionuclide ^{155}Tb decays by electron capture and emits γ rays suitable for SPECT imaging without high radiation dose to the patient and can be used for pre-therapeutic imaging and dosimetry like ^{152}Tb. Moreover this nuclide emits also Auger electrons [15, 9] (4.84 keV and 34.9 keV) and therefore can be used for targeted therapy.

The radionuclide ^{161}Tb decays emitting β^- particles and has physical properties very similar to ^{177}Lu (which is a β^- emitter commonly used in clinics with $T_{1/2}$=6.6443 d). However its peculiar feature is also the emission of conversion or Auger electrons which makes this nuclide therapeutically more effective than ^{177}Lu. Moreover it emits also γ rays suitable for SPECT and therefore can be used for dosimetry imaging [16].

All the studies performed until now demonstrate the successful use of Tb radionuclides and open the way for their clinical applications. Nevertheless, to overcome the current theoretical model uncertainties and experimental data scarsity, further investigations of innovative nuclear reaction routes for high yield, radionuclidic purity and specific activity are required.

1.2 Why ^{155}Tb? SPECT and Auger therapy

This thesis is focused on the study of different generator-based nuclear reactions to accurately describe the cross section and to identify the optimal conditions for the production of ^{155}Tb, useful for SPECT imaging and Auger therapy. Therefore, before the detailed description of this work presented in the following chapters, a brief overview of the SPECT imaging technique and of therapy with Auger electrons is given here to draw the attention to the importance of this theranostic nuclide. For completeness, the characteristics, the advantages and limitations of Single Photon Emission Computed Tomography (SPECT) imaging are reported in Tab. 1.3 and are compared to the ones of other very common diagnostic techniques: Computed Tomography (CT), Magnetic Resonance (MR) and Positron Emission Tomography (PET). With reference to Tab. 1.3 and to Ref. [17], SPECT and PET are based on the use of radiopharmaceuticals and are used in various applications, especially to study biological and metabolic processes in oncology, cardiology and neurology, to name a few. On the other hand, CT and MR are predominantly used for anatomical/morphological imaging and among these two techniques MR offers a higher soft tissue contrast. Both techniques have a greater spatial resolution ($\leq 100\mu$m) with respect to PET and SPECT, and are based on a different mechanism. Indeed CT is based on the use of an external X-ray source, while MR does not exploit ionizing radiation. Moreover, recent improvements on MR show its potential use also on functional studies of the brain.

1.2.1 SPECT: definition, functioning and innovations

SPECT is an imaging technique based on the use of a radiopharmaceutical containing a γ-emitter. This exam provides functional and metabolic information of a region of the human body, revealing for instance inflammations or, in more serious cases, also the presence of tumors. The emitted gammas can be revealed with the use of a *gamma camera* as shown in Fig. 1.2, that rotating 180° allows to obtain three-dimensional image of the scanned organs (or also projection on specific planes). The gamma camera is made up of a number

Modality	CT	MR	PET	SPECT
Contrast mechanism	X-ray attenuation of tissues	Emitted RF signal after nuclear spin excitations	photon emission after positron annihilation	emitted γ-ray photons
Penetration	>500 mm	>500 mm	>500 mm	>500 mm
Intrinsic contrast	high (bones) low (soft tissues)	high	None (Requires positron-emitting radioisotope labeled imaging agent)	None (Requires gamma-emitting radioisotope-labeled imaging agent)
Spatial resolution	<=100 μm	<=100 μm	1–2 mm	0.5–2 mm
Typical acquisition time	10—25 min	5-–60 min	10—90 min	30–90 min
Advantages	excellent bone imaging	non-ionizing radiation; very good soft tissue contrast; biochemical information (spectroscopy)	high sensitivity; fully quantitative data; high range of applications (imaging agent dependent); dynamic measurements	high range of applications (imaging agent dependent); simultaneous radioisotope imaging possible
Limitations	radiation dose; low soft tissue contrast	expensive equipment; high maintenance costs; lack of bone contrast	use of radioactive agents; highly specialized equipment and staff required; high costs	use of radioactive agents; semi-quantitative data; costs
Main application	anatomical (bone); imaging	anatomical (soft tissue); imaging in vivo MR spectroscopy	diagnostic imaging (oncology, neurology, cardiology); pharmacokinetic and pharmacodynamic imaging	diagnostic imaging (oncology, neurology, cardiology); drug development

Table 1.3: Comparison of the characteristics, advantages and limitations of Computed Tomography (CT), Magnetic Resonance (MR), Positron Emission Tomography (PET) and Single Photon Emission Computed Tomography) [17].

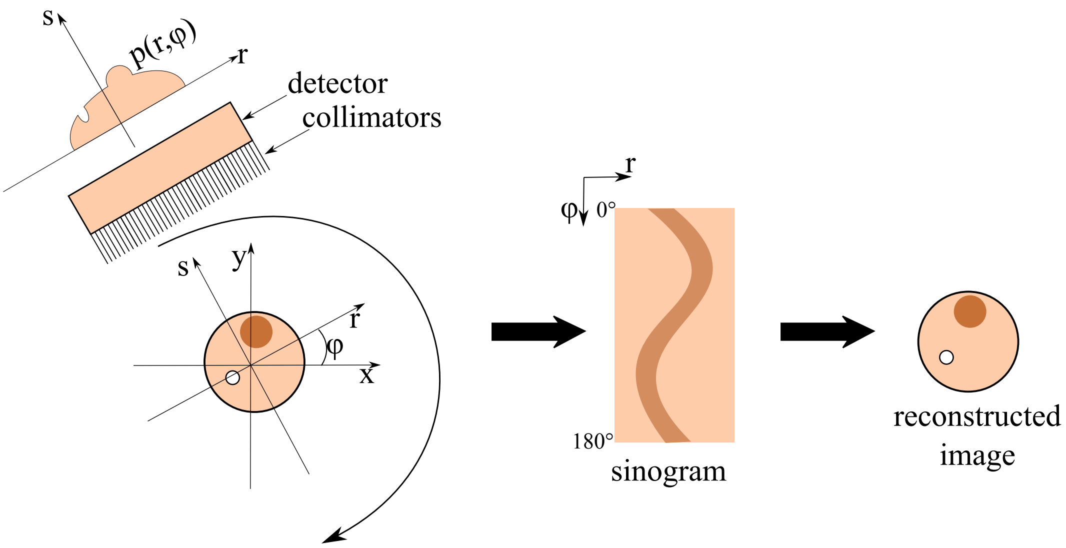

Figure 1.2: Schematic representation of SPECT imaging technique. At each position, the gamma camera, composed by the collimators and the detector, allows to collect the projection of the scanned object $p(r, \varphi)$. The gamma camera, rotating of 180°, provides a set of projection profiles (the sinogram). From the sinogram, using reconstruction algorithms, the image of the scanned object is obtained. [18].

of components, like collimators, detector and electronics to build a signal and send it to a computer that convert it to an image.

The collimators are structures interposed between the patient and the detector. Their main function is an accurate spatial localization of the γ source and of the tumour, and they have to be as close as possible to the patients in order to maximize the spatial resolution. The collimators are made of materials with high atomic number and high density and they are characterized by thousands of holes separated by septa. The gamma is emitted isotropically by the radionuclide administered to the patient. Only the γ rays emitted in a specific direction pass through the holes and contribute to the final image, while all the others are absorbed by the septa whose thickness depends on the used radionuclide: more energetic the nuclide is, the thicker the septa have to be. Therefore, the collimators absorb lots of the radiation emitted by the patient and this results in images with less morphological details. The use of the collimators represents the main issue of SPECT and also its difference in comparison to PET, that on the contrary offers higher quality images. Once the γ-rays pass through the collimator, they arrive to the detector where they lose energy by Compton and/or photoelectric effects. The detector usually is a scintillator crystal (sodium iodide doped with thallium, for example) and it is coupled with a photo-multiplier tube that converts the photons into electrons and, through a cascade, generates an electric signal.

Commonly, in hospitals SPECT scanners are composed of two or three head cameras which allow to reduce the acquisition time, and in which the

Nuclide	$T_{1/2}$	Decay mode	E_γ (keV)	I_γ
^{99m}Tc	6.02 h	IT (100%)	141	89%
^{123}I	13.22 h	EC (100%)	159	83%
^{111}In	2.80 d	EC (100%)	171	91%
			245	94%

Table 1.4: Physical properties of the γ-emitters commonly used in clinics [20]. (EC=electron capture, IT=internal transition)

collimators can have different geometries: also the holes of the collimator can have different sizes depending on the particular organ to scan and on the used radionuclide. At each position of the gamma cameras, 2D projections of a slice of the part of the human body under exam are acquired forming a sinogram. With reference to Fig. 1.2, the projections are collected in the (r, φ) system which is rotated with respect to the system of the object but is fixed with respect to the gamma camera. From the sinogram, by using methods for image reconstruction, like the filtered back-projection [18, 19], the image of the scanned part is finally obtained.

An important aspect of the SPECT technique relies on the fact that the γ-rays can pass through several organs with different specific densities. Therefore a correction for the attenuation of the γ-rays is necessary and can be obtained by adding a CT to the SPECT imaging. SPECT/CT represents a multimodal imaging technique that allows to better localize the source of the γ-rays emission. The attenuation of the γ-rays is described by the following relation:

$$I(t) = I_0\, e^{\sum_i -\mu_i x_i},$$

where I_0 is the initial intensity, μ_i is the effective attenuation coefficient of a tissue and x_i is the distance travelled by the γ-ray in the tissue. From the measured intensity I, an array of attenuation coefficients is obtained for each slice of the scanned organ and is used to correct the emission counts obtained from SPECT, resulting in a attenuation-corrected SPECT image. With a similar approach, as a secondary effect, an image with more detailed information is obtained that contains both functional and structural features, for a better understanding of the clinical picture.

With respect to PET, SPECT still represents the predominant technology due to the lower costs of SPECT cameras and the higher availability of γ emitters. Moreover, this technique is constantly improving thanks to emerging developments that are due to the use of new radionuclides and to technological innovations, since new instrumentation (like new scintillating materials and semiconductor detectors) is needed to detect γ-rays with energies different from the ones of the most common SPECT radionuclides.

At the moment, three are the radionuclides that are commonly used in clinics for SPECT imaging: ^{99m}Tc, ^{123}I and ^{111}In. Their main physical properties are reported in Tab. 1.4. The radionuclide ^{123}I is used in clinics for thyroid

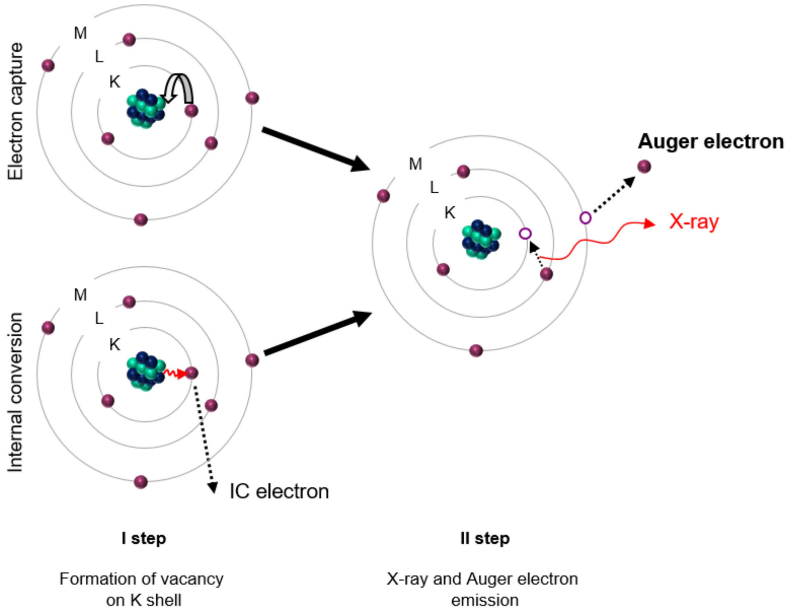

Figure 1.3: The emission of Auger electrons is a secondary effect after a vacancy in the inner shell is created due to electron capture or to internal conversion processes [24].

examinations especially when combined with the β^- emitter ^{131}I, that was the first radionuclide used in clinics for thyroid malignant diseases [21, 22]. However, approximately 85% of all nuclear imaging examinations are based on the use of ^{99m}Tc [23]. This relies on its large availability since it can be easily produced with the generator system ^{99}Mo/^{99m}Tc, but especially on the different developed molecules that deliver the radionuclide to specific regions of the human body as described in Ref. [23]. Besides these two radionuclides, ^{111}In has revealed to be interesting to study infectious diseases due to its longer half-life that allows to study long biological processes. ^{111}In is also frequently used for dosimetry studies even if its combination with the very used therapy radiolanthanide ^{177}Lu is not optimal due to their chemical diversity. Indeed their combined use may result in different bio-distributions and may introduce errors in the reconstruction of the image of the treated organ.

A similar problem can be solved using the lanthanide ^{155}Tb which is suitable for investigations of biological activities over several days thanks to its longer half-life. This radionuclide allows the use of the same detectors of the three common SPECT nuclides, since the energy of their γ rays is similar (as shown in Tab.1.2 and Tab.1.4). Moreover it can be coupled with ^{177}Lu or better with its other isotope, ^{161}Tb, for a very precise diagnostic imaging.

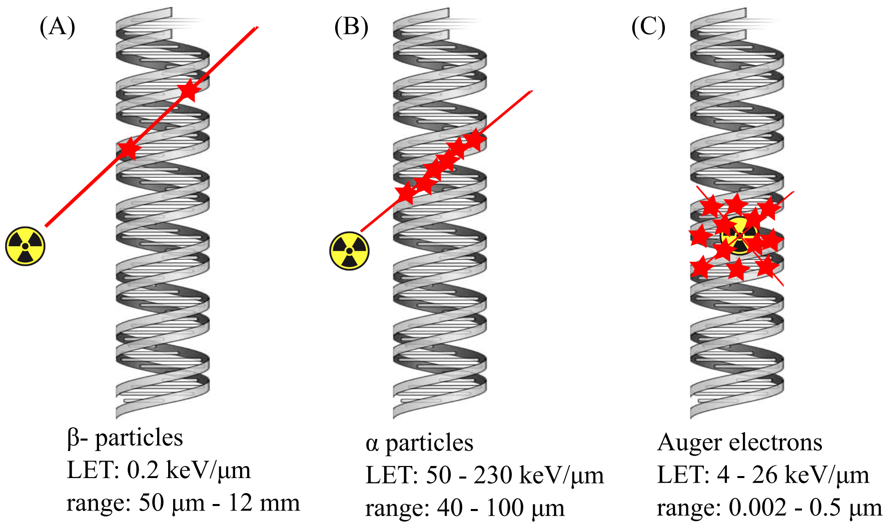

Figure 1.4: Comparison of range and LET of β^- particles (A), α particles (B) and Auger electrons (C) as shown in Ref. [26]. Since the range is small, the radionuclide emitting Auger electrons should be placed very near or better inside the cell nucleus to damage DNA.

1.2.2 Auger therapy

Many radionuclides used for SPECT imaging (such as ^{123}I, ^{99m}Tc, ^{121}In, and also ^{155}Tb in future) emit also Auger electrons as a result of their decay through electron capture and/or internal conversion. Indeed these processes create a vacancy in an inner electron orbital which can be filled by the decay of an electron of a higher shell, characterized by a lower binding energy as shown in Fig. 1.3. In the transition of this electron, energy is emitted as X-ray or is transferred to another electron which is ejected. The ejected electron is referred to as Auger electron and has lower energy (< 25 keV), which is deposited over very short distances (nanometer scale, like the size of a cell nucleus). The short range of Auger electrons yields high linear energy transfer (between 1 and 23 keV/μm [25]) and thus they are extremely useful in cancer treatment especially when are emitted in proximity of cancer cell membrane or cell DNA. In Fig. 1.4 the comparison of the effect of α and β^- particles and Auger electrons to DNA is shown with the values of the corresponding LET and range.

As reported in Ref. [25], different *in-vitro* studies have been performed that have shown that Auger electrons can kill cancer cells by inducing lethal damage to DNA. Also preclinical *in-vivo* studies of mice have revealed the feasibility of the use of Auger electrons, showing the inhibition of the tumor growth and minimal toxicity of normal tissues. Besides these, only few clinical studies have been performed with promising results achieving tumor remission or improving the survival in patients.

The main issue is still represented by the delivery of a compound containing an Auger electron emitter to the target cell nucleus. In general this represents

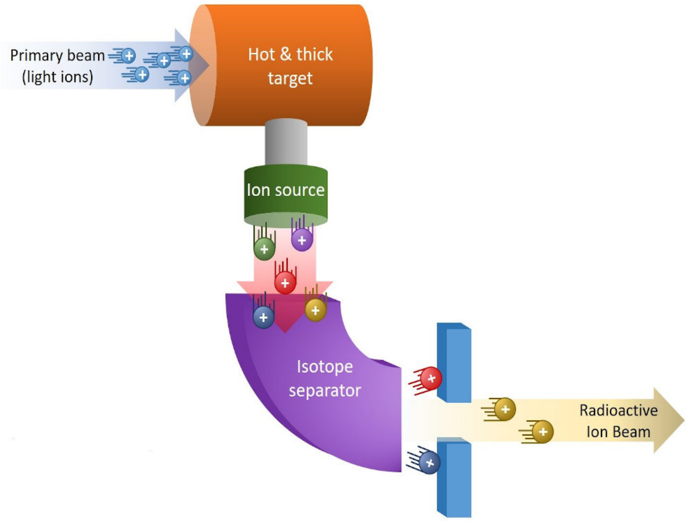

Figure 1.5: Schematic representation of the ISOL technique as used in the ISOLPHARM porject of LNL-INFN [28].

an open problem in Nuclear Medicine, both for imaging and therapy, and different investigations are done considering also the possible use of nanoparticles. They can allow the realization of very interesting structures that can help to achieve different concepts:

- theranostics, using diagnostic and therapeutic radionuclides (also chemically different);
- multimodal imaging, considering elements with specific physical properties that can be used to perform different imaging techniques, for instance SPECT/CT/MRI/FI (Fluorence imaging) [27].

Therefore, further investigations have to be performed to improve the technology of the imaging techniques, to find new strategies for the targeted drug delivery and also to select and produce innovative medical radiopharmaceuticals. Regarding the last aspect, there are different research groups operating worldwide to investigate theranostic radionuclides and in particluar I am involved in the Italian project REMIX (Research on Emerging Medical radioIsotopes from the X-sections) financed by the INFN (National Institute of Nuclear Physics).

1.3 The INFN REMIX project

REMIX is a part of the SPES[1]/LARAMED project that has the goal to identify possible production routes for ^{47}Sc, ^{155}Tb and ^{161}Tb by using accelerators.

---

[1] https://www.lnl.infn.it/en/spes-2/

LARAMED (LAboratory of RA-dioisotopes for MEDicine) [29] is a new activity that was established a few years ago at Legnaro National Laboratories of INFN (LNL-INFN) where a 70 MeV cyclotron has been installed. The aim of LARAMED project is to study the applications of Nuclear Physics to Medicine, in particular the development of production methods of new medical radionuclides, such as ^{99m}Tc, ^{67}Cu, ^{47}Sc, ^{52g}Mn, ^{155}Tb and ^{161}Tb to name a few.

In general, there are two techniques to produce medical radionuclides:

- **ISOL (Isotope Separation On Line) technique**, which consists in the use of accelerated particle beams on a specific target held at high temperature. In this way, thanks to diffusion and effusion processes, the produced radioactive species are released from the target surface and are transferred to an ion source, where atoms are ionized, extracted, reaccelerated and selected by a mass separator. The separation provides a single-mass nuclide beam collected onto a dedicated target that will be dissolved to finally obtain only the desired radionuclide. A schematic representation of this technique is shown in Fig. 1.5, used in the ISOLPHARM porject of LNL-INFN [28].

- **direct activation technique**, which is the traditional method to produce medical radionuclides and differs from ISOL since it does not use a mass separator. After the selection of a particular nuclear reaction, an accelerated particle beam is impinged on the specific selected target producing the nuclide of interest. The nuclide is identified and quantified by high precision gamma spectroscopy with HPGe (High Purity Germanium) detectors. Also other chemical elements are produced inside the target and chemical dissolution and elution processes are necessary to separate the desired element. In the ideal case of a perfect chemical procedure, the final product is composed of the nuclide of interest as well as of its isotopes (the contaminants), since no mass separation is performed. In a more realistic situation however, in the final product also isotopes different from the required element could be present. Fig. 1.6 shows the different steps of this technique as reported in Ref. [30].

Among International Research Centers, for example CERN exploits the ISOL technique in one of its facilities (MEDICIS) [31], while in the Paul Scherrer Institute (PSI) [32, 33] the direct activation technique is used.

At the LNL-INFN both methods can be used: the REMIX project is based on the second technique which usually offers a final product with higher yield, but lower purity and lower specific activity with respect to the ISOL technique, due to the presence of the contaminants. In this case, an accurate investigation of the nuclear reaction is essential to select the optimal irradiation condition to maximize the production of the nuclide of interest while minimizing the co-production of contaminants.

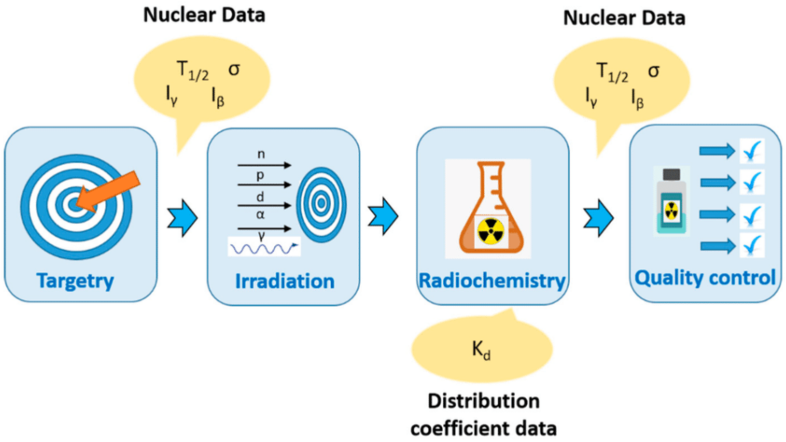

Figure 1.6: Schematic representation of the different steps of the direct activation technique [30].

A project like REMIX is by nature interdisciplinary, since it requires the expertise on different disciplines [30]:

- **material science and engineering** for the selection and design of the target, which must be as chemically pure as possible or also isotopically pure in the case is made of an enriched isotope. The target must be characterized by a high stability, high melting point and also with a specific thickness to optimize the production of the nuclide of interest. Several tests are performed to validate the targets, that for the REMIX project are mainly produced with the High Energy Vibrational Powder Plating (HIVIPP) deposition for metallic powders and with the SPS (Spark Plasma Sintering) technique using of a sintering machine (TT_Sinter [34]) [35] built in the Pavia unit of INFN useful for oxide powders sintering.
- **nuclear physics** to study the irradiation of the target both experimentally and theoretically. Theoretical studies and simulations help to suggest energy windows for new experimental data measurements. Moreover these studies allow also to identify the optimal production conditions for high yield and purity. I contribute with my work to this part, describing specific nuclear reactions with nuclear reaction codes based on theoretical models. In this context, experimental data help to constraint and tune the models to obtain a coherent and global representation of the cross sections of both radioactive and stable nuclides produced in a given reaction. From the experimental point of view, the targets, after their preparation, are irradiated using the stacked-foils target technique that consists in the use of a layered set of thin target foils, among which monitor and degarder foils are interleaved. The monitor foils are used to assess the beam intensity while the degrader foils to reduce and control the incident beam energy upon each target foil. In this way, each thin target foil is activated by an incident beam characterized by a specific

energy. Therefore, in a single irradiation, the whole stack allows to measure cross sections at different energies. The activation of each foil is measured by γ-spectroscopy and, after the data analysis, measurements of the cross section of the produced radionuclide are obtained and can be compared with the theoretical curves.

- **radiochemistry and radiopharmacy** to explore all the possibilities to extract the element of interest and also to recover the target material for recycling it for other productions. This step is particularly important for enriched targets.

- **biomedical physics and medicine** for quality control studies. Accurate activity, radionuclidic purity and specific activity measurements are crucial for dosimetry calculations and evaluations in order to assess the validity of the considered nuclear reaction.

Different units of INFN (Milano, Pavia, Padova, Ferrara and Legnaro) cooperate to fulfill the goals of the project which benefits also of the collaboration with the GIP ARRONAX (Saint-Herblain, France), the Sacro Cuore Don Calabria Hospital (SCDCH, Negrar, VR, Italy) and the Istituto Oncologico Veneto (IOV, Padova).

In this framework, my contribution concerns the investigation and simulation of nuclear reactions for the production of ^{155}Tb. In particular I have explored three generator-based reactions using natural targets (natural terbium is monoisotopic and is made 100% of ^{159}Tb):

$$p + {}^{159}\mathrm{Tb} \rightarrow {}^{155}\mathrm{Dy} + 5n \rightarrow {}^{155}\mathrm{Tb}, \tag{1.1}$$
$$d + {}^{159}\mathrm{Tb} \rightarrow {}^{155}\mathrm{Dy} + 6n \rightarrow {}^{155}\mathrm{Tb}, \tag{1.2}$$
$$\alpha + {}^{nat}\mathrm{Gd} \rightarrow {}^{155}\mathrm{Dy} + xx \rightarrow {}^{155}\mathrm{Tb}. \tag{1.3}$$

They consist in a two step reaction chain: the production of ^{155}Dy (the generator with $T_{1/2} \simeq 9.9$ h) which decays 100% by electron capture in ^{155}Tb. Generators have been the first method used for the production of medical radionuclides, even before the construction of cyclotrons. Thereafter generators have been widely developed and still contribute to the production of some of the mostly used radionuclides, as the ^{99m}Tc from ^{99}Mo/^{99m}Tc generator, since they can provide a continuous source of the radionuclide of interest far away from the production site. Indeed, the parent nuclide (^{99}Mo) is usually placed in an apparatus that allows the separation and extraction of the daughter (^{99m}Tc), even many times a day. In particular from the physical point of view, as for all generators systems, the timings for the chemical separation processes must be accurately analysed to optimize the production.

1.4 Review of experimental data

In the investigation of a nuclear reaction, a first step is represented by the analysis of the experimental data if they are available. Indeed, as described in the previous section, they can help the theoretical groups to refine the models for a better description of the excitation functions and for accurate calculations of important quantities related to the production of a radionuclide. Therefore, considering the energy of the LNL-INFN cyclotron (70 MeV), some nuclear databases like EXFOR and Data Explorer, both of the IAEA (International Atomic Energy Agency) [36, 37], have been consulted in the energy range 1–100 MeV to extract the available data for the three generator reactions. In the REMIX project, new measurements are planned for the reaction with protons by the experimental group of Milano, thus these new data are not available yet and can not be used to support the calculations and the theoretical modeling presented in this thesis.

All the available experimental data are shown in the next pages in a compact way. In the third chapter these plots will be considered one by one in comparison to the theoretical curve obtained with the modeling approach that will be presented in the next chapter.

Reaction with protons

For the reaction with protons, in 1971 Lebowitz et al. [38] performed the first measurements of cross sections for the production of ^{157}Dy, while in 2007 Hassan et al. [39] measured the cross sections of ^{159}Dy. Their works have been followed by the studies of:

- Steyn et al. in 2013 [40] for ^{153}Dy, ^{155}Dy, ^{157}Dy, ^{159}Dy, ^{153}Tb, ^{155}Tb, ^{156}Tb and ^{151}Gd, ^{153}Gd;

- Engle et al. in 2016 [41] for ^{153}Dy, ^{155}Dy, ^{157}Dy, ^{159}Dy, ^{151}Tb, ^{152}Tb, ^{153}Tb, ^{154}Tb, ^{155}Tb, ^{156}Tb, ^{158}Tb and ^{147}Gd, ^{149}Gd, ^{151}Gd, ^{153}Gd;

- Tarkanyi et al. in 2017 [42] for ^{153}Dy, ^{155}Dy, ^{157}Dy, ^{159}Dy, ^{152}Tb, ^{153}Tb, ^{154}Tb, ^{155}Tb, ^{156}Tb, ^{158}Tb, ^{151}Gd, ^{153}Gd and for some metastable state of terbium, ^{154m2}Tb, ^{156m1}Tb, ^{156m2}Tb.

All these data are shown in Fig. 1.7-1.8. Only the data of Hassan et al. show a slightly different behaviour with respect to the other datasets, which in general are in good agreement with each other. An accurate theoretical modeling is necessary to reproduce the tail and the peaks of the cross sections, which are dominated by two different processes that will be discussed in the next chapter: the *pre-equilibrium* process is predominant in the description of the tails while the *compound nucleus* mechanism for the peaks.

Reaction with deuterons

Concerning the reaction with deuterons, less experimental data are available: recent measurements have been performed mostly by Tarkanyi et al. in 2013 [43] for ^{155}Dy, ^{157}Dy, ^{159}Dy, ^{155}Tb, ^{156}Tb, ^{160}Tb and ^{153}Gd. Some channels have been studied in the past by Duc et al. (1968) [44] for ^{157}Dy, ^{159}Dy and ^{160}Tb and Siri et al. (1970) [45] for ^{157}Dy and ^{160}Tb. Very recently, in 2019 also Ichinkhorloo et al. [46] performed some measurements, for ^{157}Dy, ^{159}Dy and ^{160}Tb.

As shown in Fig. 1.9, only for ^{157}Dy the data seem in good agreement, while an evident discrepancy among the datasets is visible for ^{159}Dy and ^{160}Tb. In particular the data of Duc et al. are lower with respect to the others. The disagreement and the shortage of data suggest the need of new experimental measurements in order to better refine the theoretical models and accurately estimate the quantities of interest. In order to describe theoretically these reactions, another mechanism has to be taken into account: the *break-up* process that will be described in the next chapter and will be considered in the modeling study.

Reaction with α particles

For the reaction with α particles, in 1973 Thakur [47] performed measurements only for ^{157}Dy. Other data have been found in literature in the studies of:

- Gayoso et al. (1996) [48] for ^{153}Tb, ^{155}Tb, ^{156}Tb, ^{158}Tb, ^{160}Tb, ^{161}Tb;
- Ichinkhorloo et al.(2021) [49] for ^{155}Dy, ^{157}Dy, ^{159}Dy, ^{153}Tb, ^{155}Tb, ^{156}Tb, ^{160}Tb, ^{161}Tb;
- Moiseeva et al. (2022) [50] with data for ^{155}Dy, ^{157}Dy, ^{153}Tb, ^{154}Tb, ^{155}Tb, ^{156}Tb, the metastable states of terbium ^{154m1}Tb, ^{154m2}Tb and ^{159}Gd.

As for the reaction with protons, also in this case the available experimental data (shown in Figs. 1.10-1.11) are in general in good agreement with each other and the only exceptions are represented by ^{161}Tb and ^{160}Tb. Besides the cited nuclear reaction processes, attention has to be focused also on an accurate selection of the models and on the different physical features of the nuclei, like their deformation.

A study of the generator system ^{155}Dy/^{155}Tb was performed by Steyn et al. and by Moiseeva et al. for the reactions with protons and α particles respectively. Using a fit of their data, they showed a first calculation of activities and purities. Their study opens the way for the exploration of new possible scenarios for the production of ^{155}Tb and represents the starting point of my thesis. To our knowledge, for the reaction with deuterons, no study of the generator system is present in literature, therefore this thesis shows for the first time the analysis performed starting from the available data and the calculations for the indirect production of ^{155}Tb.

In the next chapter a description of the theory of nuclear reaction is presented to understand the method and approach used for the description of the cross sections of several radionuclides produced in the three considered reactions. Subsequently, the obtained results are shown as well as also the calculations for the optimal irradiation conditions for the production of ^{155}Tb.

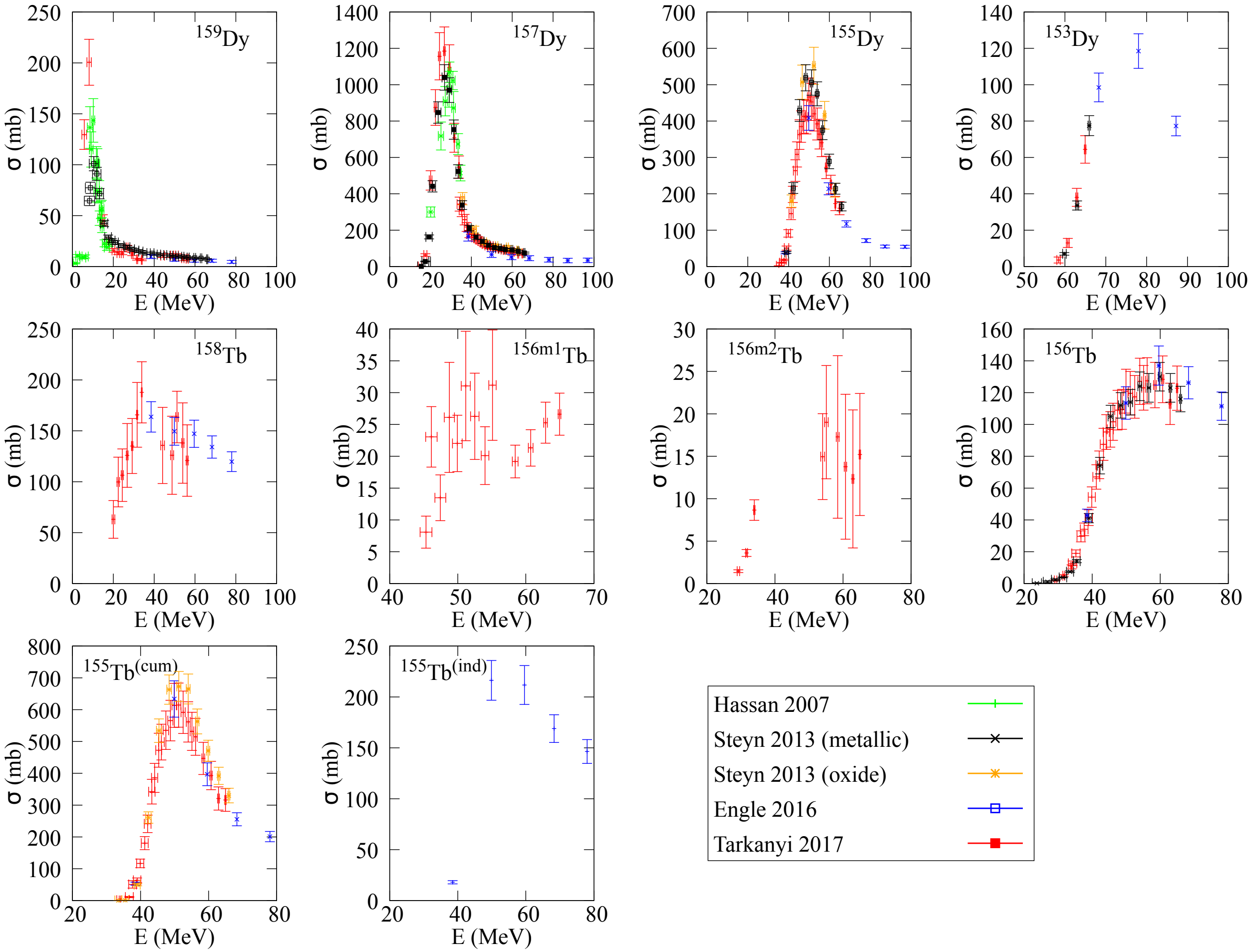

Figure 1.7: Available experimental data for the reaction: $p +^{159} Tb$ (part 1).

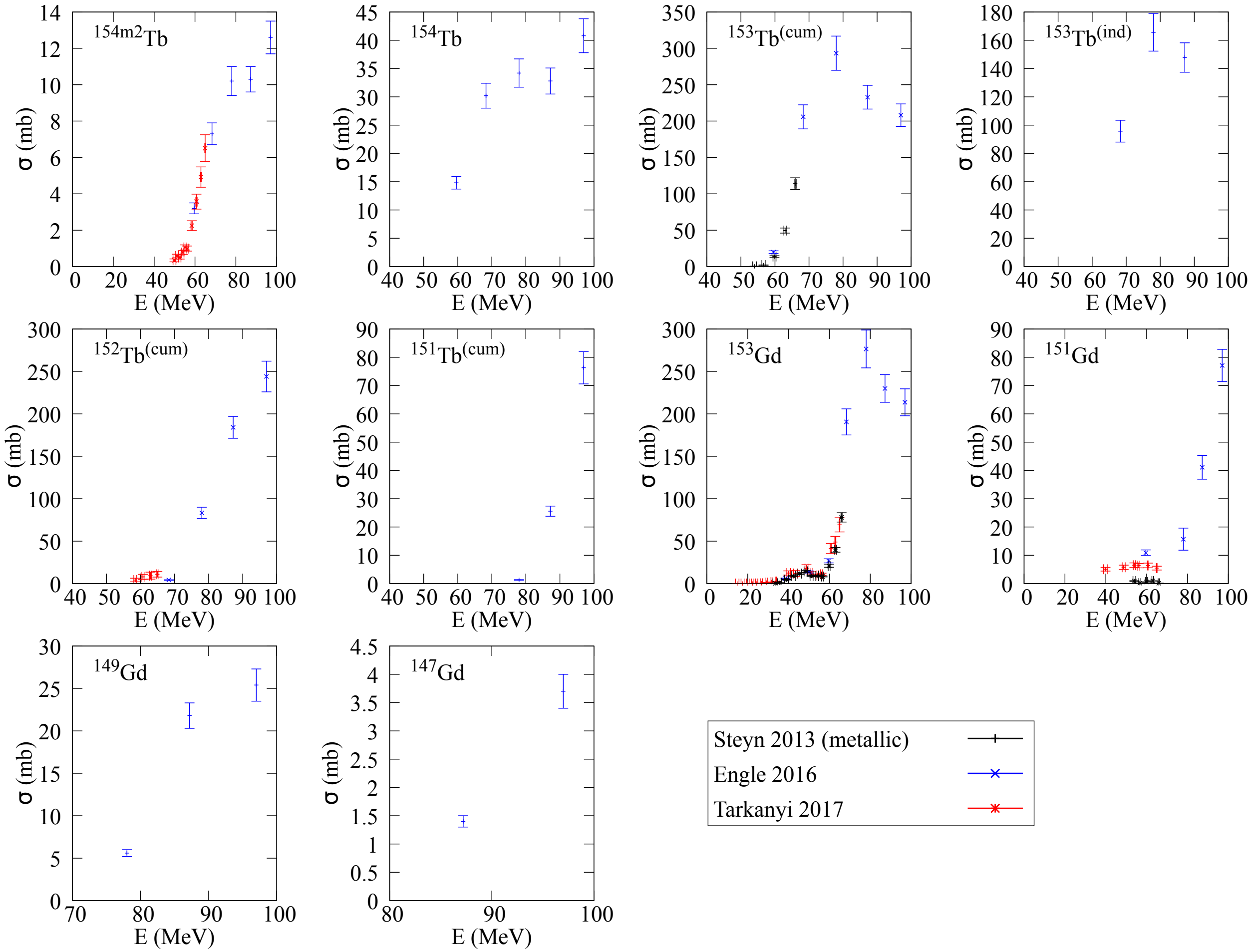

Figure 1.8: Available experimental data for the reaction: $p +^{159} Tb$ (part 2).

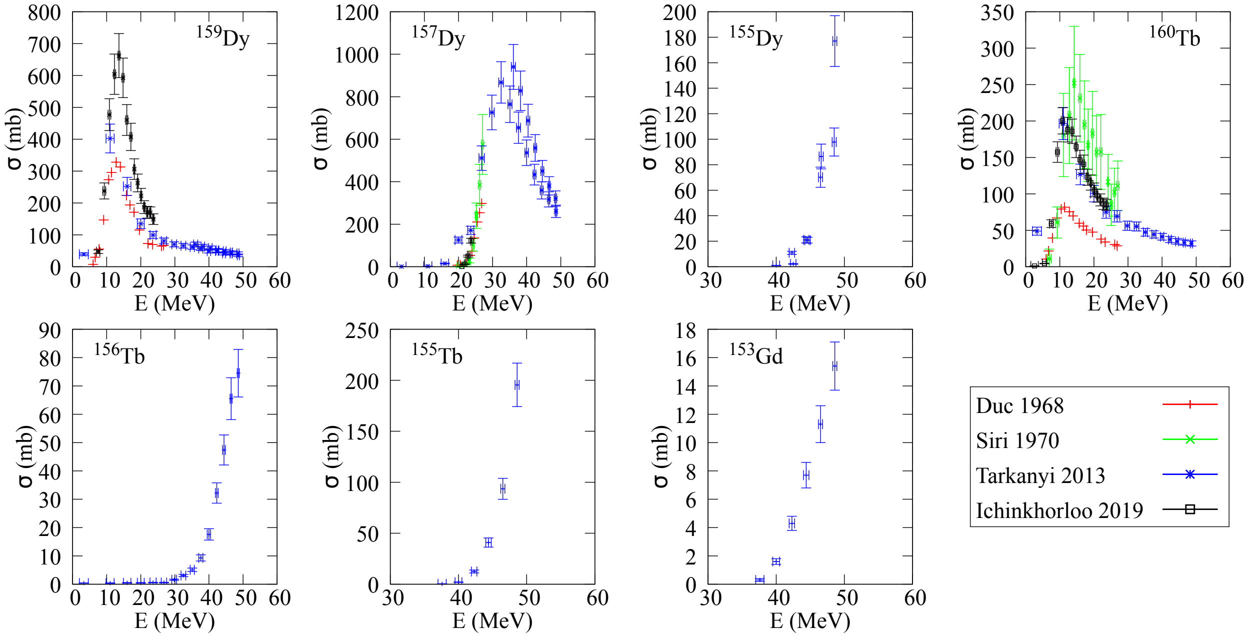

Figure 1.9: Available experimental data for the reaction: $d +^{159} Tb$.

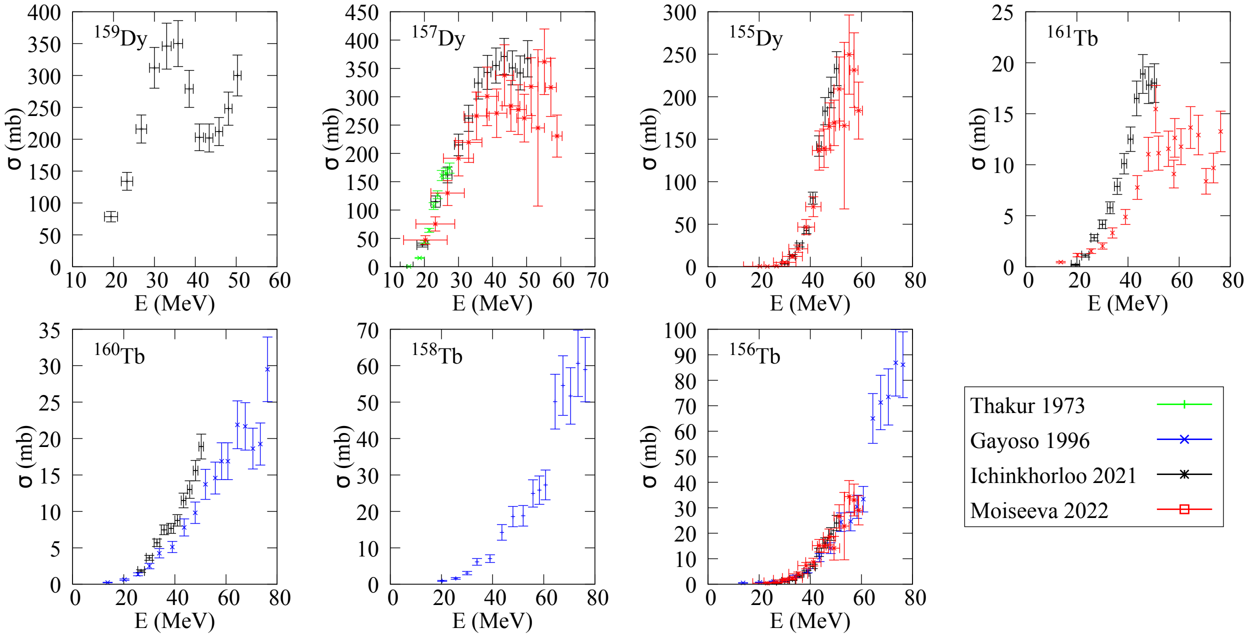

Figure 1.10: Available experimental data for the reaction: $\alpha +^{nat} Gd$ (part 1).

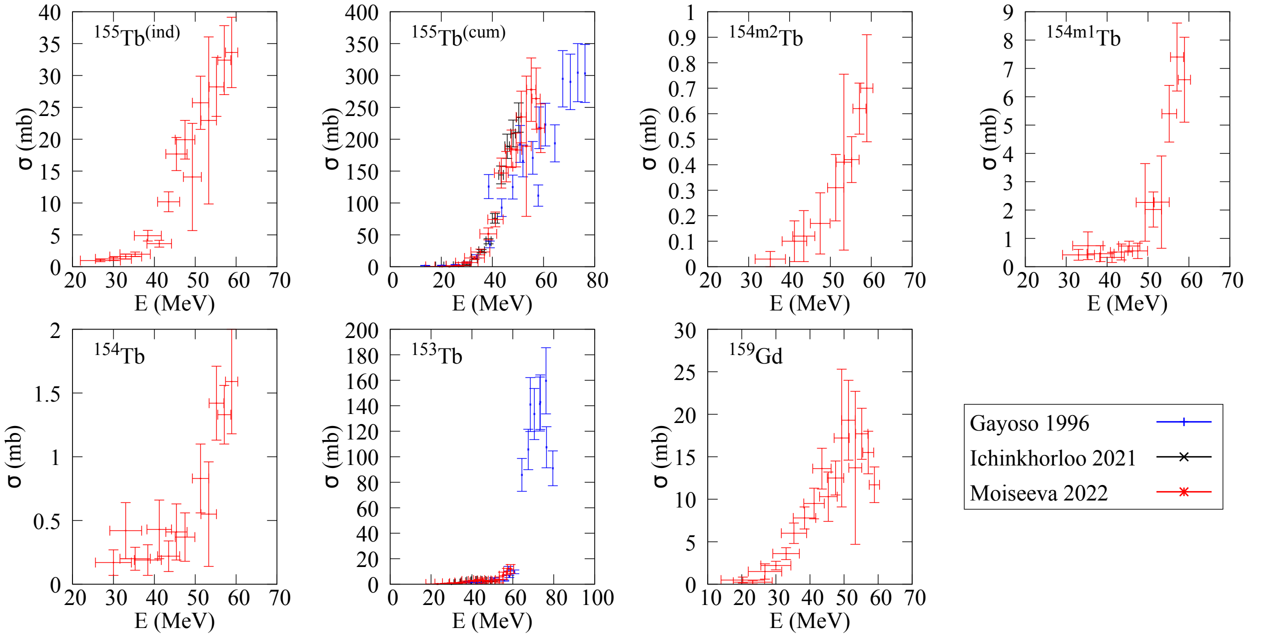

Figure 1.11: Available experimental data for the reaction: $\alpha +^{nat} Gd$ (part 2).

Chapter 2

Nuclear reaction modeling for Tb production

In this chapter a brief overview of the theory of nuclear reactions is presented with a description of the different processes involved, like the optical potential and the compound, pre-equilibrium and direct mechanisms. In particular reference is made to two nuclear reaction codes: the analytical TALYS and the Monte Carlo PHITS, that provide complementary approaches in the study of the production of radionuclides. Finally, the definitions of the quantities of interest in the field of medical radionuclides are introduced, namely yield, radionuclidic purity and isotopic purity.

2.1 Theory: optical potential, direct reactions, compound nucleus and pre-equilibrium processes

It is well known that an incident particle impinging on a target nucleus can produce a variety of final states, depending on the beam and the target characteristics. Different mechanisms describe the various phenomena and scenarios that can take place on the interaction between the projectile and the target. In particular at low energies the most probable event is the *scattering* and two possibilities can be observed: the *elastic scattering* when the internal states of the colliding particles are unchanged; the *inelastic scattering* when the target nucleus is in an excited state and the emitted particle is released with less energy compared to the elastic case. At higher energies, a nuclear reaction occurs forming a final state different from the entrance channel. A classification of the nuclear reaction mechanisms can be given in terms of both the time scales and the number of collisions with the target nucleons (intranuclear collisions). In general, short reaction times and few collisions are related to direct reactions, while the opposite case (long times and many collisions) to the compound nucleus reactions. Moreover, an intermediate state can be observed, namely the

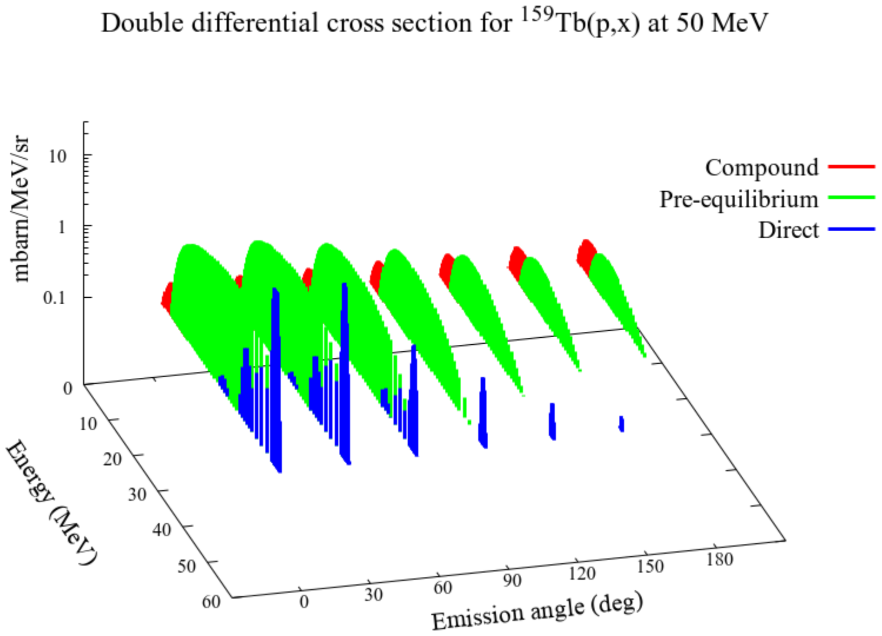

Figure 2.1: Double differential cross section simulated with the TALYS code (described later) for incident 50 MeV protons on ^{159}Tb. The colors indicate the different contributions (compound, pre-equilibrium and direct) to the total reaction cross section. In this case, the major contribution is given by the pre-equilibrium process.

pre-equilibrium process. When many collisions occur, a statistical approach is required for an accurate description of the involved processes. These three mechanisms are also characterized by different angular distribution as shown in a typical double differential cross section (Fig. 2.1): isotropic emission at low energy for the compound nucleus reaction; forward-peaked emission at high energies for the direct reaction; slightly anisotropy at intermediate energies for the pre-equilibrium process.

Optical potential

In a more formal and precise way, the mechanisms are described by means of theoretical models and all the theory is based on the initial description of the interaction with a particular potential, namely the *optical potential.* It has been introduced initially to describe the elastic and inelastic scattering and then it has extended to include also nuclear reactions. The potential can describe the Coulomb interaction between two charged particles and therefore the deflection of the projectile due to the Coulomb potential of the target nucleus. Moreover it contains also further additional terms to describe the effects of the interaction due to the nuclear potential, which becomes relevant once the

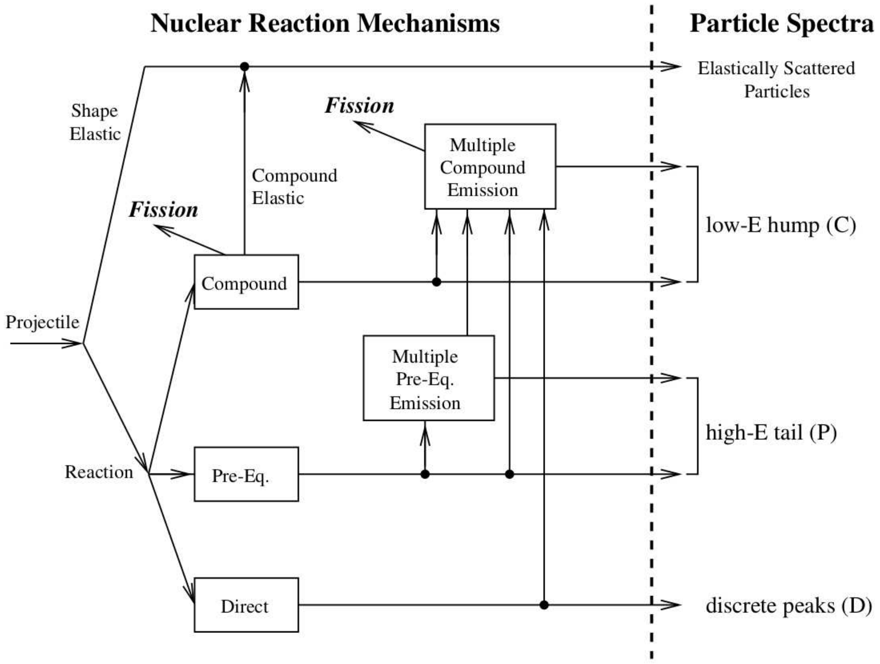

Figure 2.2: General scheme of the reaction mechanisms [51] that describes the initial interaction by means of the optical potential and then the role of direct (D), pre-equilibrium (P) and compound (C) processes in the description of a nuclear reaction and the outgoing particle spectra.

projectile energy is high enough to penetrate the Coulomb barrier. In general the optical potential is a complex mean field potential and is composed of two parts: a real one, that provides information about the elastic contribution of the interaction, and an imaginary part that describes all the non-elastic channels (the reaction channels). It represents the first step in the description of a nuclear reaction as represented in Fig. 2.2. The optical models can be divided in two main groups: phenomenological and microscopic models. In the first case, parametric functional forms have to be postulated and then adjusted to experimental data until a good agreement is obtained. The potential can be written as [52]:

$$U(r) = U_R(r) + U_I(r) + U_D(r) + U_{SO}(r) + U_C(r). \tag{2.1}$$

where:

- U_R represents the elastic scattering;
- U_I is the nuclear term that describes the absorption in the whole volume of the nucleus;
- U_D is another nuclear term that describes the absorption in the surface of the nucleus;

- U_{SO} is the spin-orbit term, necessary for the interaction of the spin of the projectile and the momentum of the target nucleus;
- U_C is the Coulomb potential, essential for charged incident particles.

Each term depends on different parameters (as the radius of the nucleus and the diffuseness of the potential, up to more than 20 overall parameters) and on the availability of experimental data. Due to its high accuracy, the optical model is the most used one.

An alternative is represented by the microscopic approach that can determine the optical model potential without any knowledge of experimental data. Similar models provide a description also for nuclei far away from the valley of stability, but normally with a lower accuracy with respect to the phenomenological models.

The Schrödinger equation expressed with the use of this potential can be solved with the partial-wave expansion analysis [53, 54] that returns quantities useful for the other mechanisms. Indeed, the wave functions are useful for the description of the direct reactions and, from the solution of the equation, the cross sections for the elastic and non-elastic contributions can be obtained. The reaction cross sections can be expressed with dependence on the transmission coefficients T_l that describe the loss of flux in the elastic channel. On one hand these coefficients are the essential components in the formalism for the compound nucleus and, on the other hand, the reaction cross sections are crucial for the description of the pre-equilibrium process.

Therefore, the use of a proper optical potential is extremely important for a global description of a nuclear reaction, since all the other mechanisms rely on this model.

Direct reactions

These reactions are generated by the interaction between the projectile and one or few nucleons of the target. Thus they involve momentum transfer only to nucleons on the surface of the target nucleus: for this reason they are referred to as peripheral reactions.

The theoretical tools commonly used to describe these reactions are the Distorted Wave Born Approximation (DWBA) and the coupled-channels methods [55, 51, 56]. The former is particularly effective for spherical or near-spherical nuclei for which the nuclear radii in the expression of the optical potential are described as $R_i = r_i\,A^{1/3}$ (where A is the mass number and $r_i \simeq 1.25$ fm). But in some cases the nuclei are deformed in their ground state and exhibit rotational bands (excited states) that are strongly coupled to the ground state. These deformations are due to the nucleons collective motion and have been observed in many even-even nuclei. The spectra of the low-lying excited states of these nuclei undergo a transition from the typically vibrational spectrum to a typical rotational one. This aspect can be observed by considering the ratio between the energies of the first 4^+ and 2^+ states, $R_{4/2} = E(4^+)/E(2^+)$

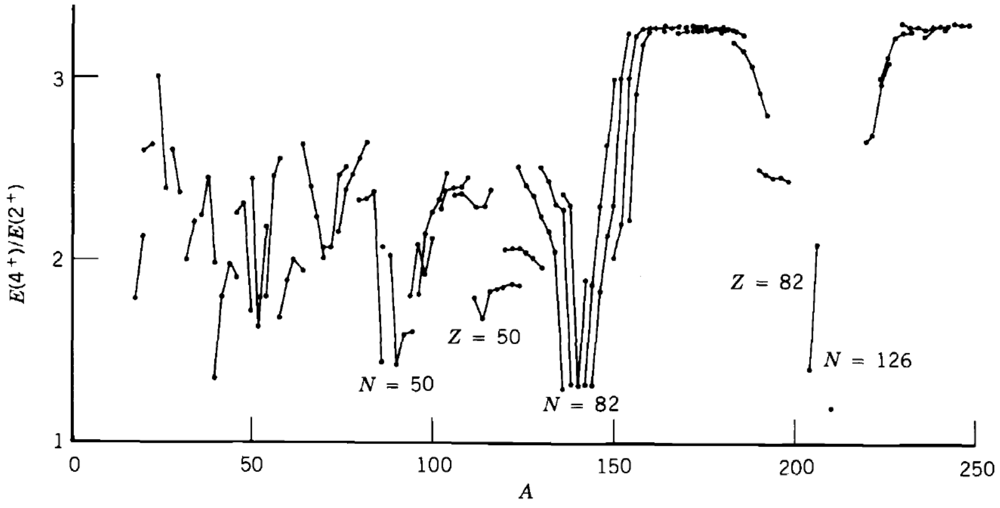

Figure 2.3: Ratio $R_{4/2} = E(4^+)/E(2^+)$ for the lowest 2^+ and 4^+ states of even-even nuclei. The lines connects sequences of isotopes [53].

as shown in Fig. 2.3. The ratio is constant around 3 for $150 < A < 190$ and $A > 230$, while is roughly 2 for $A < 150$. Moreover a larger electric quadrupole moment is observed for $A > 150$, and this suggests that nuclei exhibit a transition from a spherical (or nearly spherical) to a deformed shape [53]. In this context, the more general coupled-channels method has to be used to describe simultaneously both the elastic channel and the other channels that generate these collective phenomena. In particular, the method consists in an approximation of the infinite possible couplings of the internal states of the projectile and the target nucleus. Only few channels are considered: those that are known experimentally or are expected theoretically to be strongly coupled [57]. These coupling have an important impact on the optical potential where an additional potential U_{cc} is present and the elements of the optical potential can be expressed in terms of radii expanded in multipoles as:

$$R_i = r_i\, A^{1/3} \left[1 + \sum_{\lambda=2,4,\ldots} \beta_\lambda Y_\lambda^0(\Omega) \right], \tag{2.2}$$

where the Y functions are the spherical harmonics and β_λ are the deformation parameters that can be predicted from theoretical models, but can be derived also from analysis of experimental angular distribution [51, 56]. In general, β_2 and β_4 are important in the description of the inelastic scattering while higher order deformations are smaller in magnitude. More complex expressions can be written instead of Eq. 2.2 especially in the asymmetric rotational model where, in addition to the deformed ground state, also the vibrational states are included [51].

In the reactions studied in this thesis, some even-even nuclei lay in the mass number range $150 < A < 190$, thus are characterized by a $R_{4/2}$ around

N Z	84	86	88	90	92	94	96
64 (Gd)	1.81	2.02	2.19	3.01	3.24	3.29	3.30
66 (Dy)	1.81	2.05	2.24	2.93	3.21	3.27	3.29

Table 2.1: Experimental values of the ratio $R_{4/2}$ for some even-even nuclei involved in the reaction of this work. The collective properties (rotational for $N \geq 90$) have to be considered in the cross section calculations.

3 and therefore by rotational properties, like dysprosium and gadolinium. In particular Tab. 2.1 shows that the ratio sharply increases for $N \geq 90$ neutrons, indicating that the transition from the spherical to the deformed shape in isotopes of Gd and Dy occurs at $N = 90$. For this reason the study of direct reactions with a coupled-channels formalism is essential to consider carefully the cross section of the nuclides of interest. Different codes have been developed to solve the dynamic equation with this formalism, as discussed later.

Compound nucleus

As cited before, for low energies (few tenths of MeV), the projectile is absorbed in the target, performs many collisions and shares its kinetic energy among all the constituent nucleons of the target, forming a compound nucleus (CN). This nuclear reaction can be described as a 2-step process: the formation of a compound nucleus $a + A \to C^*$ and its decay $C^* \to b + B$, after reaching the statistical equilibrium of the whole system (known as *thermalization* of the compound nucleus). The presence of collisions and the time scale ($\sim\ 10^{-18}\,s$) result in a loss of memory of the compound nucleus C^* about the entrance channel $a + A$, as stated by the *independence hypothesis* (formulated by N. Bohr [58]): the probabilities of the exit channels are therefore independent of the entrance ones and the decay of C^* depends only on its properties. Thus the cross section can be factorized in two terms in following way:

$$\sigma_{CN} = \sigma_{aA} P_{bB} \tag{2.3}$$

where P_{bB} indicates the probability of the transition $C^* \to b + B^*$. This hypothesis was verified and validated experimentally by Ghoshal [59] considering reactions with protons on ^{63}Cu and α particles on ^{60}Ni.

As cited before, the transmission coefficients calculated using the optical potential are extremely important to determine the compound nucleus cross section. This is the main idea behind the Hauser-Feshbach formalism, in which the cross section can be written as [60, 61]:

$$\sigma_{ab} = \frac{\pi}{k_a^2} \sum_{J,\pi} \sum_{\alpha,\beta} \frac{2J+1}{(2s+1)(2I+1)} \frac{T_a^{J,\pi}(\alpha)\, \langle T_b^{J,\pi}(\beta) \rangle}{\sum_{c,\delta} \langle T_c^{J,\pi}(\delta) \rangle} W_{\alpha,\beta}. \tag{2.4}$$

This expression depends on the spin of the projectile (s), of the target (I) and of the compound system (J), on the transmission coefficients for entrance, exit and intermediate channels (a, b and c) and on the so-called width fluctuation correction factor $W_{\alpha,\beta}$, where α and β indicate the spin–angular momenta recombinations of the binary fragments in the entrance and exit channels. The correction factor has been introduced to take into account the deviations in realistic cases from the independent hypothesis. Specifically, at very low energies, interference phenomena between the entrance and exit channels may occur and may be either constructive or destructive. In general, the correction factor results in an enhancement of the elastic channel and a decrease of cross sections in other competing exit channels.

Moreover, also the average of transmission coefficients appears in Eq. 2.4 and has been added to take into account the continuum of many overlapping levels in the residual nucleus. Therefore, the transmission coefficient is averaged over the residual nuclear level density ρ:

$$\langle T_b^{J,\pi}(\beta)\rangle = \int_E^{E+\Delta E} T_b^{J,\pi}(\beta)\, \rho(E,J,\pi)\, dE. \tag{2.5}$$

The nuclear level density is given by the number of excited levels per unit of energy:

$$\rho(E,J,\pi) = \frac{dN(E,J,\pi)}{dE} \tag{2.6}$$

and also in this case different models have been developed from phenomenological to microscopic ones. In the first case, the models are mainly based on the description of the nucleus as a Fermi Gas (and on variations of this approach), where the level density can be written as:

$$\rho(E,J,\pi) = \frac{1}{2}\,\frac{2J+1}{2\sqrt{2\pi}\sigma^3}\,\exp\left[-\frac{(J+\frac{1}{2})^2}{2\sigma^2}\right]\frac{\sqrt{\pi}}{12}\,\frac{\exp\,[2\sqrt{aU}]}{a^{1/4}U^{1/4}}. \tag{2.7}$$

The nuclear level density depends on the parameter $a = \frac{\pi^2}{6}(g_\pi + g_\nu)$ with g_π (g_ν) the spacing of the proton (neutron) single particle states near the Fermi energy. The level density is expressed by the dependence on the *effective* excitation energy $U = E - \Delta$, where Δ is an empirical parameter related to the pairing energy shift due to the odd-even effects in nuclei. By summing over the parity and over the $(2J+1)$ projections of the angular momentum, the state density can be obtained:

$$\rho(E) = \frac{\sqrt{\pi}}{12}\,\frac{\exp\,[2\sqrt{aU}]}{a^{1/4}U^{1/4}} \tag{2.8}$$

through which the parameter a is determined by fitting the available experimental data for each considered nucleus.

On the other hand, the microscopic models are based on the variational Hartree-Fock method, and the level densities are retrieved only numerically. In any case the choice of the level density model plays an important role in the description of the compound nucleus and therefore of the total reaction cross section. Different example of this dependence and extensive discussion will be presented in the results section of the thesis.

Pre-equilibrium process

The pre-equilibrium reaction model embodies features of direct and compound nucleus mechanisms, as shown for example in the angular distribution: the anisotropy indicates the existence of a process preserving part of the memory of the entrance channel, like direct reactions.

According to this mechanism, the incident particle is absorbed into the target nucleus, but shares its energy with only few nucleons and not with the entire system. Thus the particle loses only part of the initial energy and direction. However, the system decays into the final channel much before the statistical equilibrium is reached.

The cross section is calculated using the probability of the particle emission from the composite system, as a function of time and emission energy. To calculate pre-equilibrium cross section many different models were formulated: classically (*the exciton model*) and quantum-mechanically (*multi step models*). The exciton model was the first model that has been introduced, and it has been later improved with successive refinements to take into account more physical features in order to improve its predictive power [62]. The quantum-mechanical models can be subdivided into MultiStep Compound (MSC) and MultiStep Direct (MSD) according to which energy region has to be considered: low or high energy region. The multistep models represent a more natural link to the theories for compound nucleus and direct reactions (which are described by quantum-mechanics) and, even if they give a more precise information about the angular distribution [51, 56], they are more complex and less flexible [62]. In this section only the exciton model is briefly presented, while for a complete description please refer to Refs. [63, 64, 65].

This model is based on the concept of excitons that are the set composed by the particles above and the holes below the Fermi level. Once the projectile enters the nucleus, it interacts with the particles of the Fermi sea, and in the first step a state is formed with a number of excitons $N = 3$. This state is the first one possibly subject to particle emission, but subsequent multiple collisions of the projectile with the target nucleons can occur resulting in configurations with different number N. In general, the number of excitons can change by $\Delta N = 2$ when a new particle-hole pair is created, by $\Delta N = -2$ when an existing particle-hole pair annihilates or by $\Delta N = 0$ when trivially the number is unchanged. Thus the cross section of this reaction is obtained considering the time evolution of the number N as the reaction progresses step by step through the intranuclear interactions, in the assumption of an equal probability of different particle–hole configurations with the same number N. A schematic representation of the flow of the reaction is shown in Fig. 2.4, where the probability of emission of a particle is non-zero for each stage. Moreover,

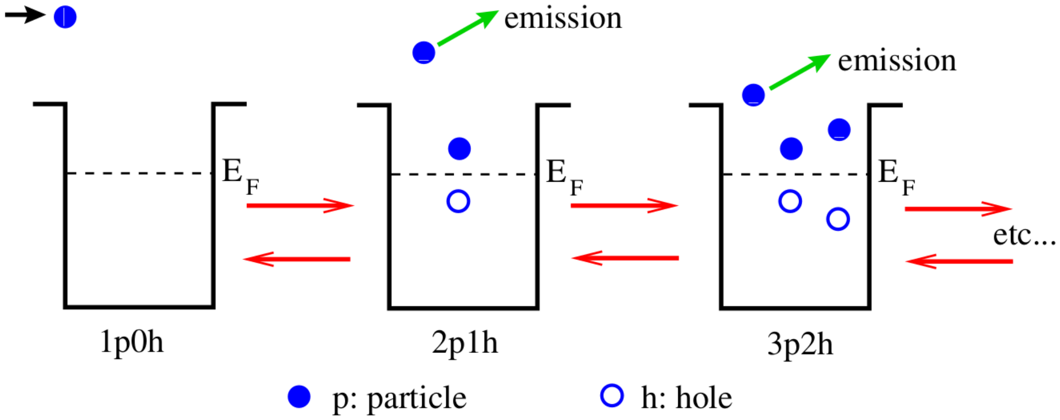

Figure 2.4: Schematic representation of the flow of the exciton model for the pre-equilibrium process [51, 56]. On the left the initial stage is represented with the entrance of the projectile in the target (1 particle 0 holes, thus $N = 1$). Then the projectile interacts with nucleons and different particle-hole pairs can be created ($N = 3, 5, ...$). Apart the first stage, in all the others the probability of emission of a particle is non-zero.

for high incident energies the composite nucleus is so excited that can decay also by further particle emissions (*multiple emissions*). The integration over time of the probability of these transitions allows to obtain an energy-averaged emission spectrum. A similar model is suitable to be implemented in codes as described in the next section, where the attention is focused on the parameterization of the transition rates between two exciton states that are in general calculated starting from the Fermi's golden rule:

$$\lambda = \frac{2\,\pi}{\hbar}\,M^2\,\omega, \tag{2.9}$$

where the dynamics of the interaction is described by the matrix M that has to be well parameterized, while ω represents the final state density[1].

All these processes (i.e. direct reactions, compound nucleus and pre-equilibrium mechanisms) contribute to the final description of a nuclear reaction and, to ease the calculations of the involved physical quantities, different calculation codes were developed. Thanks to these tools they have become in the last years an accessible theoretical reference for the nuclear Physics community, in particular for the research on medical isotopes.

2.2 Models: the TALYS code

TALYS [51, 56] is a software for the simulation of nuclear reactions that includes many state-of-the-art nuclear models to cover most of the reaction

---

[1] In this equation, the notation of the TALYS manual is used

p/n	d		α	
model	model		model	
KD	**1**	**Normal deuteron potential** [70]	1	Normal alpha potential [51]
JLM	2	Daehnick et al. [71]	2	McFadden and Satchler [72]
	3	Bojowald et al. [73]	3	Demetriou and Goriely, tab. 1 [74]
	4	Han et al. [75]	4	Demetriou and Goriely, tab. 2 [74]
	5	Haixia An et al. [76]	5	Demetriou and Goriely dispersive [74]
			6	**Avrigeanu et al.** [77]
			7	Nolte et al. [78]
			8	Avrigeanu et al. [79]

Table 2.2: Optical potential models used in TALYS for protons and neutrons (p/n), deuterons and α particles. KD: Koning-Delaroche, JLM: Jeukenne, Lejeune and Mahaux. The default models are highlighted.

mechanisms encountered in light-particle induced nuclear reactions. TALYS provides a complete description of all reaction channels and observables and in particular takes into account all types of direct, pre-equilibrium, and compound mechanisms to estimate the total reaction probability as well as the competition between the various open channels: in particular the code is able to calculate total and partial cross sections, residual and isomer production cross sections, discrete and continuum γ ray production cross sections, energy spectra, angular distributions, double-differential spectra, as well as recoil cross sections.

The code is optimized for incident projectile energies ranging from 1 keV up to 200 MeV on target nuclei with mass numbers between $A = 12$ and $A = 339$. It includes photon, neutron, proton, deuteron, triton, ^{3}He, and alpha particles as both projectiles and ejectiles, and single-particle as well as multi-particle emissions and fission. All experimental information on nuclear masses, deformation, and low-lying states spectra is considered, whenever available. If not, various local and global input models have been incorporated to represent the nuclear structure properties, optical potentials, level densities, γ-ray strengths, and fission properties.

For each process described in the previous section, all the cited models are implemented in the code (like the Hauser-Feshbach formalism, the exciton model, the MSC/MSD model, and different models for the level density). For the optical potential, the phenomenological *Koning-Delaroche* model [66] has been implemented in addition to the microscopic JLM (Jeukenne, Lejeune and Mahaux) model [67, 68, 69] for protons and neutrons, while a wider choice is available for deuterons and α particles. Tab. 2.2 summarizes the optical potential models (the default options are highlighted) implemented in TALYS for incident neutrons, protons, deuterons and α particles. They are particularly relevant in this thesis for the study of the three generator reactions.

Besides the use of the code as a tool to study nuclear reactions, there is also the possibility to use it together with other tools that perform an automatic global optimization to experimental data and that determine the nuclear model based covariances. In this way TALYS can be used to generate nuclear reaction data libraries, as TENDL (TALYS-based evaluated nuclear data library) [80], to provide information for new nuclear technologies. This library is increasingly growing and is one of the most used, especially in the field of medical radionuclide production: it represents a theoretical reference for a comparison with experimental data or for a preliminary analysis of nuclear reactions when data are not available. Moreover, in support of this aspect, in the TALYS code routines devoted to medical radionuclide production have been implemented and can be used to calculate activities of the nuclides produced in a given reaction. However, in some cases, the constructed data library, or the default TALYS calculation, does not provide an adequate description of particular cases and specific refinements have to be performed.

Indeed, in general, to treat a nuclear reaction computationally considering all the possible physical properties, different considerations have to be made from both a numerical and a physical point of view, before the actual calculation is performed. Hereafter a brief description is shown about the considerations performed and used in this study, while for a complete technical description of the code it is suggested to refer to the manual [51]. This step is essential to optimize the TALYS code results by tuning the code on the specific problem under exam: only looking to these details allow to go beyond the mere execution of the code and to reach a deeper comprehension of the underlying physics.

2.2.1 Numerical considerations: energy binning

The first consideration regards the treatment of the formation and decay of the compound nucleus from a numerical point of view. Indeed, the compound nucleus can be formed in any energy level and its decay occurs by means of gamma de-excitation. Theoretically, this stage proceeds through a cascade of consecutive photon emissions, until the ground state is reached. All photons are emitted isotropically, since from the evaporation stage no information on the residual nucleus spin and polarization is available. The cascade is assumed to be statistical as long as the excitation energy is high enough to allow the definition of a continuous nuclear level density. Below a (somewhat arbitrary) threshold, the cascade goes through transitions between discrete levels, while the last steps consist of transitions among these levels, down to the ground state.

To perform the calculations in a computer program the continuum must be discretized in excitation energy bins. In TALYS, transitions from the continuum are treated statistically, due to many overlapping levels, and when known levels are tabulated, the cascade is forced to pass through them. In this code the user can choose between two different binnings: linear or logarithmic, controlled with the `equidistant` option. The two binnings generate different gamma intensities in the nucleus spectrum: this reflects in different cross sections for all nuclei. The effects of the choice of a particular binning are more important at high energy, but are also visible down to threshold.

This behaviour (that can be seen as problem or as a "feature" of the code) is known to the authors of TALYS: the default for the `equidistant` option has changed with time. The first version of the code, TALYS 1.0 (2007), was released with linear bins, while the logarithmic ones were introduced with TALYS 1.6 (2013). The default option was the logaritmic binning until the latest version currently available, TALYS 1.96 (2021), when linear binning was restored to be the default option since an equidistant energy grid was reported to produce better agreement of the cross sections with experimental data [51]. Neither option is right or wrong, and, indeed, the authors have given to the users the possibility to choose among the two binnings.

Anyway, in general, the choice of the proper binning has always been an open problem without a unique solution, since it depends from case to case. Therefore it is evident that the number of bins is a crucial parameter that affects the accuracy of the results. TALYS, concerning the linear binning, offers two possibilities:

- the use of a constant number of bins (this is the default, with the keyword `bins 40`);
- the use of an energy dependent algorithm that produces a reasonable number of bins that take into account the fact that more bins are needed when the incident energy increases:

  $$N_{\text{bins}} = 30 + 50\frac{E^2}{E^2 + 60^2} \tag{2.10}$$

  achievable using `bins 0`.

The produced number of bins is close to the commonly accepted values provided by other statistical and data analysis codes, such as ROOT for example, that follows the rule n. of bins $\approx \sqrt{\text{n. of entries}}$.

The choice of the binning has been extremely important in this study. As it will be shown, in the analysis of the cross sections for all the three nuclear reactions we achieved a better agreement with the experimental data by first fine tuning the TALYS binning options. As following steps, we made other considerations on the physics of the studied reactions.

2.2.2 Physical considerations on the different nuclear processes

Direct reaction with deformations

The first physical consideration refers to the use of the coupled-channels formalism to describe direct reaction for deformed nuclei. Indeed, as explained before, the various nuclei produced in the considered reactions, lay in the mass number range $150 < A < 190$, and this formalism has to be considered. Usually the coupled-channels calculations are based on rotational optical potentials where the radius has the expression of Eq. 2.2, while the Koning-Delaroche optical potential (the one used in this work) is known to be spherical. Nonetheless, TALYS allows to perform coupled-channels calculations through the ECIS-06 code [81, 82], (one of the different and available codes used in this context): an empirical modification is done in order to describe the deformation of the nuclei [51]. In particular, for rotational non-fissile nuclides, like the ones involved in this work, TALYS uses the Koning-Delaroche potential and subtracts 15% from the parameter (d_1) that adjusts the width of the imaginary surface potential U_D of Eq. 2.1, if rotational levels are included in the coupling scheme databases inside the code. Probably more accurate approaches will be developed in future, but at the moment this empirical method produces interesting results. Specifically, TALYS prepares the input file for the ECIS code once specific keywords are activated. The most relevant ones are:

- `spherical`, to treat all nuclei as spherical and perform DWBA calculations for the direct reactions. It is a boolean keyword and its default value is `spherical n`;
- `rotational`, to enable or disable rotational optical model and coupled-channels calculations for the various particles in the calculations, provided a coupling scheme is given in the deformation database available inside the code. The default value is `rotational n p`, thus performing the calculations considering only neutrons and protons and not complex particles;
- `autorot`, to enable automatic coupled-channels calculations for nuclide with $A > 150$. In this case, the lowest rotational band is identified by inspecting the discrete levels database. Also this keyword is boolean and its default value is `autorot n`;
- `maxrot`, to specify the maximum number of excited levels to consider in a rotational band in the coupled-channels calculations. The default value is 2 and the maximum is 10;
- `maxband`, to specify the maximum number of vibrational bands to be included in the rotational coupling scheme. The default value is 0 and the maximum is 10.

In this work the combination of `rotational` and `autorot` is used to force the code to perform coupled-channels calculations, starting from the lowest rotational energy levels, as shown in the next chapter. In particular the last two parameters have been thoroughly evaluated and the default values have been used. In this way, the theory is exploited considering correctly the physics of the problem without empirical or handmade modifications of the optical potential parameters.

Considerations can be made for all the other nuclear reaction processes, for a proper use of the options of the code to better describe the cross sections.

Pre-equilibrium process: exciton model parameterization

Following the procedure described in Ref. [83], the attention is mainly focused on the pre-equilibrium mechanism and on the variation of its parameters, that allows to avoid a greater "change of the physics" (as reached with an excessive variation of the optical potential or level density parameters), but instead allows to vary the evolution and the emission rate that are not known accurately.

As we have seen before, the exciton model is implemented in the TALYS code with a proper parameterization of the transition rates. More specifically, considering a proton (π)-proton (π) collision that creates a new particle-hole pair ($1p$) the corresponding transition rates is written, according to Eq. 2.9 and using the notation of the TALYS manual, as:

$$\lambda_{\pi\pi}^{1p} = \frac{2\,\pi}{\hbar}\, M_{\pi\pi}^2\, \omega \tag{2.11}$$

where the final state density ω depends on the exciton state configuration and excitation energy, as formulated by Dobeš and Běták [84]. In TALYS, the matrix is re-written in terms of a total average matrix M^2:

$$M_{xy}^2 = R_{xy}\, M^2 \tag{2.12}$$

where x and y denote any combination of proton π and neutron ν, while R_{xy} is a free parameter with the following default values that can be varied in TALYS:

$$R_{\pi\pi} = 1.0 \quad R_{\pi\nu} = 1.0 \quad R_{\nu\pi} = 1.0 \quad R_{\nu\nu} = 1.5 \tag{2.13}$$

For the matrix M^2 a semi-empirical expression has been written and has been shown to work for incident energies between 7 and 200 MeV:

$$M^2 = \frac{C_1\, A_p}{A^3}\left[7.48\, C_2 + \frac{4.62 \times 10^5}{\left(\frac{E^{tot}}{n\, A_p} + 10.7\, C_3\right)^3}\right] \tag{2.14}$$

where A and A_p are the mass number of the target and of the projectile while n is the total exciton number. The other parameters C_1, C_2, C_3 are adjustable constants equal to 1 by default and they can be varied using the following keywords: `M2constant`, `M2limit`, `M2shift`. In particular, an increase of the overall constant C_1 corresponds to a lowered energy tail, while an increase of C_2 (that controls the asymptotic behaviour) allows to prevent an overestimation of the tail. On the other hand, C_3 has effect on the energy of the system and the corresponding keyword `M2shift` can be used to vary the strength of the exciton model along the energy axis of the projectile [83].

Among the pre-equilibrium models implemented in the code, the exciton models based on Eq. 2.14 can be invoked with the `preeqmode` keywords, in particular with `preeqmode 1` or `preeqmode 2` for analytical or numerical solution of the equations respectively. There is also a third option for the pre-equilibrium process based on the exciton model, in which the transition rate is related to an average optical model potential depth instead of an average squared matrix. In this approach, the final expression of the cross section depends only on a single parameter whose values can be varied in the code using again the keyword `M2constant` [51]. Moreover, in the “standard” versions of TALYS, developed and mantained by the three authors Arjan Koning, Stephane Hilaire and Stephane Goriely, there is also one last option of the pre-equilibrium models: the microscopic multi-step direct/compound model, whose cross sections can be rescaled with `M2constant`. However, in this thesis the special version of TALYS (v. 1.95G, handled by the Institute for Neutron Physics and Reactor Technology [85]) is used since it allows to consider an additional model for the pre-equilibrium process. This model, called Geometry Dependent Hybrid (GDH) model, is very similar to the exciton model, but the description of the interaction is performed with an explicit dependence on the geometry of the system [86, 87, 88, 89, 90], by means of the initial impact parameter and of the distribution of the nuclear density. In particular the dependence of these two quantities allows to obtain a better description of the high-energy tail. Initially, a nuclear code was created upon this model (the ALICE code [91]) and only later it has been implemented inside the modern TALYS code. However, in TALYS the parameters of this model are not easily accessible by the user and the model is offered as a “black-box”. Therefore the attention is focused on the exciton models, considering also the multiple emissions (with the `multipreeq` and `mpreeqmode` keywords) and the spin distribution for the residual nuclei (invoked with `preeqspin`), for an improvement of the cross sections, as discussed in the next chapter.

Other processes induced by complex particles

When considering reaction induced by complex particles, as deuterons and α particles, other phenomena may occur, like:

- *stripping reactions*: one or more nucleons are transferred to the target from the projectile (ex. ^{159}Tb(d,p)^{160}Tb);
- *pick-up reactions*: one or more nucleons are transferred from the target to the projectile (ex. ^{159}Tb(p,d)^{158}Tb);
- *break-up reactions*, when a break-up of the projectile into one or more fragments occurs (ex. d + ^{159}Tb $\rightarrow$^{159}Dy + n);
- *knock-out reactions*: a single nucleon or a light cluster is removed from the target by the projectile during their interaction (ex. ^{nat}Gd(α, x)^{159}Gd).

In particular the *break-up* process plays an important role in this work. This direct-like process has been initially observed by Oppenheimer [92] and later explained by Dancoff [93] and Serber [94]. Their theories are based respectively on the Coulomb excitation of the deuteron (elastic break-up) and on the nuclear process in which the proton (or neutron) is "stripped" away from the neutron (non-elastic break-up). In the latter description, either the energy, a particle or both are transferred to the target nucleus through a nuclear interaction, and the total cross section exhibits particular features. The energy distribution of protons (or neutrons) is centered around half the deuteron energy and the angular distribution of protons is highly forward peaked. The current models are based on the Serber theory (and on further corrections to include the elastic break-up, as the one proposed by Glauber [95]) and they include semi-empirical formulae fitted to experimental data. Examples of these recent models are the one proposed by Kalbach [96] and the one by Avrigeanu [97, 98, 99], but these phenomenological approaches not always show good agreement with neutron yield data. This is due to the fact that they were mostly fit to (d,p) and (d,n) reaction data on medium-mass nuclides and might give different results on lighter or heavier nuclei. Moreover, this discussion regards also α particles which have double the charge of a proton, leading to a much stronger Coulomb interaction. Consequently also for these reaction binary breakup and fragmentation processes in the target are very important and other specific models have been developed for this case. In general different parameterizations were provided by the authors to improve the agreement with experimental data and all these models are available in the TALYS code. Therefore different parameters have been added to take into account the contribution of these processes and they can be invoked with the `Cstrip`[2], `Cknock` and `Cbreak` keywords.

The values of all the pre-equilibrium parameters can be varied, within their limits, to better reproduce the cross sections in comparison with available experimental data, and have been extensively considered in this work.

Level density models and parameters

In addition to the variation of the parameters of the pre-equilibrium process, also minor changes on the level density can be made to locally adjust the cross sections of specific nuclides maintaining the global description.

There are six models for level density implemented inside the code: three phenomenological and three microscopic. Among them, the attention of this work has been focused on the three microscopic ones due to their higher flexibility and modernity. In particular, as described in the manual [51] and also in RIPL (Reference Input Parameter Library) [100], theoretical level densities ρ_{HFM} (calculated with Hartree-Fock methods) are tabulated and can be re-normalized with the following scaling function:

$$\rho(E, J, \pi) = \exp\left(c\sqrt{E-p}\right)\rho_{HFM}(E, J, \pi). \tag{2.15}$$

By using this relation, depending on the two parameters c and p, a new level density can be obtained for a specific nuclide. The *pairing shift* p allows to

---

[2] this keyword is used for both the stripping and pick-up reactions

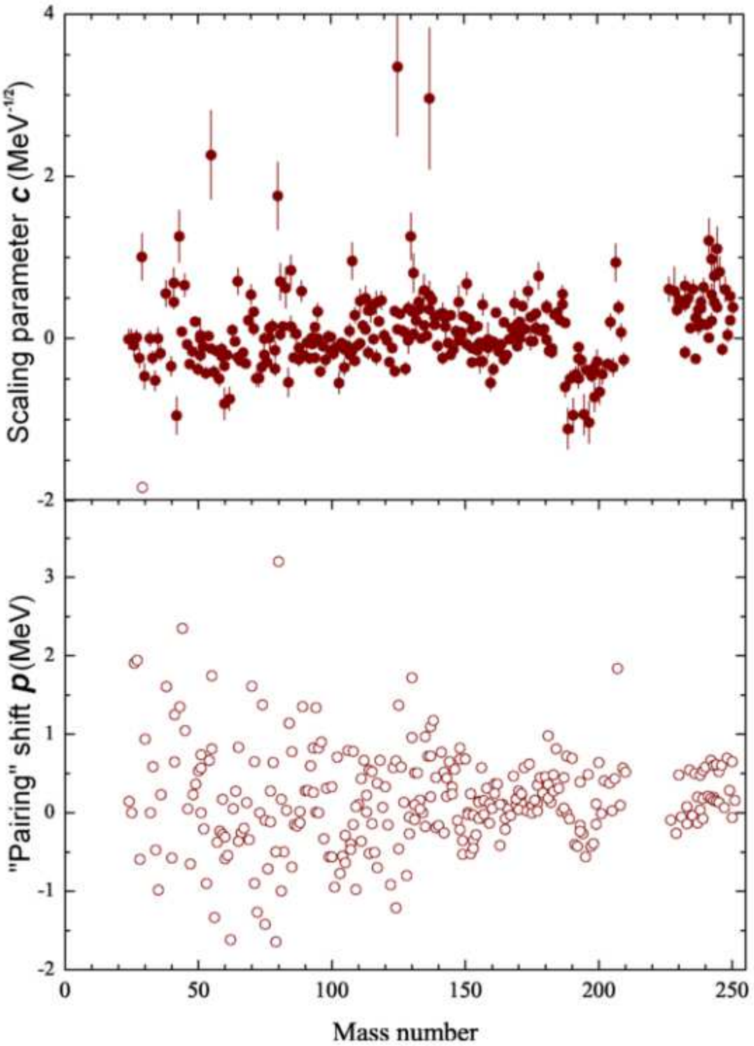

Figure 2.5: Values of the parameters obtained in the fitting of Hartree-Fock method to the experimental data on the low-lying levels and the neutron resonance spacings [100].

retrieve the level density from the tables at a different energy, while c is similar to the level density parameter a of the phenomenological Fermi Gas model (Eq. 2.8): it acts as an overall normalization parameter, increasing or decreasing the magnitude of the tabulated level density [101, 102]. In particular, these parameters can be varied within the range [-10,10] and their adjustment allows to reproduce as well as possible both discrete levels and the mean resonance spacings for the RIPL library. Usually a smaller range is sufficient, as indicated in Fig. 2.5 that shows the values of the parameters obtained in the fitting of Hartree-Fock method to the experimental data on the low-lying levels and the neutron resonance spacings. The parameter c remains often close to zero and this indicates that the normalization does not modify the energy dependence of the microscopic model. The variation of these parameters has consequences

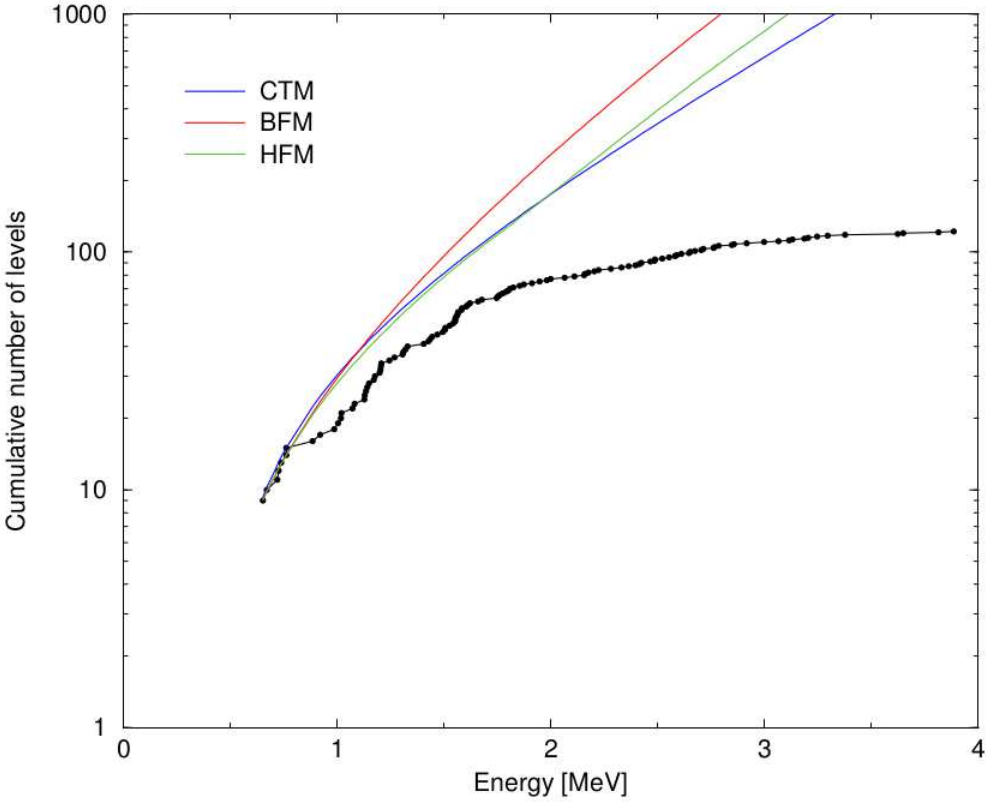

Figure 2.6: Comparison of cumulative number of levels (colored lines) of ^{99}Tc with experimental data (black points) for three different level density models: CTM (Constant Temperature Model) and BFM (Back-shifted Fermi gas Model) are phenomenological, while HFM (Hartree-Fock Method) is microscopic. The details of this figure can be found in the TALYS manual [51].

mainly on two observable quantities: the cumulative of the levels and the reaction cross sections. The cumulative of the levels is obtained by integrating the level density over the energy:

$$N(E) = \int_{E}^{E+\Delta E} \rho(E')dE' \tag{2.16}$$

and, as the cross section, can be compared with experimental data as shown, for example, in Fig. 2.6. In order to obtain a better agreement between the theoretical cross section and experimental data, the variation of c and p should be performed considering simultaneously both the cross section and the cumulative. This should be done to avoid too large modifications of the description of the cumulative of levels that contains information of the nuclear structure. Moreover, the TALYS code is very flexible and offers the possibility to consider, in a single run, different level density models per each nuclide involved in a given reaction. Thanks also to this possibility, the variation of the two parameters represents a minor change that is done a posteriori to improve locally the description of the reaction.

2.3 A Monte Carlo approach: the PHITS code

Besides nuclear reaction codes, like TALYS, many other tools, like Monte Carlo codes, can be used when preparing for the production of radionuclides. These codes are normally used to simulate and study high energy physics problems, but are becoming an option also in the field of low energy physics with the refinements of their models. Examples of common Monte Carlo code used also in low energy physics are MCNP [103], FLUKA [104], GEANT4 [105] and PHITS [106]. In particular PHITS (Particle and Heavy Ion Transport code System) is a general purpose Monte Carlo code developed and maintained mainly by JAEA (Japanese Atomic Energy Agency) in collaboration with other Japanese research centres like KEK and RIST and many other institutes. The code is used for modelling particle transport and interaction with matter covering an extended range of applications: accelerator shielding, calorimetry, dosimetry, detector design, radiotherapy, space radiation and more. It can deal the transportation of all the particles over wide energy range (from 0.1 meV for neutrons to 1 TeV per nucleon for incident nuclei). Therefore the code allows to perform a realistic simulation of a nuclear reaction by defining the beam profile, the geometry of the target and by specifying if the target is a pure element or a compound. Therefore PHITS, as many other Monte Carlo codes, allows to reproduce a counting experiment and to calculate the reaction cross section by its very definition. Indeed, the code calculates and returns the number of nuclides N_p for each chemical species produced in the reaction. From this, knowing the properties of the beam like the number of projectiles N_i and their energies, and the properties of the target, like its density ρ, its mass M, its thickness Δx and the number of the diffusive centers in the target f, the cross section can be calculated with its definition formula:

$$\sigma = \frac{N_p}{f\, N_i\, \rho\, \frac{N_A}{M}\, \Delta x}$$

where N_A is the Avogadro number. In particular, the code provides a statistical uncertainty associated to the number of nuclides N_p: this will reflect in the final calculation of the cross section.

Anyway, to calculate N_p the code relies on data libraries and on different models which can be chosen for the description of a nuclear reaction. In the energy range considered in this work (1–100 MeV), the default model used for light particle induced reactions (from proton to α particles) is the INCL (Intra-Nuclear Cascade of Liège) [107] coupled with the generalized evaporation model (GEM) [108, 109], as presented in the manual. For neutron induced reactions, the default is that the INCL coupled with the GEM is used for energies above 20 MeV, while below 20 MeV the JENDL-4.0 library is used. The combination of these models allow to describe the formation and decay of the intermediate system composed by the projectile and the target nucleons, tracking in time all their possible interactions. Therefore these models embody (not explicitly) the three reaction mechanisms described before: the formation and decay of the compound nucleus, the pre-equilibrium process and the direct reaction.

However, with respect to TALYS, PHITS provides fewer models, whose parameters can not be easily varied to obtain a better description of the cross sections. Nevertheless, in the latest versions, these codes allow to use tabulated cross sections, that can be calculated for instance using TALYS, instead of the models, to simulate the experiment. In addition, TALYS may be coupled with INCL codes in future [56] to treat the pre-equilibrium mechanism both at lower and higher energies (over 200 MeV). In this way these codes combine a stronger theoretical description (provided by the nuclear reaction code) with all the useful information and quantities involved in an experiment (provided by the Monte Carlo codes). Therefore they allow to avoid wrong predicted yields or also higher production of undesired nuclides, that are important aspects in this field, as will be shown in the next section.

Moreover, PHITS allows to calculate also important quantities like the yield and the activity for each produced nuclide at times specified by the user, following its decay chain using the DCHAIN-SP module. Therefore this code can be used alone or combined with a nuclear reaction code to study the production of medical radionuclides.

In this thesis, this code has not been deeply investigated (as done for the TALYS code for the cross sections), due to the greater complexity to access and modify the parameters of the used theoretical models: in PHITS only a few global control parameters to choose among the different models are available for the normal user in the input file. A more advanced approach would still be possible, since the source code is available and could be modified and recompiled. However this is not recommended and not attempted in this thesis, where PHITS has been used to perform the same yields and purities calculations carried out with TALYS and to verify the results with an independent code, as often done in the literature [110, 111, 112, 113].

2.4 Production studies

As described in the previous sections, both TALYS and PHITS provide routines to study the production of medical radionuclides, calculating some quantities like yield and activity of each nuclide produced in a given reaction. However other quantities have to be calculated, like the purity of the final product in view of its clinical applications. Moreover, these codes do not treat the cases of generator systems, but only the direct production of radionuclides. For this reason, the problem has to be delineated and the quantities of interest have to be properly studied and implemented in a specific code for an appropriate treatment of the cases under consideration, especially to evaluate the timings of the chemical separations.

2.4.1 Production rates and Bateman equations

The production of a nuclide with cyclotrons is obtained with the interaction of a beam of particles of different energies with a target. The expression of its production rate is the following[61]:

$$R = \frac{I_0}{z_{proj}|e|}\frac{N_A}{A}\int_{E_{out}}^{E_{in}} \sigma(E)\left(\frac{dE}{\rho_t dx}\right)^{-1} dE \tag{2.17}$$

where I_0 is the charge beam current (measured in ampere), z_{proj} the atomic number of the incident particle, e the electron charge, N_A the Avogadro number, A the target atomic mass, E_{in} and E_{out} are respectively the energy of the incident particles (corresponding to the maximum value of the energy window) and the energy of the outcoming particles calculated by taking into account the thickness of the target. $\sigma(E)$ is the cross section of the considered reaction, and $\frac{dE}{\rho_t dx}$ is the *stopping power*. Its expression is given by the Bethe-Bloch formula [114], that, without the shell and density corrections, is:

$$-\frac{dE}{\rho_t dx} = 2\pi N_A r_e^2 m_e c^2 \frac{Z}{A}\frac{z^2}{\beta^2}\left[\log\left(\frac{2m_e\gamma^2 v^2 W_{max}}{I^2}\right) - 2\beta^2\right]. \tag{2.18}$$

It describes the energy loss of the incident particles in the target (due to their interaction with the target atoms) as a function of the travelled distance and of the density of the target (ρ_t). In this equation r_e is the classical electron radius, m_e the electron mass, c the speed of light in the vacuum, Z and A the atomic number and atomic mass of the target, z and v are the charge and the velocity of the incident particle. The quantities β and γ are the relativistic factors:

$$\beta = \frac{v}{c} \qquad\qquad \gamma = \frac{1}{\sqrt{1-\beta^2}}.$$

I is the mean excitation potential (expressed in eV), calculated with the empirical relation:

$$\begin{aligned} \frac{I}{Z} &= 9.76 + 58.8\, Z^{-1.19}\, eV && Z \geq 13 \\ \frac{I}{Z} &= 12 + \frac{7}{Z}\, eV && Z < 13 \end{aligned}$$

W_{max} is the maximum energy transfer to an electron of the target by the incident particle with mass M in a single collision:

$$W_{max} = \frac{2m_e c^2\beta^2\gamma^2}{1 + 2\gamma\frac{m_e}{M} + (\frac{m_e}{M})^2}$$

that, if $M \gg m_e$, can be simplified as:

$$W_{max} \cong 2m_e c^2\beta^2\gamma^2.$$

Thus the production rate R depends on the properties of both the absorbing material (the target) through the quantities Z, A, ρ_t, I and the projectile by z_{proj}, I_0, v and indirectly by its mass M which appears within the kinematic parameters β and γ: $\beta\gamma = p/M\,c$.

Note that the expressions of the production rate (Eq. 2.17) and of the stopping power formula (Eq. 2.18) apply only for the case of pure elements, while for compound targets the number of atoms of the desired elements in the molecule has to be considered. More specifically Eq. 2.17 becomes:

$$R = \frac{I_0}{z_{proj}|e|}\frac{N_A\,a_i}{A_{mol}}\int_{E_{out}}^{E_{in}} \sigma(E)\left(\frac{dE}{\rho_t dx}\right)^{-1} dE, \tag{2.19}$$

where a_i is the number of the atoms of the desired element in the target molecule and A_{mol} is the average molar mass of the target. The formula of the mass stopping power is corrected by replacing Z, A, I with their effective values [114]:

$$Z_{eff} = \sum_i a_i\, Z_i \quad A_{eff} = \sum_i a_i\, A_i \quad \ln I_{eff} = \frac{\sum_i a_i\, Z_i\, \ln I_i}{Z_{eff}},$$

where i-index refers to the different elements in the target.

These expressions are used in the case of the reactions with Gd, since the considered target is gadolinium oxide (Gd_2O_3) where $a_i = 2$ and A_{mol} depends on the isotopic abundance of Gd in the target.

Starting from the production rate, another important quantity can be calculated: the *yield*, which is often used in the field of medical radionuclide production. The yield is defined as the number of nuclei produced per induced electric charge, is measured in nuclei/C or MBq/μA and is calculated using the following formula for the case of pure elements:

$$y = \frac{R}{I_0} = \frac{1}{z_{proj}|e|}\frac{N_A}{A}\int_{E_{out}}^{E_{in}} \sigma(E)\left(\frac{dE}{\rho_t dx}\right)^{-1} dE. \tag{2.20}$$

As the rate, also the yield depends on the thickness of the target and we can refer to three different cases:

- **thin target yield**: when the target is thin and the energy loss of the incident particle is negligible ($E_{in} \simeq E_{out}$). The cross section is constant and there is a low production of radionuclides. Usually a thin target is used for cross section measurements.

- **thick target yield**: when the target is thick and the energy lost by the incident particle in the target is no longer negligible ($E_{in} > E_{out}$). The yield is calculated using exactly Eq. 2.20. This is the case considered for the production of radionuclides.

- **integral yield**: when the target has such a thickness that the incident particle loses all its energy and is stopped inside the target, or when the output energy E_{out} is less than the threshold energy of the reaction. Targets of this type are used to compare different reactions that contribute to directly produce the same radionuclide.

In the literature different definitions of yield can be found with an explicit time dependence. They are often used to estimate the quantity of radionuclide produced and available at a given time. To define some of the more commonly used quantities for medical radionuclide production, i.e. activity and "*End-Of-Bombardment*" yield, the time evolution of the number of nuclei produced in the reaction has to be considered, by solving in general the Bateman equations [115].

Different cases can arise, but the time evolution of a specific nuclide, produced with a rate R_i and that decays with decay constant λ_i, can be described in general in the following way:

$$\frac{dN_i(t)}{dt} = R_i - \lambda_i N_i(t) + \sum_j f_{ij}\,\lambda_j\,N_j \tag{2.21}$$

where f_{ij} represents the branching fractions of other possible nuclei N_j (including metastable states) that, decaying, can produce the considered nuclide N_i. From Eq. 2.21, the simplest cases can be easily found concerning:

- stable isotopes:
$$\frac{dN_i(t)}{dt} = R_i$$
- radionuclides produced only by a single reaction:
$$\frac{dN_i(t)}{dt} = R_i - \lambda_i N_i(t)$$

The solution of Eq. 2.21 is obtained by solving numerically the corresponding differential equation system that can be handled in algebraic way using matrices as described in Ref. [116]. In general, in order to write such a system, the decay chains of the involved radionuclides have to be carefully taken into account.

In this work the attention is focused on the following reactions:

$$p + {}^{159}\text{Tb} \rightarrow {}^{155}\text{Dy} + 5n \rightarrow {}^{155}\text{Tb}, \tag{2.22}$$
$$d + {}^{159}\text{Tb} \rightarrow {}^{155}\text{Dy} + 6n \rightarrow {}^{155}\text{Tb}, \tag{2.23}$$
$$\alpha + {}^{nat}\text{Gd} \rightarrow {}^{155}\text{Dy} + xx \rightarrow {}^{155}\text{Tb}. \tag{2.24}$$

Therefore the aim is initially to produce ^{155}Dy and looking at the decay scheme shown in Fig.2.7, its production and decay is simply described by a single equation:

$$\frac{dN_{155Dy}}{dt} = R_{155Dy} - \lambda_{155Dy}\,N_{155Dy}$$

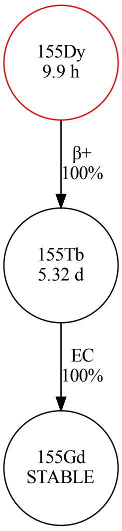

Figure 2.7: Decay scheme of ^{155}Dy as an example of decay chain for the case of interest. The figure is obtained with a program that automatically draws the decay chains and writes the corresponding decay constant matrices (see Appendix A).

which is valid until the end of the irradiation. After this time, the equation is formally similar, but the production rate vanishes: the equation describes only the decay of the produced ^{155}Dy. On the other hand, always looking to Fig. 2.7, the production and decay of ^{155}Tb is described by the following system:

$$\begin{cases} d_t N_{155Dy} = R_{155Dy} - \lambda_{155Dy}\, N_{155Dy} \\ d_t N_{155Tb} = R_{155Tb} - \lambda_{155Tb}\, N_{155Tb} + f_{155Dy\to 155Tb}\, \lambda_{155Dy}\, N_{155Dy} \end{cases}$$

that can be rewritten as:

$$\begin{pmatrix} d_t N_{155Dy} \\ d_t N_{155Tb} \end{pmatrix} = \begin{pmatrix} R_{155Dy} \\ R_{155Tb} \end{pmatrix} + \begin{pmatrix} -\lambda_{155Dy} & 0 \\ +f_{155Dy\to 155Tb}\, \lambda_{155Dy} & -\lambda_{155Tb} \end{pmatrix} \begin{pmatrix} N_{155Dy} \\ N_{155Tb} \end{pmatrix}.$$

This system can be solved using the standard analytical methods or also some computational routines, if one is interested in the direct production of ^{155}Tb as indicated by the presence of the production rate R_{155Tb}. Nevertheless, this thesis is focused on the indirect production of ^{155}Tb, described by a slightly different system that will be presented and discussed in the next chapter.

To generalize and ease the problem of writing and solving similar differential equation systems also for more complex cases, I have implemented a procedure in a Python script that, combining a recent nuclear database [117] with the output of a TALYS run, draws the decay chains of the nuclides produced in a given reaction. This tool allows to avoid the manual search of the needed information on the available online services (like Nudat or the LiveChart of IAEA). The same program allows also to obtain with each graph the corresponding decay constant matrix that is used for the numerical solution of the system. See Appendix A for a schematic description of the script to plot these graphs.

2.4.2 Yields and purities

The solution of the system is used for the calculations of the other useful quantities, as the activity:

$$A_i(t) = \lambda_i \, N_i(t), \tag{2.25}$$

and from that also the "*End-Of-Bombardment*" yield:

$$y_{EOB} = \frac{A_i(t_{EOB})}{I_0} \tag{2.26}$$

defined as the activity per unit of current, calculated at the end of the irradiation. Among all the definitions of yields available in literature [118], other very useful quantities can be defined. One is the *saturation yield*:

$$a_{sat} = \frac{A_i(t \to \infty)}{I_0}, \tag{2.27}$$

that is defined for a very long irradiation time, or more practically for an irradiation time much longer than the half-life of the product. In this condition the production rate and the decay rate of the product are in equilibrium [118]. On the other hand, another quantity is the *physical yield*, defined as:

$$\alpha_{phys} = \left.\frac{d(A_i(t)/I_0)}{dt}\right|_{t=0}. \tag{2.28}$$

Usually it is combined with the previous definition of integral yield, resulting in the *integral physical yield*: this is one of the most used quantity in the field of medical radionuclide production. It allows a general and precise comparison of different production routes, based on the use of different projectiles and targets, for the direct production of a specific radionuclide. Moreover, other combinations can be defined to compare generator-like reactions, as it will described in Chapter 5. In general, from such a comparison, the reaction with higher value of yield is preferable. However, these quantities have to be calculated not only for the radionuclide of interest but also for all its isotopes (the *contaminants*).

Indeed, as presented in the previous chapter, this work contributes to the activities of the REMIX project which is based on the direct activation technique. Therefore, it is not possible to extract only a single nuclide, since radiochemistry allows to extract the chemical element we are interested in (^{155}Tb in our case) with all its isotopes. They decay emitting radiation of different types that could be harmful to the patient: therefore their production must be carefully evaluated and minimized. For this purpose, an accurate analysis has to be performed for all the parameters that affect the yield as: the energy and the current intensity of the incident beam, the irradiation time, the cooling time (waiting time after the irradiation), the target properties (as its thickness and composition). In particular, an approximate indication of the best energy or energy window (and thus of the thickness of the target) can be obtained with a preliminary analysis of the cross section ratio between the cross section of the nuclide of interest and the sum of the cross sections of all the nuclides of the considered chemical element:

$$r = \frac{\sigma_i}{\sum_j \sigma_j}. \tag{2.29}$$

In practice three quantities are very useful in this context: isotopic purity, radionuclidic purity and specific activity.
The isotopic purity (IP) and the radionuclidic purity (RNP) are defined by the ratios:

$$IP(t) = \frac{N_i(t)}{\sum_j N_j(t)} \tag{2.30}$$

$$RNP(t) = \frac{A_i(t)}{\sum_j A_j(t)} \tag{2.31}$$

that show at a specific time t, respectively, the amount of the produced nuclide i and its purity among all the other nuclides of the same element. In particular, the ideal case of $RNP = 1$ indicates a product composed only of the nuclide of interest, therefore emitting only the desired radiation. Values of $RNP < 1$ indicate the presence of contaminants, which could emit harmful radiation to the patient or not useful for clinical purposes. Among these two quantities, the European Pharmacopoeia has imposed a lower limit over the radionuclidic purity: it must be greater than or equal to 99% [119].

Another useful quantity is the specific activity defined as:

$$SA(t) = \frac{A_i(t)}{\sum_j m_j} \tag{2.32}$$

the ratio between the activity of the nuclide of interest and the mass of all the produced nuclides of the same species. Also this quantity describes the amount of the produced nuclide i among its isotopes, more from a radio-chemical point of view.

In the next chapter all the results, obtained on the basis of the theory and codes described here, will be shown and analyzed for all the reactions with protons, deuterons and α particles. The first step is represented by an accurate description of the experimental cross sections using the nuclear code

TALYS, to define the routes and calculations for an optimal production of ^{155}Tb.

Chapter 3

Cross section results

In this chapter the results of the study of the cross sections are presented and compared with the experimental data for all the three reactions considered in this work. On the basis of the theory presented in the previous chapter, a study has been performed for each specific reaction by using the TALYS code, selecting the proper models and varying (when necessary) their parameters to obtain a better description of the cross sections especially of the dysprosium isotopes.

Indeed, since the considered reactions are generator-based reactions, the attention has to be focused initially both on ^{155}Dy and on its isotopes because, after the irradiation, they will be extracted from the target and by decay produce the nuclide of interest (^{155}Tb) and all its contaminants. In particular among all the different dysprosium nuclides produced in the reactions, only four radionuclides are relevant for this study: ^{153}Dy, ^{155}Dy, ^{157}Dy and ^{159}Dy, for which experimental data are available, with the exception of ^{153}Dy in the reactions with deuterons and α-particles, as shown in the review of the data in the first chapter. Many nuclides are stable (^{156}Dy, ^{158}Dy, ^{160}Dy, ^{161}Dy, ^{162}Dy, ^{163}Dy and ^{164}Dy), one (^{154}Dy) has a very long half-life ($T_{1/2} \simeq 3$ My) and all the others are produced at energies higher than the ones achievable with the INFN-LNL SPES cyclotron (70 MeV).

An accurate description of the cross sections is extremely important since an underestimation or overestimation could lead to wrong calculations of activities and purities.

An important note is necessary at this point: this study is concerned to the practical applications of the final product, i.e. ^{155}Tb, and an accurate description of the cross section of every reaction channel involved in the related decay chains is not the main goal of this thesis. Nevertheless, for completeness, the effect of the used improvement approach has been examined considering also other nuclides for which experimental data are available, like terbium and gadolinium.

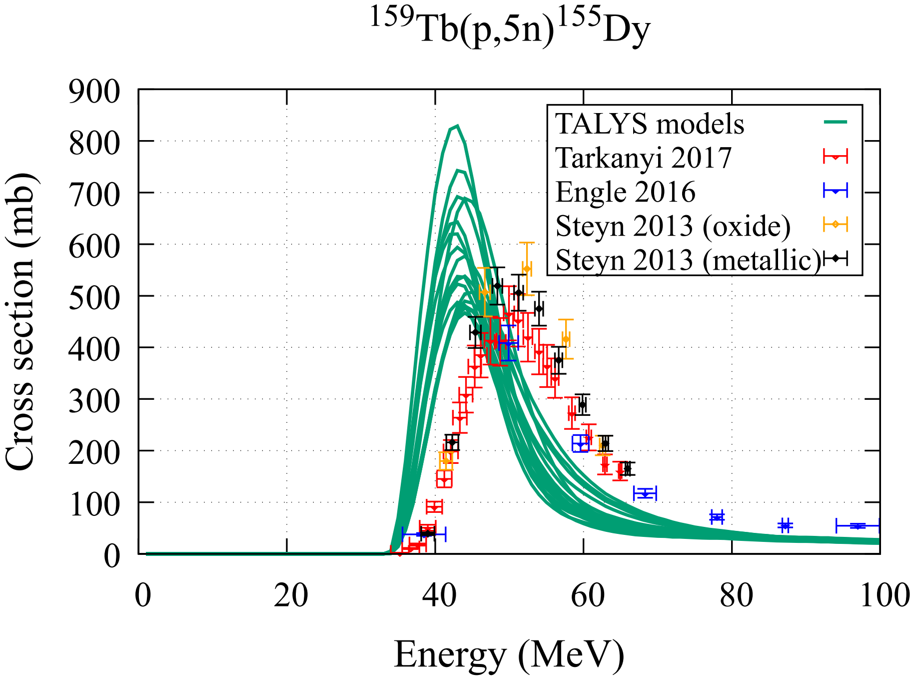

Figure 3.1: Different combinations of pre-equilibrium and level density model with default options for optical potential and energy binning.

3.1 Reactions with protons

The reaction with protons on natural terbium has been the first reaction studied in this work and its analysis has revealed insights and properties useful also for the other two reactions. For this reason, the main steps of the used procedure for the investigation of this reaction are shown to clarify their meaning and impact on the cross sections. Initially different TALYS calculations have been performed to explore all the possible combinations of pre-equilibrium and level density models, while using the default options, for all the other models (like the optical potential) and also for the excitation energy binning. This first investigation has been carried out to outline the physical situation and the behaviour of the models in comparison with the data, as shown in Fig. 3.1 for the case of ^{155}Dy. The theoretical curves do not reproduce the position of the peak of the cross section and, instead, appear to be shifted to the left with respect to the different available experimental data which are in agreement with each other. From this step the approach for a better description of the cross section has been set up, following a procedure similar to the one presented in Ref. [83]. The behaviour of the theoretical curves has been greatly improved initially with considerations of numerical nature, using the linear binning which is not the default option in the version of the code used in this work. In particular a better description has been obtained with a number of bins given by the energy dependent algorithm which produces the results

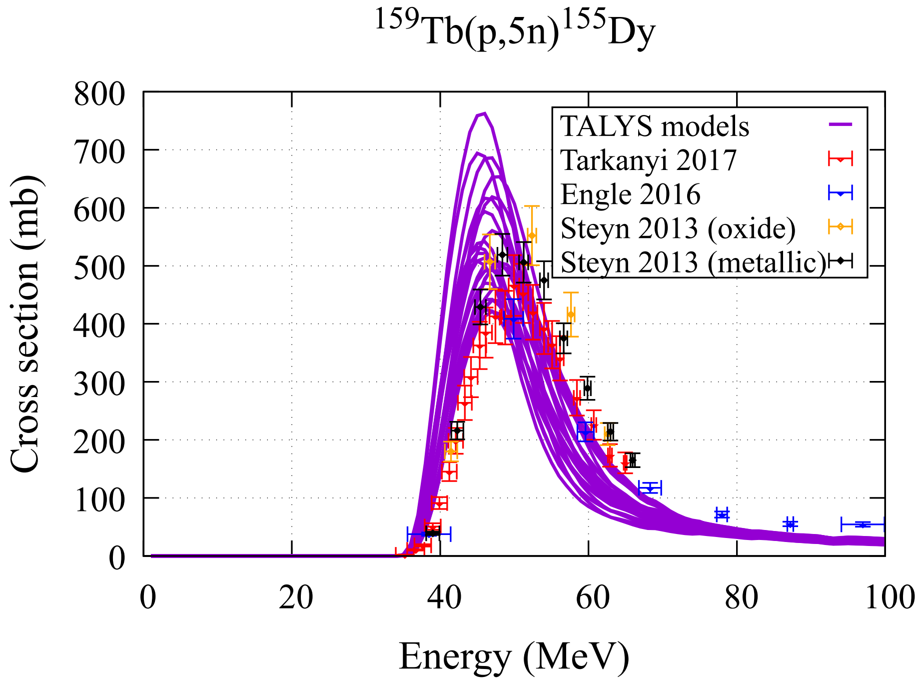

Figure 3.2: Different combinations of pre-equilibrium and level density model with default options for optical potential but with equidistant excitation energy binning (the combination of `equidistant y` and `bins 0` has been used).

shown in Fig. 3.2.

Moreover the coupled-channels approach has been used since the considered nuclides are known to be deformed, resulting in a further slight shift to the right of the curves. This is mainly caused by the modifications of the parameters of the imaginary part of the optical potential implied by the automatic coupled-channels calculations, which have been activated using the following keywords: `rotational n p d a` and `autorot y`. These commands allow to enable the calculations starting from the lowest rotational band for the various particles that can appear in the calculations, that is neutrons, protons, deuterons and α-particles. The inclusion of ^{3}H and ^{3}He has been considered as well, but no difference has been observed in the cross sections of all the considered nuclides: however their exclusion in the calculations has allowed to reduce the computational time.

The effect of these improvements can be noticed from Figs. 3.3-3.4 for ^{155}Dy and ^{153}Dy respectively. In these figures the curve obtained considering both linear binning and the deformation of the nuclides is shown and compared to the one obtained without these considerations, for simplicity only for a combination of pre-equilibrium and level density models. The improvements are remarkable especially for ^{153}Dy, but also the cross sections of the other dysprosium nuclides (^{157}Dy and ^{159}Dy) have been well reproduced.

Only after the global choice of binning and the inclusion of rotational effects

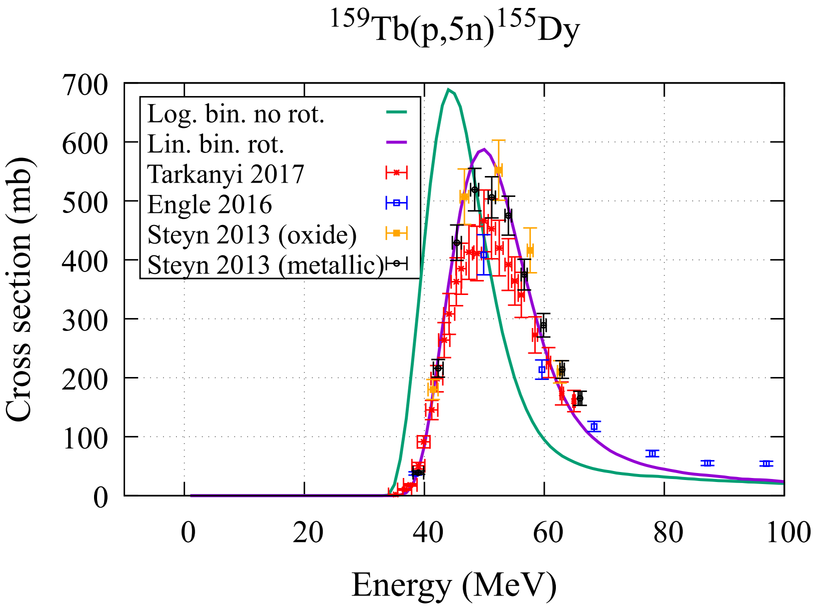

Figure 3.3: Effects of initial improvements for ^{155}Dy. Purple line: linear binning and coupled-channel calculations; green line: logaritmic binning without deformation effects. Here, for simplicity, the comparison is shown only for a single combination of pre-equilibrium and level density models.

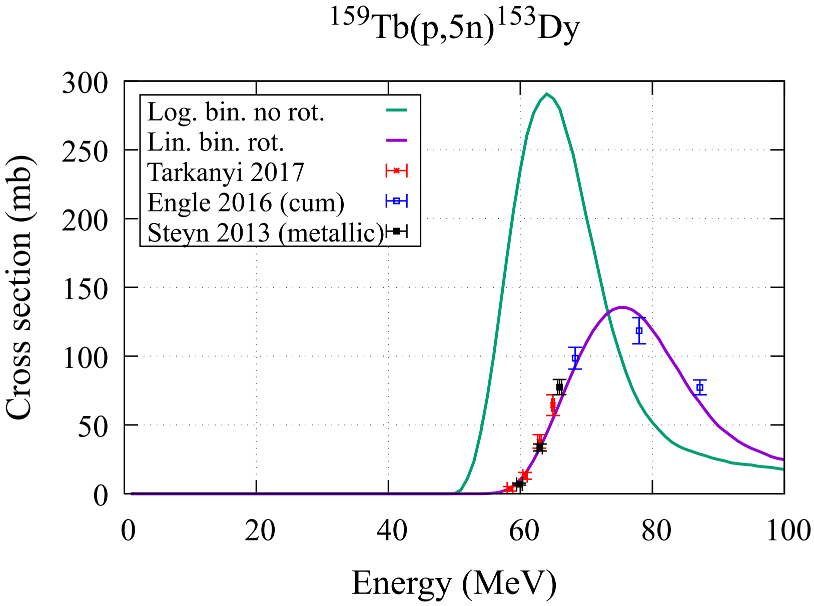

Figure 3.4: Effects of initial improvements for ^{153}Dy. Purple line: linear binning and coupled-channel calculations; green line: logaritmic binning without deformation effects. As in the previous figure, only a single combination of pre-equilibrium and level density models is considered.

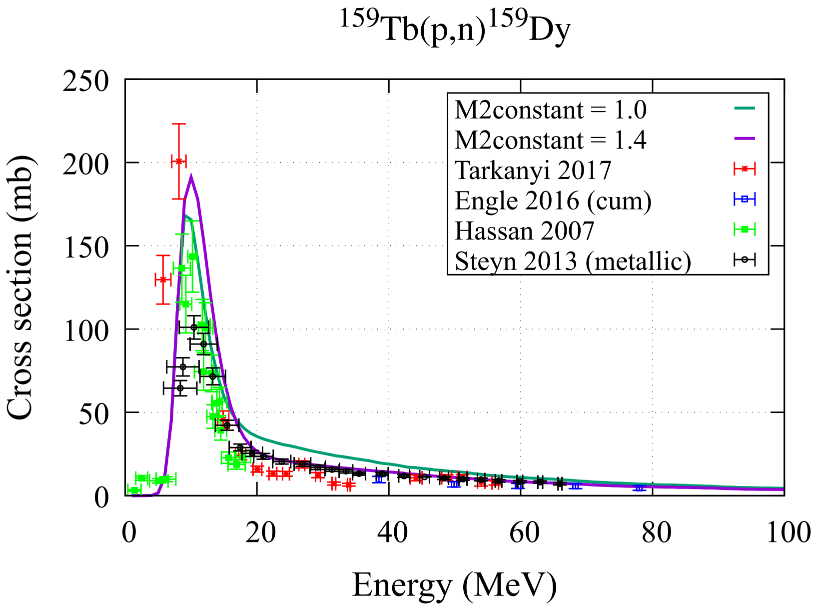

Figure 3.5: Comparison of the adjustment of the pre-equilibrium parameter `M2constant` to 1.4 (purple line) with respect to its default value (green line).

for the involved nuclides, a specific combination of pre-equilibrium and level density models has been selected and used in subsequent studies. Regarding the level density, which is an essential ingredient for the compound nucleus theory and for the description of the peaks of the cross sections, in general the microscopic models perform better than the phenomenological models. In particular, the most recent model (`ldmodel 6`) has been chosen for all the nuclides produced in the reaction because on average it describes better all the cross sections. Moreover, even if the microscopic level densities are developed considering the collective effects as stated in RIPL [100], in this work better results have been obtained forcing the code to consider the collective enhancement of the level density using `colenhance y`.

In addition to the level density, the strength function is an important quantity to model the gamma emissions in the de-excitation process of the compound nucleus. In this reaction, the same theoretical model of the level density has been used for this quantity, with `strength 8`.

On the other hand, among the pre-equilibrium models implemented in the special version of the code used in this work, the attention has been focused on the exciton model instead of the quantum mechanical model, which is not properly effective in this case, and of the Geometry Dependent Hybrid model since its parameters are not easily accessible. The third option for the exciton model (`preeqmode 3`) has been used varying its single parameter `M2constant` that has important effects on the cross sections. Indeed, it has been observed that an increase of `M2constant` results in a decrease of the cross section tail of ^{159}Dy and in an increase of the peak magnitude of the cross section of the other dysprosium nuclides. The parameter can be varied from 0 to 100, with 1 as the default value. In this study, the parameter has been modified and adjusted to `M2constant 1.4`, since with the default value the TALYS curve overestimates the experimental cross section of ^{159}Dy, as shown in Fig. 3.5. Therefore the adjustment corresponds to a very small variation from the default value and provides a significant result. In order to compensate for the increased peak of the other dysprosium nuclides further parameters have been considered for the pre-equilibrium process and in particular for the stripping reactions. The final result has been obtained using `Cstrip d 4.2` which affects the cross section of the (p, d) channel (for the production of ^{158}Tb) and produces effects also on other channels like (p, xn) for the production of dysprosium nuclides. This behaviour could be explained considering that for these direct-like reactions all the intermediate states are taken into account in the calculations. Indeed, deuterons could be formed in intermediate states during the formation and de-excitation processes of a specific nuclide. In these cases deuterons could also absorb energies higher than their binding energy ($\simeq$ 2.2 MeV) and therefore they could split into a neutron and a proton. The latter could have not enough energy to cross the Coulomb barrier and remains inside the nucleus while the neutron could escape. Additional pre-equilibrium model changes have also included the selection of the multiple exciton model (`mpreeqmode 1`), for the description of multiple pre-equilibrium reactions, the microscopic particle-hole state density (`phmodel 2`) and the default option for the pre-equilibrium spin distribution.

Finally, as described in the previous chapter, also the scaling transformation of the level density has been considered:

$$\rho(E, J, \pi) = \exp\left(c\sqrt{E-p}\right)\rho_{HFM}(E, J, \pi),$$

after the inspection of the cumulative of the levels of the dysprosium nuclides. The theoretical curve, calculated using the default level density parameters tabulated inside the code, is not in agreement with the experimental cumulative only for ^{153}Dy. Moreover only the cross section of ^{153}Dy required a minimal adjustment to reduce the effects of the variation of the pre-equilibrium parameters. Therefore, the values of the c, p parameters have been selected to improve the description both of the cumulative and of the cross section of ^{153}Dy and their optimal value are: $c = -0.4$ and $p = -0.6$.

In Fig. 3.6 the comparison of the experimental cumulative and the theoretical calculations is shown for all the four relevant dysprosium radionuclides. In particular for ^{153}Dy also the calculation with the default parameters is shown with a clear discrepancy with respect to the experimental cumulative and to the curve obtained with manual modification of the parameters.

All the parameter changes are listed in Tab. 3.1 and the TALYS calculations, produced with these new modifications, are plotted in the following figures and are referred to as "TALYS modified", in comparison with the TENDL–2021 curve. The latter is based on TALYS–1.96 calculations performed consid-

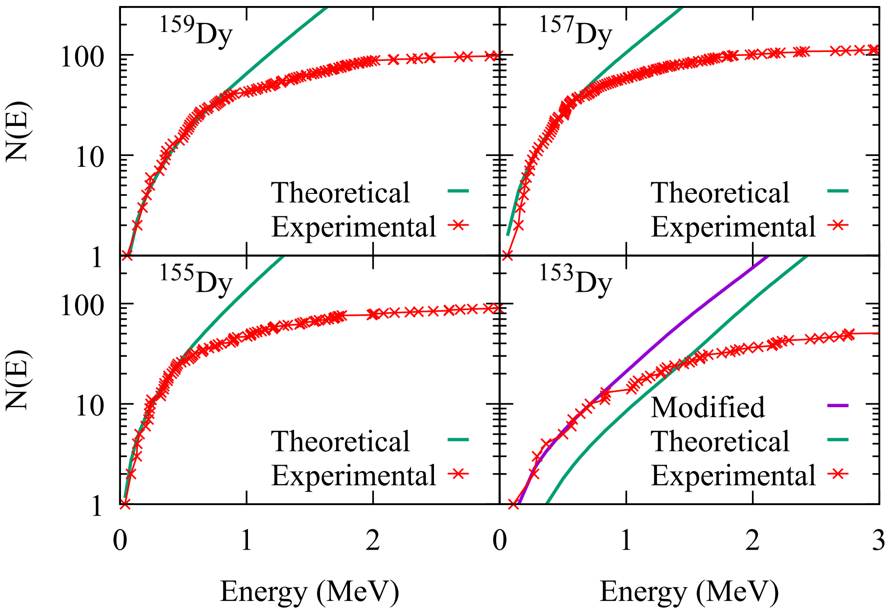

Figure 3.6: Theoretical and experimental cumulatives of levels for the four relevant dysprosium nuclides. The Theoretical curves (green lines) are obtained without any variation of the tabulated values of the level density c and p parameters. The TALYS modified curve (purple line), instead, is obtained with $c = -0.4$ and $p = -0.6$.

ering adjustments of different parameters for a global and general description of various reactions induced by the particles handled by the code.

The found solution is not intended to be unique: other combinations of pre-equilibrium and level density models adjustments as well as variations of the parameters of the Koning–Delaroche optical potential have been considered. However, among the different considered analyses, the described solution is the optimal one in terms both of the number of parameters and of the deviation from the default values.

The results in Figs. 3.7–3.10 are referred to the cross sections of the dysprosium nuclides. From these plots a better description of the cross section of the dysprosium nuclides is clearly evident: in particular for ^{153}Dy our approach accurately reproduces the measurements, while TENDL overestimates the experimental data. This will have an impact on the quality of ^{155}Tb produced with this route as it will be shown in the next chapter.

Parameter	Value
equidistant	y
bins	0
rotational	n p d a
autorot	y
preeqmode	3
M2constant	1.4
Cstrip	d 4.2
preeqspin	n
mpreeqmode	1
phmodel	2
ldmodel	6
colenhance	y
strength	8
ctable	66 153 –0.4
ptable	66 153 –0.6

Table 3.1: TALYS parameters adjustment used in this work to reproduce the experimental data of the ^{159}Tb(p, x) reaction.

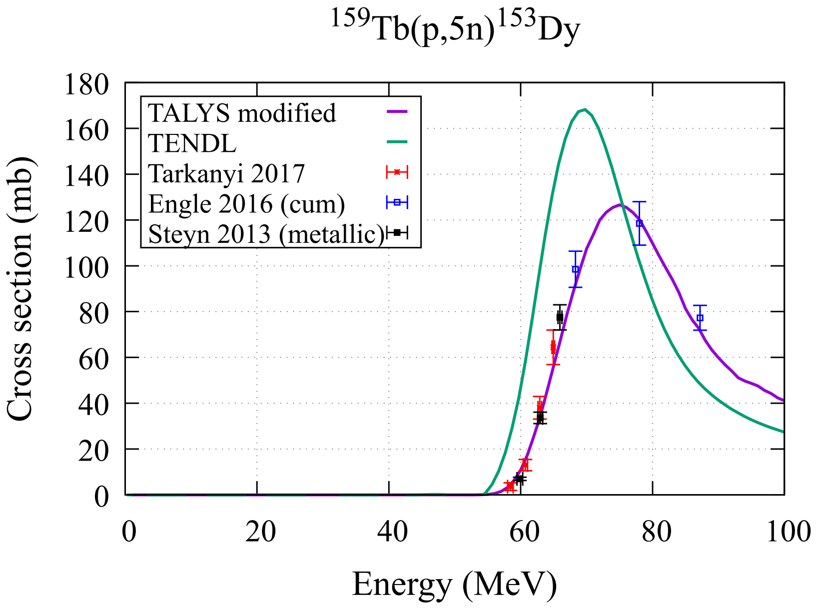

Figure 3.7: Comparison of TALYS modified and TENDL curves with experimental data for ^{153}Dy.

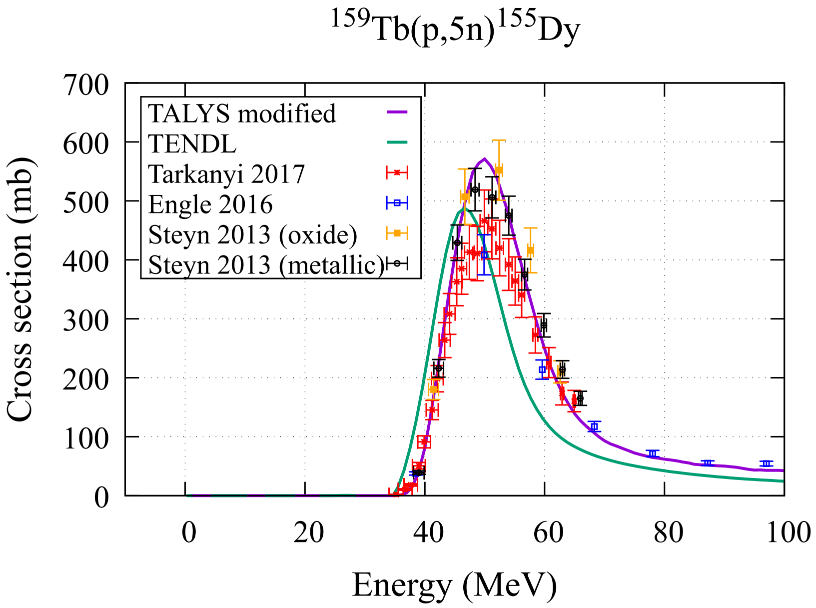

Figure 3.8: Comparison of TALYS modified and TENDL curves with experimental data for ^{155}Dy.

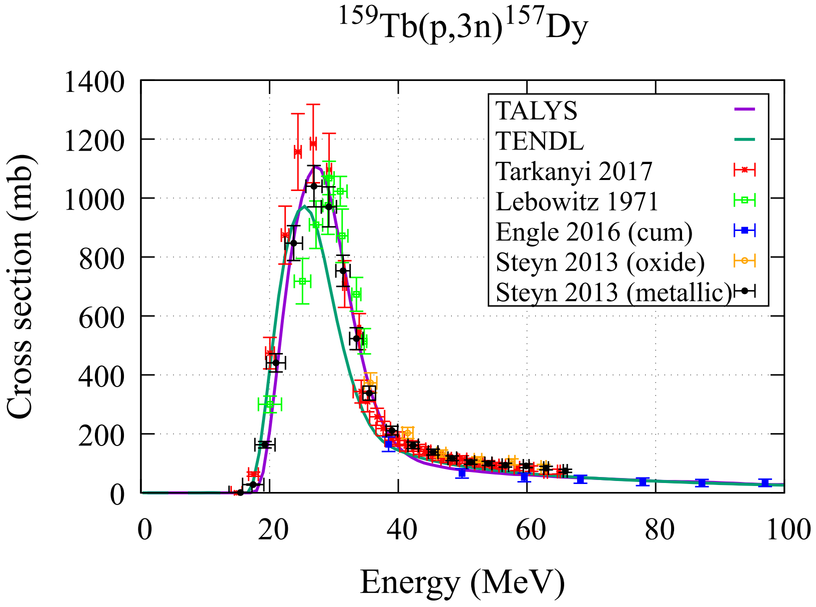

Figure 3.9: Comparison of TALYS modified and TENDL curves with experimental data for ^{157}Dy.

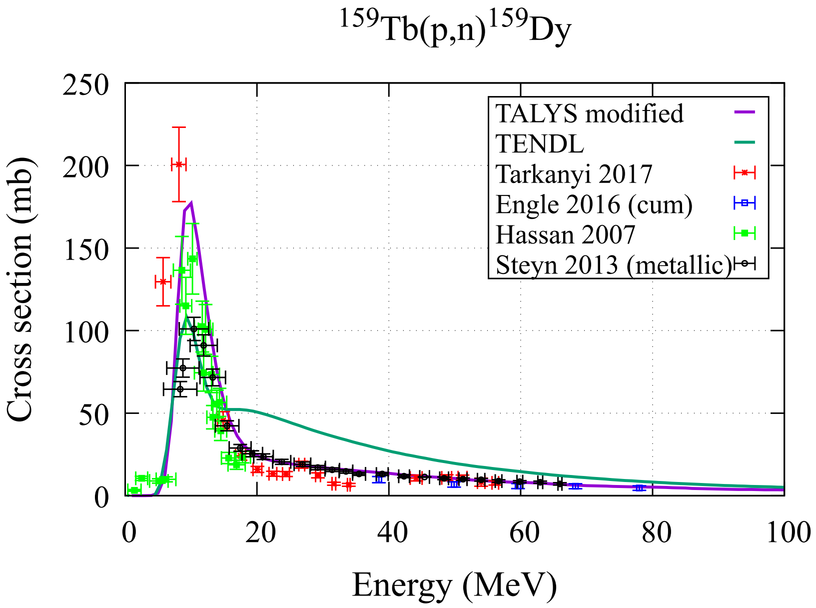

Figure 3.10: Comparison of TALYS modified and TENDL curves with experimental data for ^{159}Dy.

The used approach has created effects also on the cross sections of terbium and gadolinium nuclides, that have not been considered in the analysis. The optimal solution indeed has been found with regard only of the dysprosium nuclides that are the relevant ones in this study. However, for completeness, in Figs. 3.11–3.13 the comparison between TALYS modified, TENDL and the available data are shown for different terbium and gadolinium nuclides. In these figures the TALYS modified curve seems to better reproduce, on average, the trend of the cross sections, even if in some cases, like for ^{156}Tb, the new curve overestimates the cross sections. This behaviour is mainly due to the variation of the pre-equilibrium parameters that have a global effect on all the produced nuclides in the given reaction, like a higher prediction of the cross section tail for ^{155}Tb^{cum}. Probably, the inclusion of isospin (not yet implemented in the code) and the variation of many other parameters, including the level density parameters for several nuclides, could improve the description of the terbium and gadolinium nuclides, but, as stated, this was not the main goal of this work.

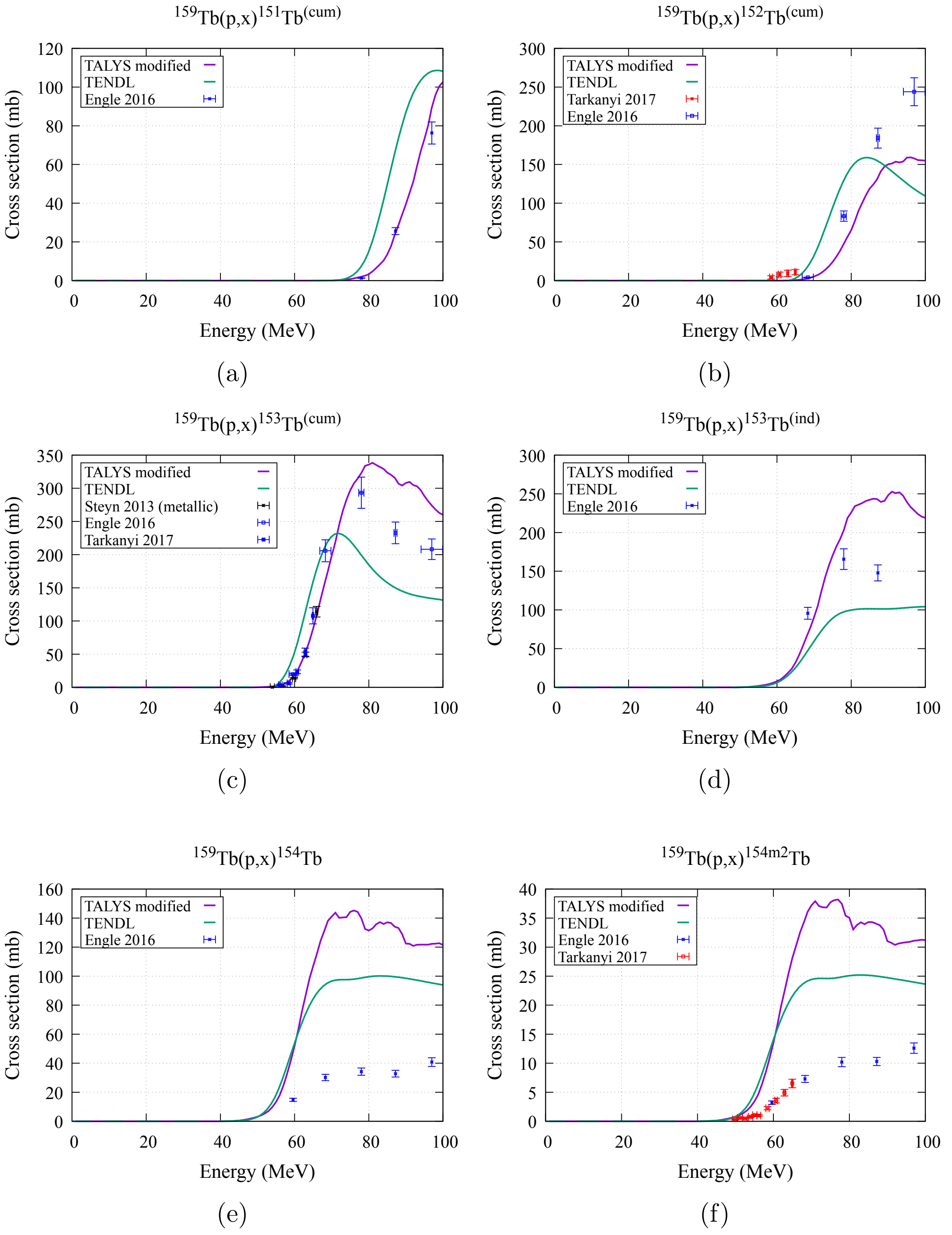

Figure 3.11: Comparison of TALYS modified and TENDL curves with experimental data for ^{151}Tb^{cum} (a), ^{152}Tb^{cum} (b), ^{153}Tb^{cum} (c), ^{153}Tb (d), ^{154}Tb (e) and ^{154m2}Tb (f).

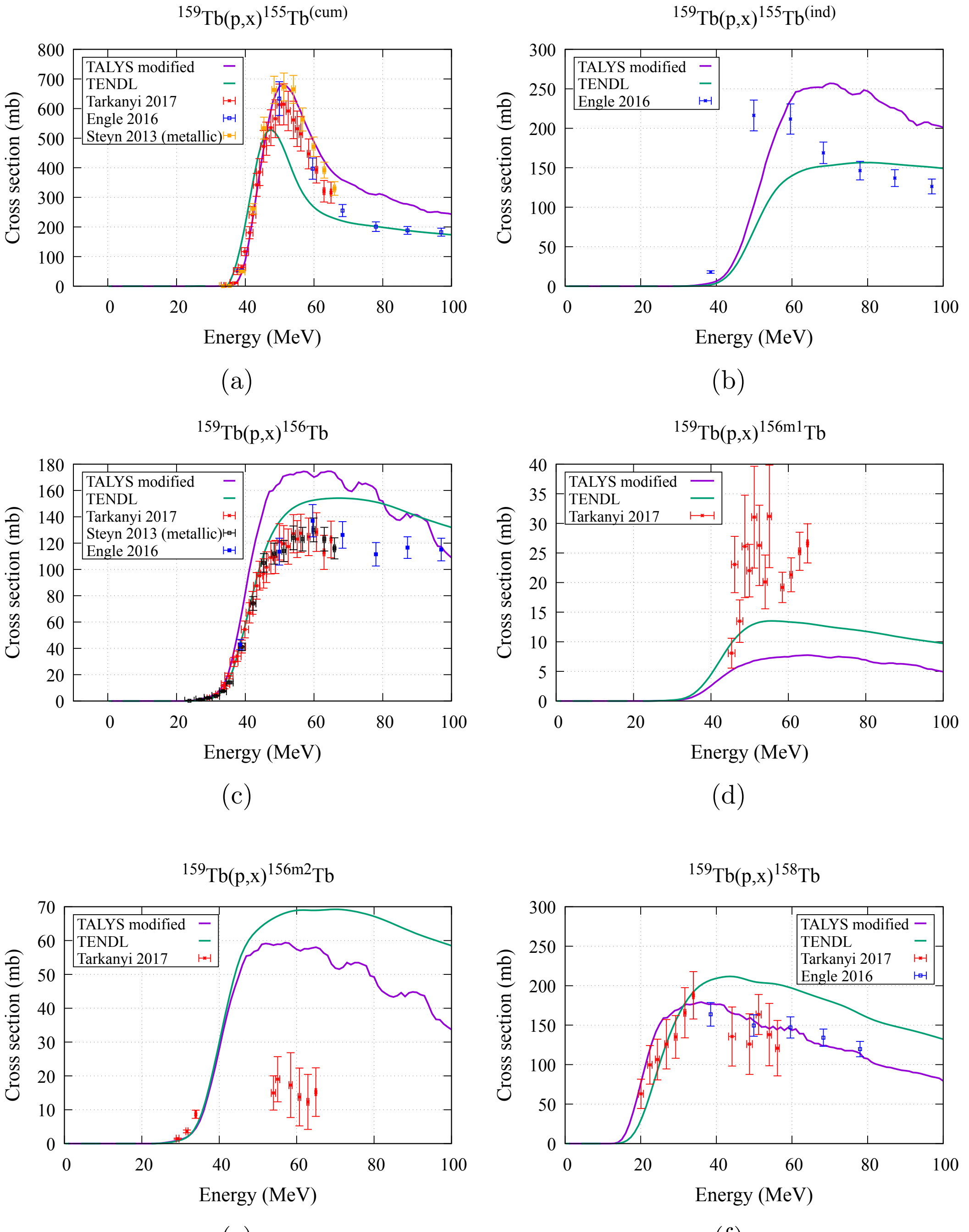

(a) (b)

(c) (d)

(e) (f)

Figure 3.12: Comparison of TALYS modified and TENDL curves with experimental data for ^{155}Tb^{cum} (a), ^{155}Tb^{ind} (b), ^{156}Tb (c), ^{156m1}Tb (d), ^{156m2}Tb (e) and ^{158}Tb (f).

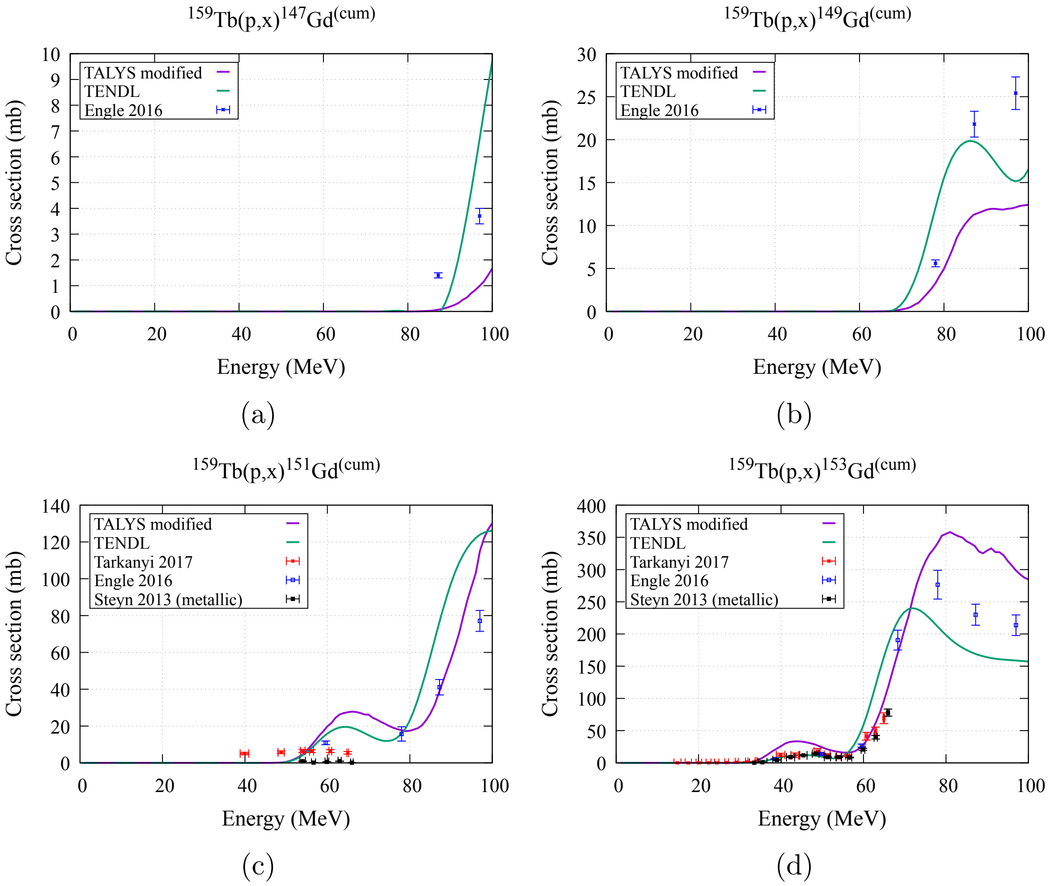

(a) (b) (c) (d)

Figure 3.13: Comparison of TALYS modified and TENDL curves with experimental data for ^{147}Gd^{cum} (a), ^{149}Gd^{cum} (b), ^{151}Gd^{cum} (c) and ^{153}Gd^{cum} (d).

Validation

In order to evaluate from a quantitative point of view the goodness of the results obtained with the found set of parameters, the same approach used in the literature to test new TALYS adjustment calculations has been considered and applied in this work.

In particular, as described in [83], based on the work of the authors of the code [120, 121], a total chi-square, χ^2_{tot}, is used to compare the TENDL and the "TALYS modified" curves for all the channels, *i.e.* considering all the produced radionuclides, using the following expression:

$$\chi^2_{tot} = \frac{1}{N_c} \sum_{c=1}^{N_c} \chi^2_c w_c \qquad (3.1)$$

where N_c is the number of all the reaction channels, χ^2_c is the chi-square value per channel and w_c is a weight that is used to normalize data belonging to different reaction channels. In the literature two methodologies are usually considered in order to stress the importance of the calculations to the most prominent channels:

- "Cumulative σ" weighting, that acts as an area normalization. Its expression is:
$$w_c = \frac{\sum_{i=1}^{N_P} \sigma_T^{c,i}}{\sum_{c=1}^{N_c} \sum_{i=1}^{N_P} \sigma_T^{c,i}} \tag{3.2}$$
where $\sigma_T^{c,i}$ is the TALYS cross section evaluated at the energy of the point i for each channel c, while N_P is the number of data points of all the experimental datasets per channel.

- "Maximum σ" weighting, that is the fraction between the TALYS maximum cross section reached in each channel and the sum of the TALYS maxima of all the channels. The expression is:
$$w_c = \frac{\sigma_{T,max}^{c}}{\sum_{c=1}^{N_c} \sigma_{T,max}^{c}}. \tag{3.3}$$

The latter is suggested to strengthen the significant parameter adjustments, if any, for the reproduction of large compound peaks at low energies. However, in this work the compound peaks have not been predominant in the analysis of the cross sections of the relevant nuclides and, therefore, the "Cumulative σ" weighting has been used.

For each channel, χ_c^2 is calculated without exclusion of any data and is given by:

$$\chi_c^2 = \frac{1}{N_P} \sum_{i=1}^{N_P} \left(\frac{\sigma_{Exp}^i - \sigma_T^i}{\Delta\sigma_{Exp}^i} \right)^2 \tag{3.4}$$

where σ_{Exp}^i are the experimental cross sections and $\Delta\sigma_{Exp}^i$ their uncertainties, while σ_T^i are the TALYS cross section calculations. In particular, for an accurate determination of χ_c^2, both the uncertainty on the cross section and on the energy (if available) have been considered by combining them in quadrature as described in Ref. [122]:

$$\Delta\sigma^2 = \left(\Delta\sigma_x \frac{dy}{dx} \right)^2 + (\Delta\sigma_y)^2 \tag{3.5}$$

where $\Delta\sigma_x \frac{dy}{dx}$ is the indirect contribution from the uncertainty in x (*i.e.* in energy) to the total uncertainty in y (*i.e.* in cross section) using a first-order approximation.

In Tab. 3.2 the comparison of the total chi-square confirms that "TALYS modified", produced by realistic analysis driven by numerical and physical considerations, gives a better global description of the cross sections with respect

TALYS modified χ^2_{tot}	TENDL χ^2_{tot}
1.7	3.6

Table 3.2: Total chi-square describing the goodness of the TALYS modified and TENDL curve for the ^{159}Tb(p, x) reaction. An improvement of ∼53% has been achieved.

to the standard TENDL curve: an improvement of ∼53% is achieved. This result is notable considering that the model optimization has been obtained for only the dysprosium nuclides, varying few parameters, and is certainly a more reliable and general approach with respect to the mere interpolation of experimental data.

3.2 Reactions with deuterons

The same procedure described in the previous section has been applied also for the reaction with deuterons.

As presented in the first chapter, for this reaction few experimental data are available only for seven reaction channels for the production of: ^{155}Dy, ^{157}Dy, ^{159}Dy, ^{155}Tb^{cum}, ^{156}Tb, ^{160}Tb and ^{153}Gd. Moreover, for some nuclides, the data are very scattered and thus not in agreement with each other. Therefore the analysis of the cross sections has been more difficult: anyway the study has led to an improvement in the description of the cross sections for the produced nuclides.

The first step in the analysis of the cross sections has been represented by the investigation of the behaviour of the five models of the optical potential for deuterons implemented in the TALYS code. In Fig. 3.14, the comparison of these models is shown for the case of ^{155}Dy, keeping the default options for all the other parameters. From the figure, the curve obtained with the default option, `deuteronomp 1`, fails in the description of the cross section while all the others are close one each other. Among the models, `deuteronomp 4` and `deuteromomp 5` are the most recent ones. Since the former seems to overestimate less the cross section, not only for ^{155}Dy but also for the other nuclides, it has been chosen for the description of the reaction. In particular, `deuteronomp 4` corresponds to the model of Han et al. [75], which has been obtained in a similar way to the well-known Koning–Delaroche potential. Indeed it results from a global fit of the potential parameters for reactions induced by deuterons, with energy from threshold to 200 MeV, on nuclei within the mass number range $12 \leq A \leq 209$, and considering the experimental data of deuteron total reaction cross sections and elastic scattering angular distributions.

Similarly to the case of the reaction with protons, a comparative study between the logaritmic (default) and liner binning has been considered, and better results have been obtained with the linear binning using the same en-

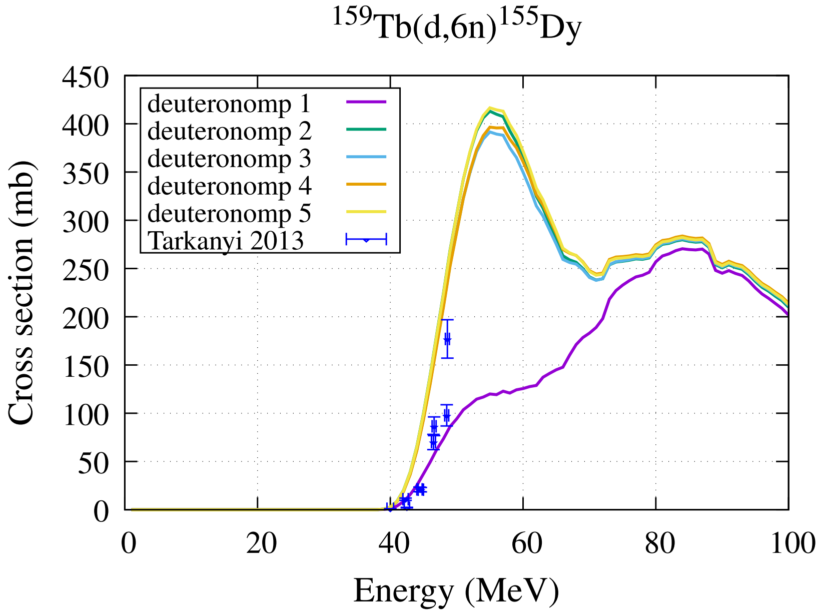

Figure 3.14: Comparison of the five deuteron optical potential models implemented inside the TALYS code for ^{155}Dy.

ergy dependent algorithm presented before (`bins 0`). Moreover the options `rotational n p d a` and `autorot y` have been used also for this reaction for the automatic coupled-channels calculations, since the reaction involves the same deformed nuclides of the previous case. These choices have the same effects described for the reaction with protons: a slight shift to the right of the curves.

Regarding the pre-equilibrium models, the default option (`preeqmode 2`) has been selected without any variation of the parameters of the matrix element (*i.e.* `M2constant`, `M2limit` and `M2shift`). Other parameters, like `mpreeqmode`, `preeqsin`, `phmodel`, . . . for example, have been considered but no apparent change has been observed. However, since this reaction is induced by deuterons, the break-up process has been examined with particular attention. As described in the previous chapter, two models are available inside the TALYS code: the Kalbach phenomenological model (which is the default option) and the microscopic Avrigeanu model. Both models have been considered using the `breakupmodel` keyword and their comparison is shown in Fig. 3.15. In this context the default option clearly describes better the trend of the data, while the other model may require some adjustments from the theoretical point of view, which can be done by the authors of the model: there is no way for a TALYS user to improve it. Nevertheless, for some nuclides, like ^{159}Dy and ^{160}Tb that correspond to the (d, n) and (d, p) channels respectively, an attempt has been performed to improve the description of their cross section, adjusting the break-up parameter with the `Cbreak n` and `Cbreak p` keywords. In this context, the attention has been focused not only on dysprosium nuclides but

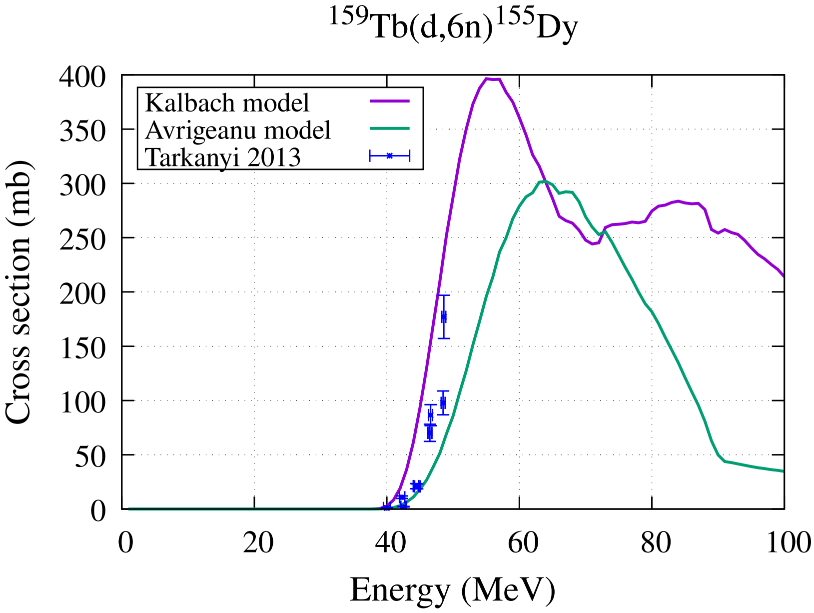

Figure 3.15: Comparison of the two deuteron break-up models available inside the code.

also on ^{160}Tb, because the break-up process involves both the (d, n) and (d, p) channels and they result strictly correlated. In particular the change from the unity (default value) of this parameter and its adjustment to `Cbreak n 0.53` and `Cbreak p 1.25` have been made to reduce the cross section of ^{159}Dy while increasing the one of ^{160}Tb.

Concerning the level density, the `ldmodel 6` has been given the best agreement with data almost for all the produced nuclides. The TALYS code allows to choose a specific level density model per nuclide allowing to tailor the models to individual reaction channels: this possibility has been investigated by mixing parametrization among different nuclides. Among the various combinations, the choice to use `ldmodel 5` only for ^{157}Dy and ^{159}Dy while keeping `ldmodel 6` for all the other nuclides has produced the best results. This change has allowed to soften the high-energy tail of these two dysprosium radionuclides, whithout any visible effect to the other reaction channels. Finally, another consideration has been made for the level density, regarding the c and p parameters. Looking to the cumulative of the four relevant dysprosium nuclides, a good agreement has been observed for ^{155}Dy, ^{157}Dy and ^{159}Dy between the theoretical curve and the experimental cumulative. For the case of ^{153}Dy the same picture of the reaction with protons has been faced: a discrepancy in the description of the cumulative of the levels from theoretical point of view. But in this context experimental data are not available for the cross section of ^{153}Dy. Therefore the effects of a variation of the level density parameters could not be assessed by looking at the cross section. However, the same parameters found for the protons reaction have been used also here, motivated by the following considerations:

1. the level density is a property of every nuclide and is independent of the particular reaction from which is produced.
2. TALYS provides, per each nuclide, tables containing values of the *c*, *p* parameters that depends on the specific considered microscopic model. They are used by default and therefore their values are always the same for every reaction.
3. In the reaction with protons, `ldmodel 6` has been optimized for ^{153}Dy and new values of the two parameters have been found. Consequently, these new values could be used whenever considering `ldmodel 6` for the production of ^{153}Dy, as in the study of the reaction induced by deuterons.

Needless to say, the picture is complex and this consideration is not to be intended as absolute. Indeed, looking to the nuclide chart, for many nuclides the theoretical predictions of the cumulative are usually not in agreement with the observed levels, even if the default values of the parameters are obtained after a renormalization of the microscopic models to experimental data for thousands of nuclei (see Fig. 3.16 that shows the comparison between the theoretical and experimental cumulatives presented in RIPL Ref. [100]).

Parameter	Value
equidistant	y
bins	0
deuteronomp	4
rotational	n p d a
autorot	y
Cbreak	n 0.53
Cbreak	d 1.25
ldmodel	6
ldmodel	5 66 159
ldmodel	5 66 157
ctable	66 153 –0.4
ptable	66 153 –0.6

Table 3.3: TALYS parameters adjustment used in this work to reproduce the experimental data of the ^{159}Tb(d, x) reaction.

In Fig. 3.17 the comparison of the theoretical predictions calculated in this work, and the experimental observed levels is shown for the four relevant dysprosium nuclides, while in Tab. 3.3 all the parameters used in this reaction are summarized.

In Figs. 3.18–3.20 the comparison of the TALYS modified and TENDL curves is shown for the dysprosium nuclides while in 3.21 the one for terbium

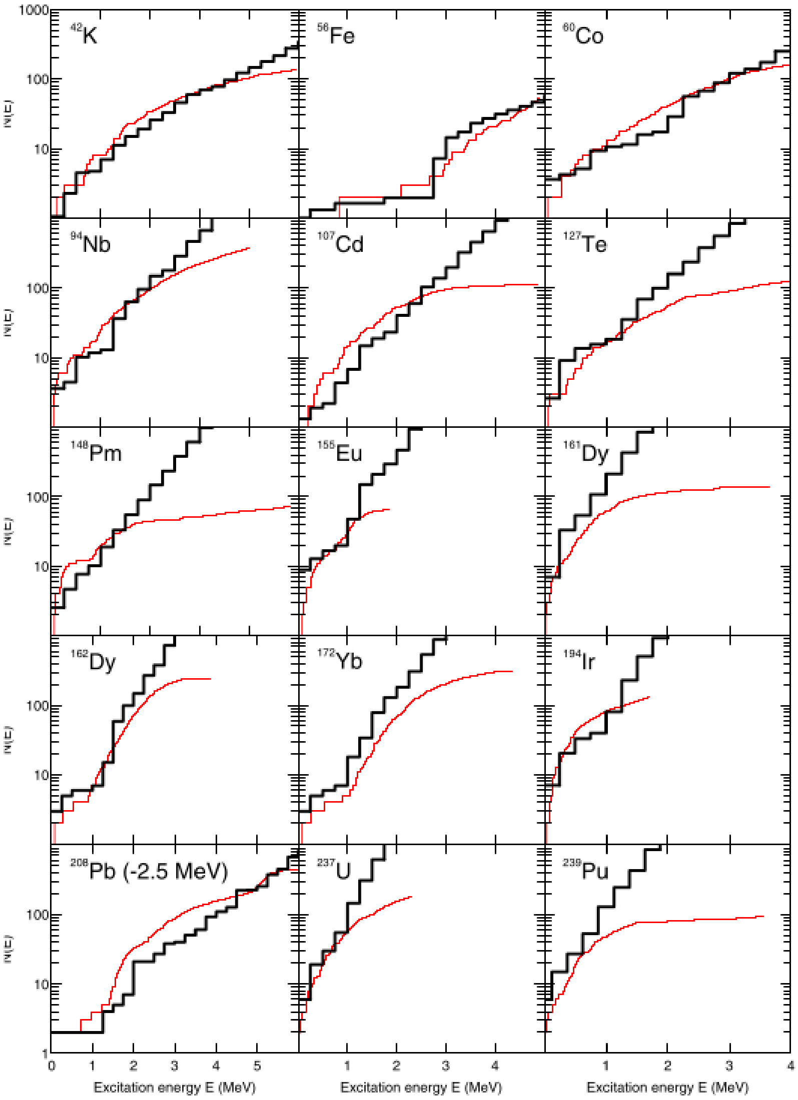

Figure 3.16: comparison between the theoretical (black lines) and experimental (red lines) cumulatives presented in RIPL, Ref. [100] on page 3163. In many cases, the tabulated values of the c and p parameters do not allow a proper description of the number of observed levels.

and gadolinium nuclides. Also for this reaction an average better description of the cross section has been obtained. Unfortunately, the TALYS modified curve does not reproduce well the cross section of ^{159}Dy and of ^{160}Tb. The main problem is given by the very scattered data, but it is challenging to predict accurately and simultaneously both the (d, n) and (d, p) channels and to obey at the same time the spectra fits of Kalbach. Therefore, more work is probably needed both from the theoretical and the experimental points of view to improve the agreement for these specific channels [56].

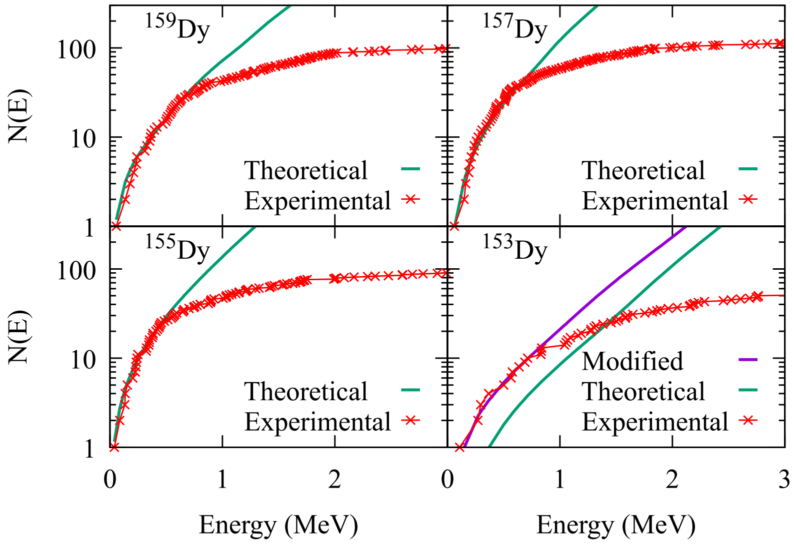

Figure 3.17: Comparison between the theoretical predictions and the experimental observed levels for the four relevant dysprosium nuclides. For ^{157}Dy and ^{159}Dy `ldmodel 5` has been used, while `ldmodel 6` for all the other nuclides. The TALYS modified prediction is the same of the reaction induced by protons.

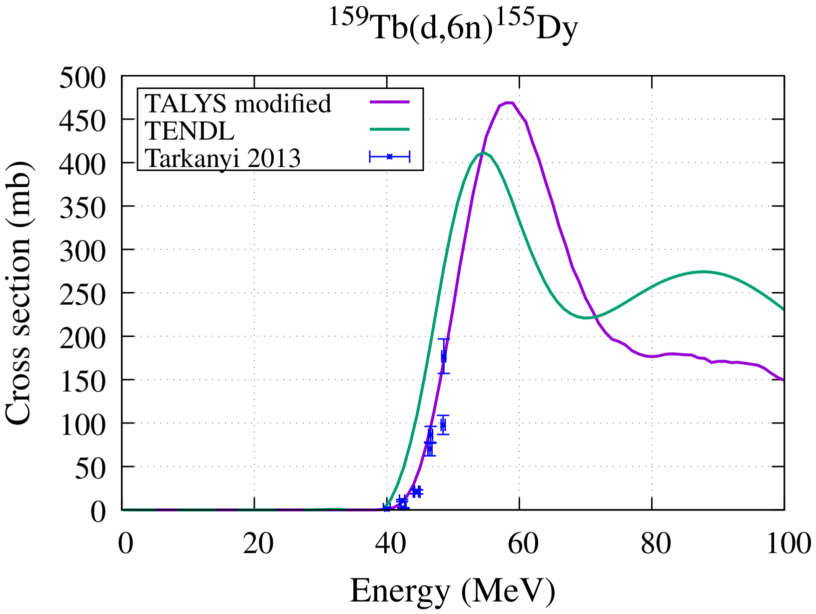

Figure 3.18: Comparison of TALYS modified and TENDL cross section curves with experimental data for ^{155}Dy.

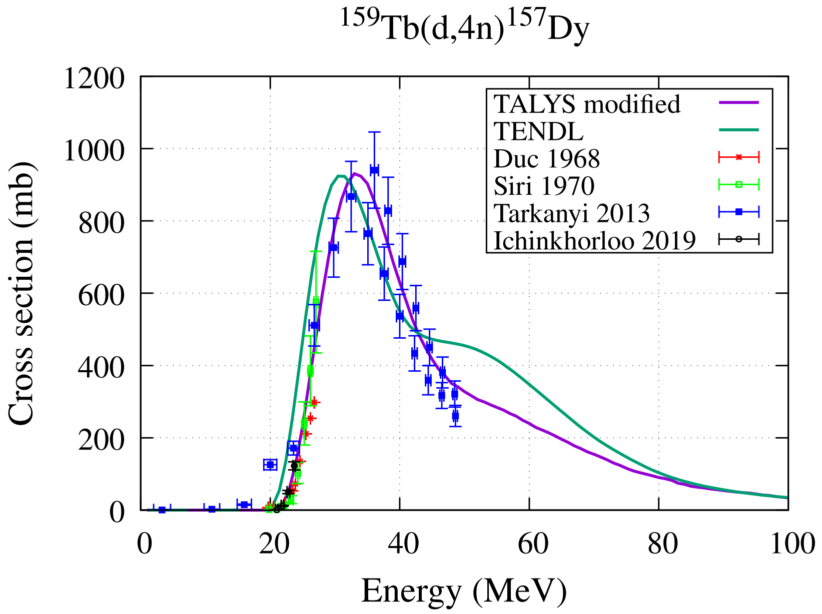

Figure 3.19: Comparison of TALYS modified and TENDL cross section curves with experimental data for ^{157}Dy.

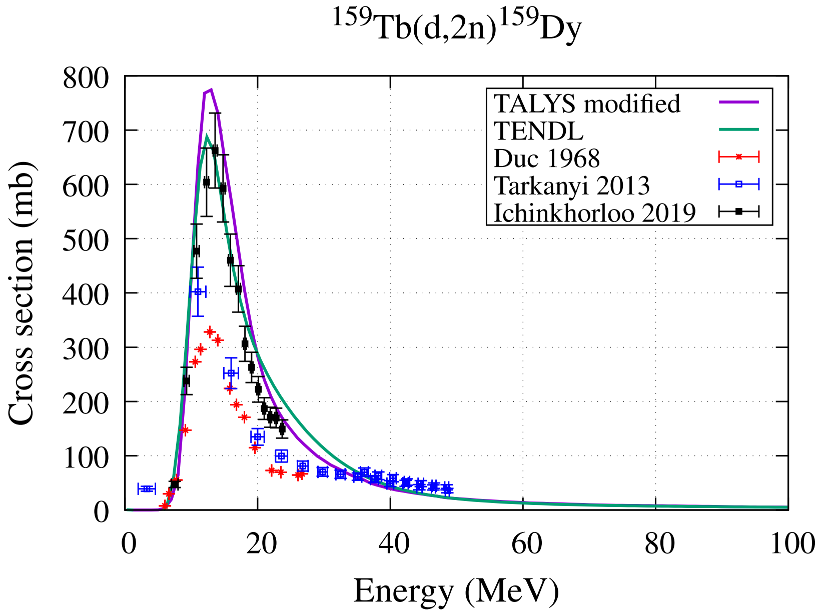

Figure 3.20: Comparison of TALYS modified and TENDL cross section curves with experimental data for ^{159}Dy.

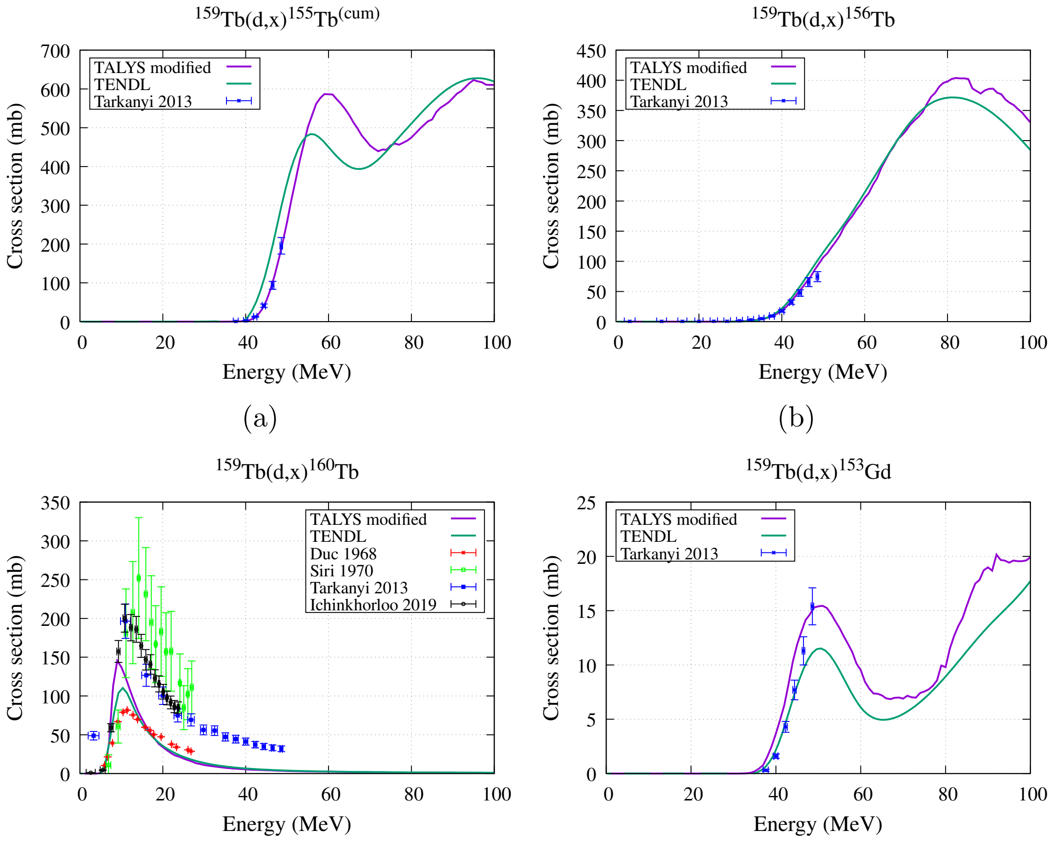

(a) (b)

(c) (d)

Figure 3.21: Comparison of TALYS modified and TENDL cross section curves with experimental data for ^{155}Tb^{cum} (a), ^{156}Tb (b), ^{160}Tb (c) and ^{153}Gd (d).

Validation

TALYS modified and TENDL calculations are compared by means of the total chi-square metrics, described in the previous section. For this reaction the old data of Duc et al. have not been considered in the calculation of χ^2_{tot} to avoid infinities, since they are given without cross section uncertainties. In the following table the values of χ^2_{tot} show that with the few performed adjustments an improvement of ~38% has been obtained. In this case, however, the TENDL curves described already quite well the cross sections given the few available experimental data.

TALYS modified χ^2_{tot}	TENDL χ^2_{tot}
1.3	2.1

Table 3.4: Total chi-square for the ^{159}Tb(d, x) reaction. An improvement of ~38% has been achieved.

^{152}Gd	^{154}Gd	^{155}Gd	^{156}Gd	^{157}Gd	^{158}Gd	^{160}Gd
0.002	0.0218	0.1418	0.2047	0.1565	0.2484	0.2186

Table 3.5: Isotopic composition of ^{nat}Gd

3.3 Reactions with α particles

This reaction differs from the previous ones not only for the incident particle, but also for the considered target, ^{nat}Gd, which is not monoisotopic but has a broader composition. As presented in Tab. 3.5, in a natural gadolinium target there are seven gadolinium isotopes that can contribute to the formation of the same nuclides. Indeed, in the TALYS code each of the following reactions is considered and calculated individually: ^{152}Gd(α, x), ^{154}Gd(α, x), ^{155}Gd(α, x), ^{156}Gd(α, x), ^{157}Gd(α, x), ^{158}Gd(α, x) and ^{160}Gd(α, x). Only after the calculations, a weighted sum is performed, using the weights of Tab. 3.5, to derive the cross section of each nuclide produced by the ^{nat}Gd(α, x) reaction. In this way, one has also the possibility to consider separately the contribution of each gadolinium isotope. This may be useful if one is interested in the exam of the production of a specific radionuclide starting from an enriched target.

The same procedure described in the previous sections has been used to obtain a better description of the cross sections for different reaction channels where experimental data are available. With respect to the previous reactions, another important terbium radionuclide can be produced, namely ^{161}Tb. Therefore, the attention has been focused on the relevant dysprosium nuclides (for the indirect production of ^{155}Tb), and also on ^{161}Tb and on its main contaminant ^{160}Tb. The production of ^{161}Tb is not the goal of this thesis, anyway an attempt has been performed to obtain an accurate description also of its cross section. Indeed, studies on its direct production by means of ^{nat}Gd(α, x) have not been performed yet and only other direct reaction by means of protons and deuterons have been considered [123].

For the improvement of the cross sections, the linear binning with the default values of bins (`bins 40` equal for all the energies) has been used in addition to the automatic coupled-channels calculations (activated again with `rotational n p d a` and `autorot y`), since we are still considering the same nuclides of the previous reactions.

For the optical potential, the default option has been considered and used. It corresponds to the most recent Avrigeanu model [77] that performs better than the other available models. In particular it represents an improvement of the previous optical potential [79] for α particles on nuclei with mass number in the range from 45 to 209. The two main enhancements were the increase of the surface imaginary-potential depth and the ∼7% increase in value of the radius for the surface imaginary part of this potential. The latter modification has allowed to remove the underestimation of the cross section for well-deformed nuclei. Moreover it has been used in accurate analyses to remove also the significant underestimation of the α-particle emission obtained with the previous model.

Regarding the pre-equilibrium, the default exciton model with transition rates calculated numerically (`preeqmode 2`) has been used, but the parameters of the matrix element M^2 have been varied. In particular the best results have been obtained with `M2constant 0.9` and `M2shift 1.4`. This change had the effect to decrease the cross section of ^{160}Tb, adjusting it to recent data. Moreover also the stripping process with tritium as outgoing particle (`Cstrip t 2.0`) have been considered, especially to increase the cross section of ^{161}Tb while keeping almost unchanged all the other reaction channels. Also `Cknock a 0` has been used to remove a little "unphysical" hump around 25 MeV observed in different channels and not reproduced by the experimental data. The reset of this parameter of course decreases the cross sections of ^{nat}Gd(α, α x) reactions like ^{nat}Gd(α, α x)^{159}Gd. However, as it will be shown in the next plots, even TENDL performs very poorly showing an odd behaviour. An attempt to include also this channel in the current analysis has been made with scarce results: any adjustment of the parameters has produced drastic effects on the more important channels for this study. Therefore the found values of the parameter has been kept optimal, since the aim of this thesis is the indirect production of ^{155}Tb.

Finally, considerations on the level density have been made similarly to the case of deuterons. For almost all the nuclides `ldmodel 5` has been used forcing the collective enhancement of the level density, while for ^{153}Dy, ^{155}Dy, ^{153}Tb, ^{155}Tb, ^{156}Tb, ^{160}Tb and ^{161}Tb `ldmodel 6` has been chosen. Moreover, with the same assumption explained in the reaction with deuterons, $c = -0.4$ and $p = -0.6$ have been used also here for ^{153}Dy, even if experimental data are not available for this channel. However, for this reaction the cumulative cross section of ^{153}Tb is available, that is the sum of ^{153}Tb and ^{153}Dy (the progenitor) cross sections. Therefore the variation of the level density parameters of ^{153}Dy have produced visible and positive effects in the cumulative cross section of ^{153}Tb, confirming the choice made for the use of the new found level density parameters. Nevertheless, also the p parameter of ^{161}Tb has been varied for a slight improvement in the description of its cross section without an excessive large modification of the cumulative theoretical prediction, as shown in Fig. 3.22.

The set of the adjusted parameter used in the analysis of this reaction is summarized in Tab. 3.6, while in Figs. 3.23–3.28 the comparison of the TALYS modified and TENDL curves with the available experimental data is shown. Again there are few experimental data sets and they are not in great agreement with each other for many channels. In particular the point of Moiseeva et al. around 55 MeV is odd due to the very large uncertainty, as reported also in their paper (Ref. [50]) and the old data by Gayoso et al. seem to describe very differently the cross section if compared with the new data by Ichinkhorloo et al., especially for ^{161}Tb.

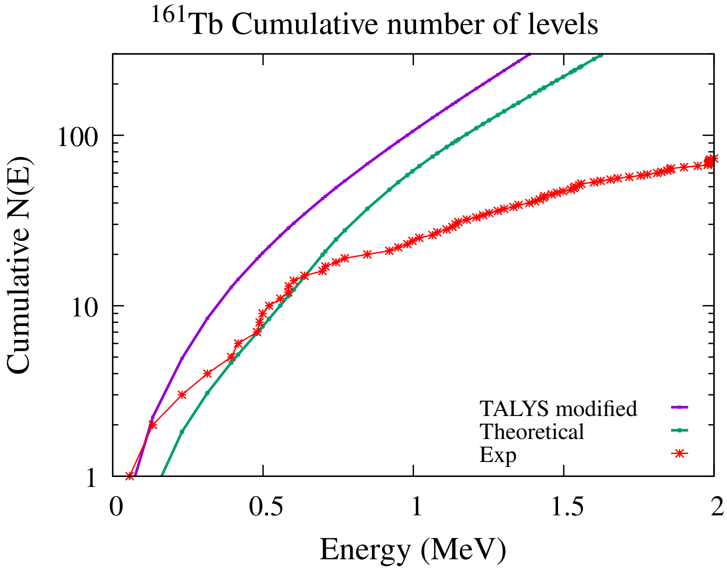

Figure 3.22: Comparison of the experimental and theoretical cumulatives for ^{161}Tb. In this work an improvement has been obtained with $p = -0.2$ (purple line) with respect to default values (green line).

Parameter	Value	Parameter	Value
equidistant	y	ldmodel	6 66 153
rotational	n p d a	ldmodel	6 66 155
autorot	y	ldmodel	6 65 153
M2constant	0.9	ldmodel	6 65 155
M2shift	1.4	ldmodel	6 65 156
Cstrip	t 2.0	ldmodel	6 65 160
Cknock	a 0	ldmodel	6 65 161
ldmodel	5	ctable	66 153 –0.4
colenhance	y	ptable	66 153 –0.6
		ptable	65 161 –0.2

Table 3.6: TALYS parameters adjustment used in this work to reproduce the experimental data of the ^{nat}Gd(α, x) reaction.

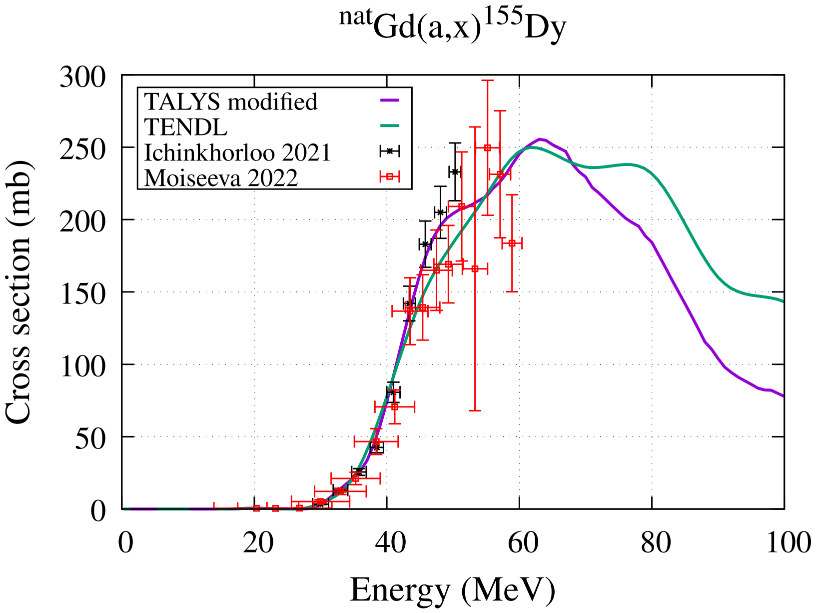

Figure 3.23: Comparison of TALYS modified and TENDL cross section curves with experimental data for ^{155}Dy.

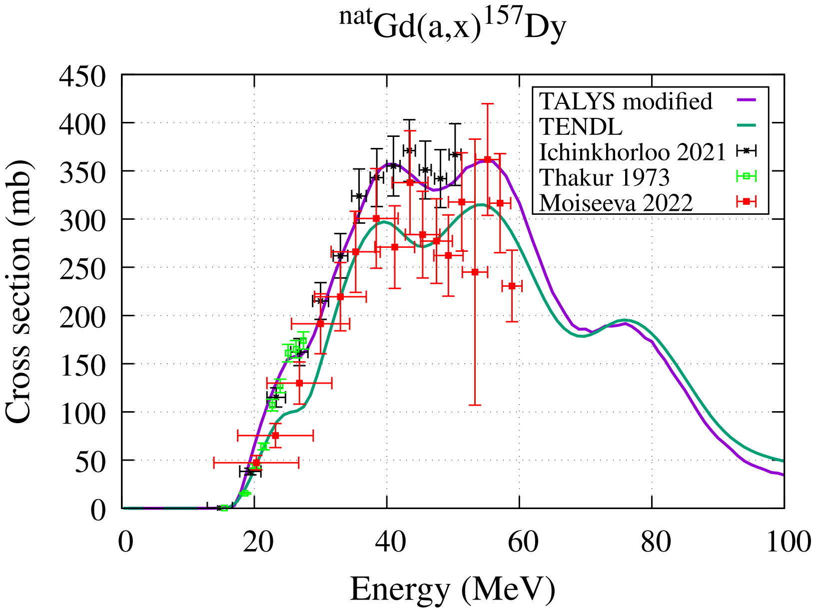

Figure 3.24: Comparison of TALYS modified and TENDL cross section curves with experimental data for ^{157}Dy.

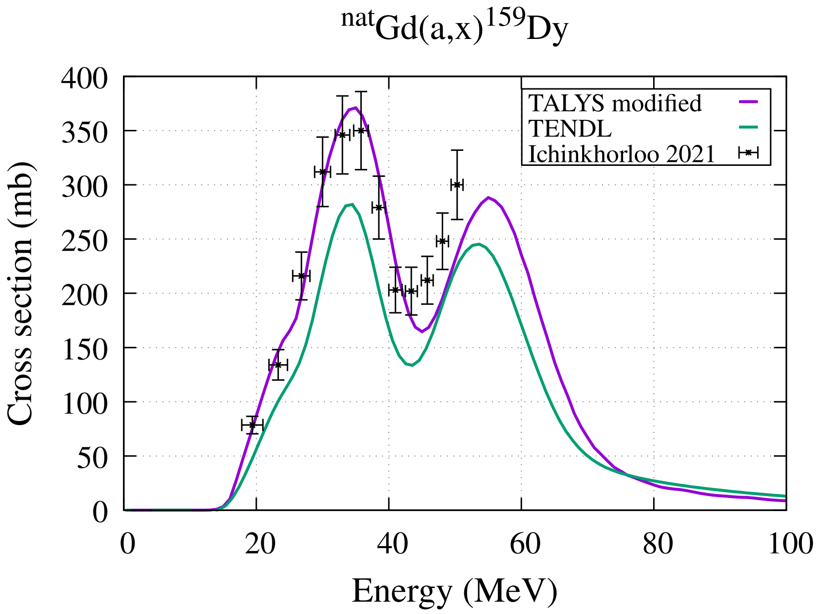

Figure 3.25: Comparison of TALYS modified and TENDL cross section curves with experimental data for ^{159}Dy.

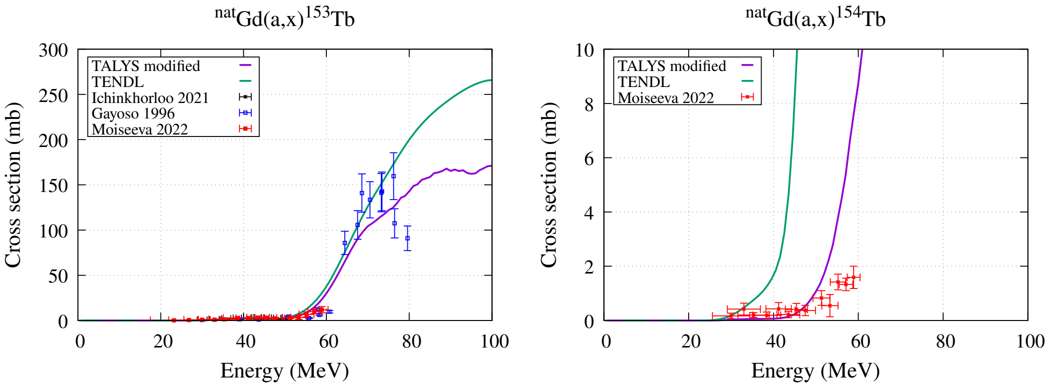

(a)

(b)

Figure 3.26: Comparison of TALYS modified and TENDL cross section curves with experimental data for ^{153}Tb (a), ^{154}Tb (b).

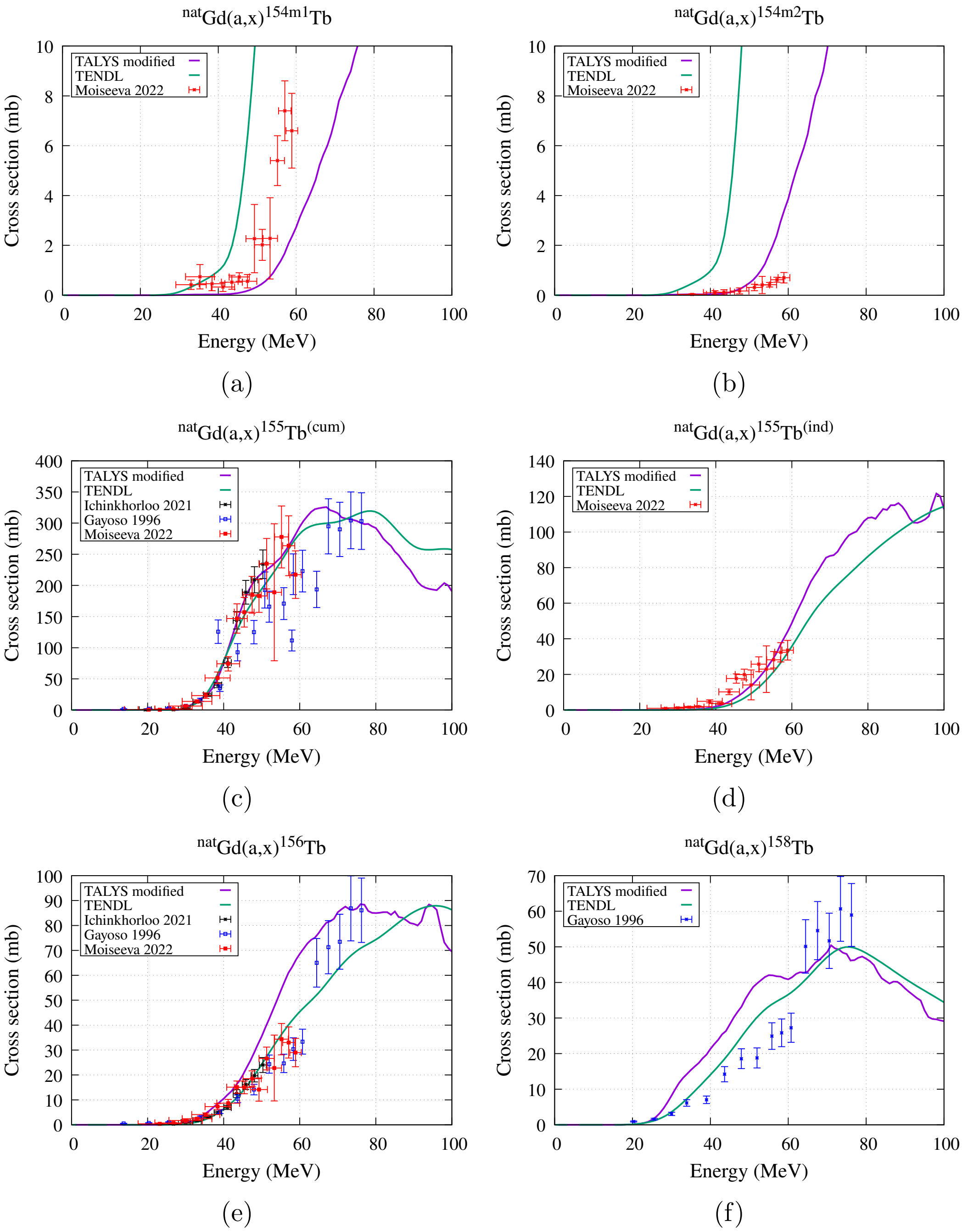

Figure 3.27: Comparison of TALYS modified and TENDL cross section curves with experimental data for ^{154m1}Tb (a), ^{154m2}Tb (b), ^{155}Tb^{cum} (c), ^{155}Tb^{ind} (d), ^{156}Tb (e) and ^{158}Tb (f).

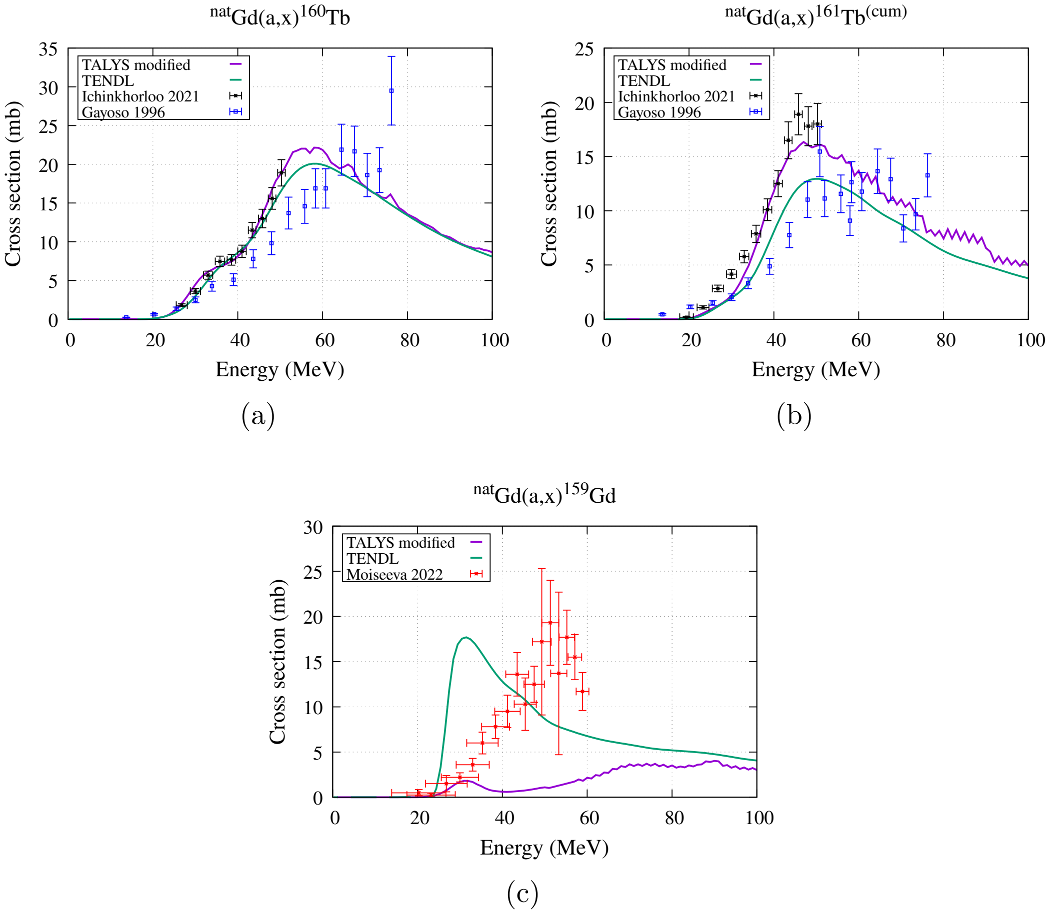

(a) (b)

(c)

Figure 3.28: Comparison of TALYS modified and TENDL cross section curves with experimental data for ^{156}Tb (a), ^{158}Tb (b), ^{160}Tb (c), ^{155}Tb^{cum} (d) and ^{159}Gd (e).

Validation

The total chi-square has been calculated also for this reaction considering all the data and the values for TALYS modified and TENDL are reported in Tab. 3.7. The χ^2_{tot} values are below the unity because of the large cross section uncertainties of the data by Moiseeva et al. and also Gayoso et al., but also in this case an improvement has been achieved. It is around 22%, therefore is slightly lower than the ones obtained with the reaction with protons and deuterons. Indeed, in this reaction, the TENDL curve seems to globally describe well the trend of the experimental data, even if for some nuclides, like for ^{157}Dy and ^{159}Dy, it underestimates the cross section while TALYS modified performs better. Anyway new experimental measurements are demanded to describe in more accurate way the cross sections of the different produced nuclides. Indeed new experimental measurements may help theoreticians to constraint the parameters of their models and a more extensive study may

TALYS modified χ^2_{tot}	TENDL χ^2_{tot}
0.9	0.7

Table 3.7: Total chi-square for the ^{nat}Gd(α, x) reaction. An improvement of $\sim$22% has been achieved.

lead to new solutions.

For the moment, the calculations of this study represent an improvement, especially for the dysprosium nuclides, for all the three considered reactions in view of the indirect production of ^{155}Tb. The analysis has been performed to avoid erroneous physical description of the reactions and limiting as much as possible the underestimation/overestimation of the cross sections. The current calculations, referred to as "TALYS modified", have allowed to obtain curves that represent the starting point to compute the different and useful quantities (activities and purities).

Chapter 4

Production studies of ^{155}Tb

The results, obtained in the previous chapter with the analysis of the cross sections of the reactions, are used to investigate the optimization of the ^{155}Tb production process. In the first part of this chapter the generator system is described in general terms by identifying the variables needed for the calculation of the physical quantities of interest, like activities and purities. In the second part, a particular approach based on the multi-objective optimization methods, which is applied for the first time in this field, is used to optimize simultaneously the quality and the quantity of the final product.

4.1 Chemical separation model

As described in the first chapter, this work is based on the direct activation technique. During the irradiation of the target many nuclides of different chemical elements are produced.

If one is interested in the direct production of ^{155}Tb, whose contribution is cumulated with the decay of its progenitor (^{155}Dy), only a single radiochemical process is needed to extract all its isotopes from the target.

On the contrary, if the generator system is considered, ^{155}Dy has to be extracted first and ^{155}Tb is extracted from the isolated dysprosium when sufficient quantity of terbium is produced by the decay of its progenitor.

Different variables are involved in all the steps of this process that is represented schematically in Fig. 4.1:

- the incoming energy E_{in} of the projectile, the current I_0 of the incident beam, the outgoing energy E_{out} (or the thickness of the target) and the irradiation time t_{irrad} represent the variables that characterize the irradiation step;

- the Δt_1 and Δt_2 times describe the chemical processes. The former includes the time for the removal of the target from the beamline after the end of bombardment (referred to as "waiting time" in Ref. [40]) and

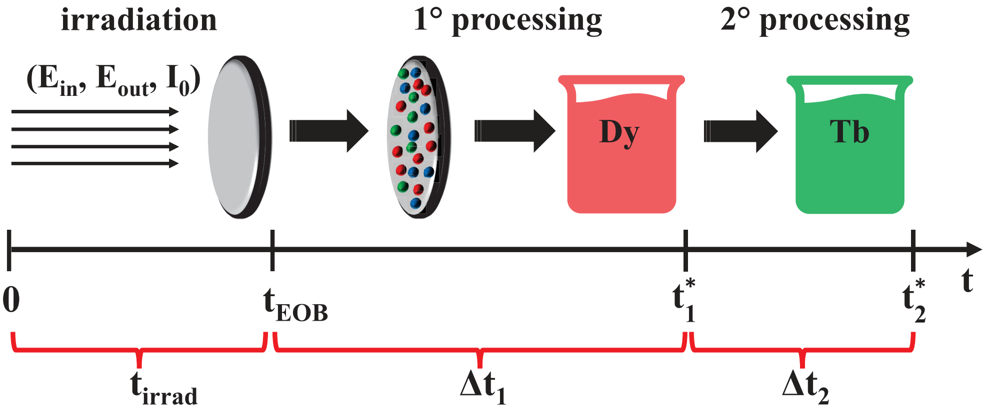

Figure 4.1: Schematic representation of the Dy/Tb generator divided in three main parts: irradiation, determined by incoming energy E$_{in}$, by beam current I$_0$, outgoing energy E$_{out}$ and by irradiation time t$_{irrad}$ (t$_{EOB}$ and t$_{irrad}$ have the same meaning and are interchangeable); first processing for the separation of Dy from the target characterized by Δt$_1$ time; second processing for extraction of Tb from isolated Dy, characterized by Δt$_2$ time.

> the time for the chemical separation. The latter includes the optimal time for the maximum growth of ^{155}Tb and the time required for the second chemical separation.

In addition, from the experimental point of view, in a realistic production process a precise control of all the experimental setup is extremely relevant. The homogeneity, the thickness and the spatial position of the target (mainly the angle at which it is mounted) as well as the spatial distribution of the energy beam can highly affect the yield and especially the radionuclidic purity. Of course also the irradiation time and the beam energy should be maintained constant during each irradiation when producing radionuclides for medical use, and all these factors will play a role in the final production yield measurements.

4.1.1 Energies for the production rate

The incoming and the outgoing energies are the key ingredients for the calculation of the optimized production rate as defined in Chapter 2 (Eq. 2.17):

$$R = \frac{I_0}{z_{proj}|e|}\frac{N_A}{A}\int_{E_{out}}^{E_{in}} \sigma(E)\left(\frac{dE}{\rho_t dx}\right)^{-1} dE, \tag{4.1}$$

valid for the case of a pure element. The two integration limits represent the energy window that has to be carefully selected to maximize the indirect production of ^{155}Tb and to minimize the co-production of its contaminants. Therefore the attention initially should be focused on the progenitors of the terbium nuclides. A preliminary idea of the energy window can be obtained by the inspection of the cross section ratio between ^{155}Dy and all the dysprosium radionuclides produced in the reactions:

$$r = \frac{\sigma_{^{155}Dy}}{\sum_j \sigma_{^{j}Dy}}. \tag{4.2}$$

The TALYS modified calculations have been used to evaluate this ratio, shown in Fig. 4.2–4.4 for all the three considered reactions. In particular, the best case is represented by the reaction with protons with a maximum over 0.8, while the worst one is represented by the reaction with α particles. This is due to a higher formation of the contaminants of ^{155}Dy especially for the reaction with α particles due to the varied composition of ^{nat}Gd. Anyway an energy window can still be selected around the peak since it corresponds to the case of higher production of ^{155}Dy with respect to its contaminants. For each reaction two considerations are important:

- an attempt has been made to avoid an excessive production at higher energies of other dysprosium radionuclides with respect to the relevant ones (like ^{152}Dy, ^{151}Dy, ...), since this can affect the final result;
- for a comparison with the literature, the window has been selected to include also the energy range used by Steyn et al. (Ref. [40]) and Moiseeva et al. (Ref. [50]) for indirect production of ^{155}Tb with protons and α particles respectively.

In particular, for the reaction with protons only the four relevant radionuclides (^{153}Dy, ^{155}Dy, ^{157}Dy and ^{159}Dy) are produced in the selected energy window 35–60 MeV, with deuterons also ^{152}Dy is produced in the range 40–70 MeV, while for the case of α particles also ^{149}Dy, ^{150}Dy, ^{151}Dy and ^{152}Dy are produced, especially from ^{152}Gd(α, x), in the range 20–70 MeV.

These ranges have been explored in the optimization study to select the two integration limits of the rate for an optimal production of ^{155}Tb.

4.1.2 Decay schemes and processing times for Bateman equations

As described in Chapter 2, the rate is used to calculate the time evolution of the produced dysprosium nuclides, by means of the Bateman equations that have been written after the analysis of the decay schemes, which are shown in detail in Appendix B. Among them, the stable isotopes and also ^{154}Dy are not relevant since they do not produce terbium nuclides. Only the branches of the decay chain that describe the production of the terbium nuclides (and not the whole decay chains) are taken into account. In particular, in this context the aim initially is to solve the decay equations only for the dysprosium radionuclides.

In a first step the equations have been solved analytically focusing the attention on the dependence on the different times and only subsequently they

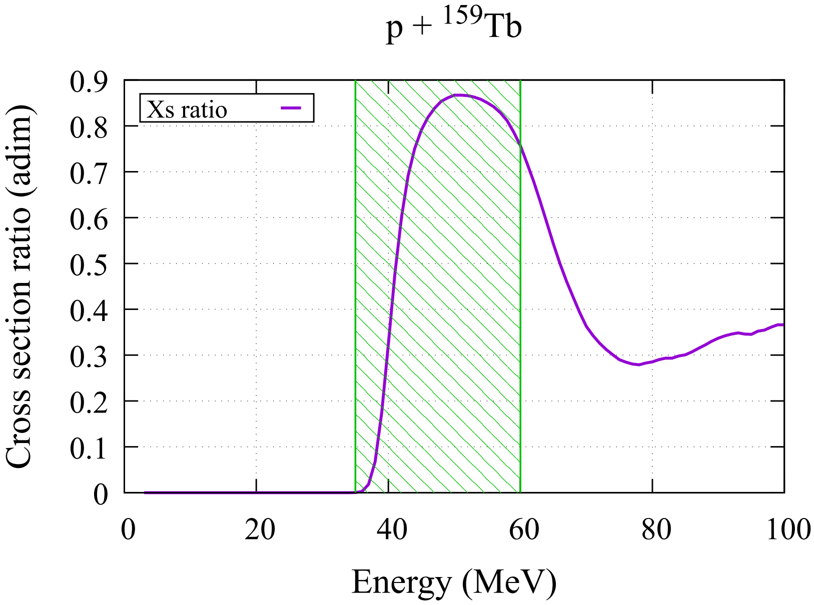

Figure 4.2: Cross section ratio for the reaction with protons. The selected energy window is 35 – 60 MeV.

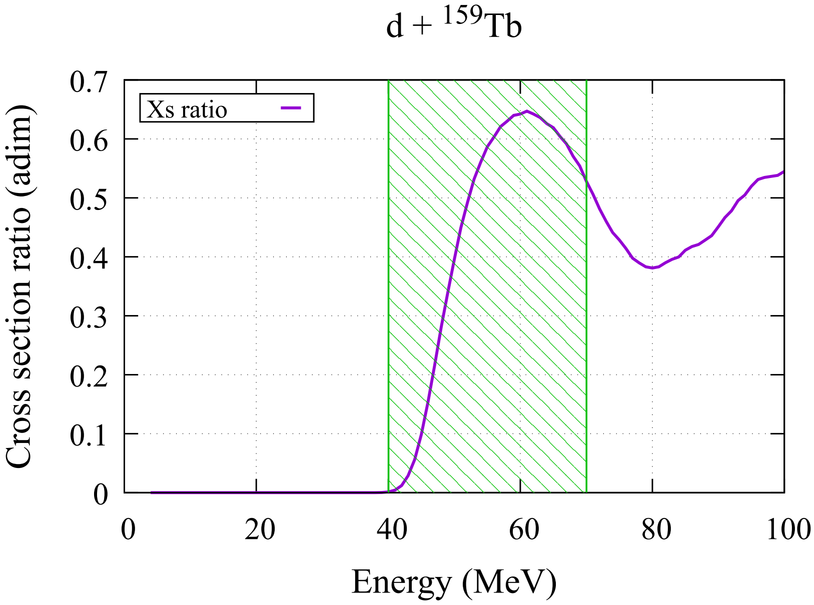

Figure 4.3: Cross section ratio for the reaction with deuterons. The selected energy window is 40 – 70 MeV.

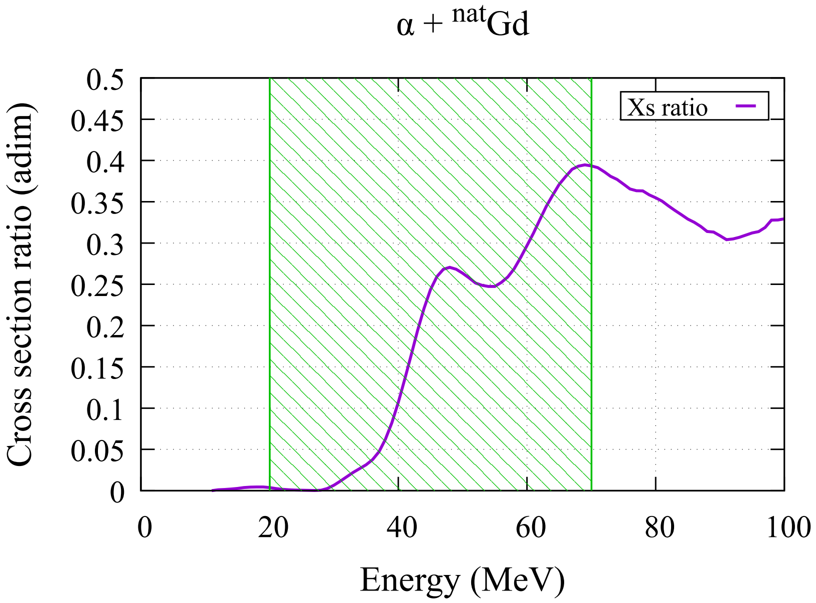

Figure 4.4: Cross section ratio for the reaction with α particles. The selected energy window is 20 − 70 MeV.

have been implemented in a code, solving the same problem numerically with the algebraic method shown in Chapter 2. In this way the code has been tested and now it is suitable to be used also for other studies for the production of new radiopharmaceuticals. Nevertheless, the analytical solutions have allowed to perform important considerations that are not clearly evident in the numerical approach regarding the involved times. Therefore in the following the first method is shown, illustrating the important observations carried out in the study, starting from the direct production of the dysprosium nuclides at the beginning of the irradiation and arriving to the final extraction of the terbium nuclides, according to the time stream of Fig. 4.1 where $t_{EOB} = t_{irrad}$.

In general, for all the dysprosium nuclides the differential equations have the same analytical form:

$$\frac{dN_{Dy}}{dt} = +R_{Dy} - \lambda_{Dy} N_{Dy} \qquad \text{for} \quad 0 \leq t \leq t_{irrad} \tag{4.3}$$

where R_{Dy} is the given by Eq. 4.1. The previous equation has the following solution:

$$N_{Dy}(t) = \frac{R_{Dy}}{\lambda_{Dy}}\left(1 - e^{-\lambda_{Dy} t}\right) \qquad \text{for} \quad 0 \leq t \leq t_{irrad}. \tag{4.4}$$

After the irradiation, the production rate vanishes and the nuclides decay according to the decay equation:

$$\frac{dN_{Dy}}{dt} = -\lambda_{Dy} N_{Dy} \qquad \text{for} \quad t > t_{irrad}. \tag{4.5}$$

From this point, the dysprosium nuclides have to be extracted from the target and at the end of the first chemical separation process, which in general occurs at time $t_1^* = t_{irrad} + \Delta t_1$, the number of available dysprosium nuclei is:

$$N_{Dy}(t_1^*) = N_{Dy}(t_{irrad}) e^{-\lambda_{Dy}\,\Delta t_1}. \tag{4.6}$$

Beyond this time, the final and explicit expression of N_{Dy} is:

$$N_{Dy}(t) = \frac{R_{Dy}}{\lambda_{Dy}}\left(1 - e^{-\lambda_{Dy}\,t_{irrad}}\right) e^{-\lambda_{Dy}\,\Delta t_1}\, e^{-\lambda_{Dy}\,t}. \tag{4.7}$$

Only from this step the production of terbium nuclides, produced by the decay of their progenitors, can be studied. The differential equations for the growth and decay of the terbium nuclides can be written as:

$$\frac{dN_{Tb}}{dt} = -\lambda_{Tb} N_{Tb} + f_{Dy\to Tb}\,\lambda_{Dy} N_{Dy} \qquad \text{for} \quad t_1^* \le t \le t_2^*, \tag{4.8}$$

where $f_{Dy\to Tb}$ is the branching ratio of the decay of dysprosium into terbium and $t_2^* = t_{irrad} + \Delta t_1 + \Delta t_2$, which is the final time when the terbium nuclides are finally extracted from the isolated dysprosium. Indeed, for $t > t_2^*$ the generator system is terminated: terbium is no more produced, but it can only decay, according to the common decay equation:

$$\frac{dN_{Tb}}{dt} = -\lambda_{Tb} N_{Tb} \qquad \text{for} \quad t > t_2^*. \tag{4.9}$$

These two equations (4.8 and 4.9) have the following solutions:

$$N_{Tb}(t) = \frac{f_{Dy\to Tb}\,R_{Dy}}{\lambda_{Tb} - \lambda_{Dy}}\left(1 - e^{-\lambda_{Dy} t_{irrad}}\right) e^{-\lambda_{Dy}\Delta t_1}\left(e^{-\lambda_{Dy} t} - e^{-\lambda_{Tb} t}\right), \tag{4.10}$$

$$N_{Tb}(t) = \frac{f_{Dy\to Tb}\,R_{Dy}}{\lambda_{Tb} - \lambda_{Dy}}\left(1 - e^{-\lambda_{Dy} t_{irrad}}\right) e^{-\lambda_{Dy}\Delta t_1}\left(e^{-\lambda_{Dy}\Delta t_2} - e^{-\lambda_{Tb}\Delta t_2}\right) e^{-\lambda_{Tb} t}. \tag{4.11}$$

These equations depend on:

- the production rate of the progenitor, that includes the cross section of the progenitor, the energy window and the beam current, which is a multiplicative factor and can be fixed;
- the irradiation and the processing times as arguments of different exponentials.

Regarding the times, the values of t_{irrad}, Δt_1 and Δt_2 are unknown, but different choices can be made in view of the optimization of the activity of ^{155}Tb, calculated using its definition: $A = \lambda N$. Looking at the previous equation, a condition for the optimization of the amount of the final product can be given by considering:

$$\begin{cases} \lambda_{Dy}\, t_{irrad} \gg 1 \\ \Delta t_1 = 0 \end{cases} \tag{4.12}$$

that corresponds to an ideal case with a very long irradiation time and an instantaneous combination of the removal of the target from the beamline and the separation of the dysprosium nuclides. Studies on the partial derivative of N_{Tb} with respect to t_{irrad} and then to Δt_1 reveal that finite and realistic optimal values can not be found for these two times. Nevertheless this ideal case is useful for the comparison of the three reactions and, moreover, other reasonable assumptions can be performed, as it will be described in the next section.

For the second processing time, instead, a different analysis can be made. The starting point is represented by the activities for dysprosium and terbium nuclides calculated from Eqs. 4.7, 4.10:

$$A_{Dy}(t) = R_{Dy}\big(1 - e^{-\lambda_{Dy}\, t_{irrad}}\big)\, e^{-\lambda_{Dy}\,\Delta t_1} e^{-\lambda_{Dy}\, t} \tag{4.13}$$

$$A_{Tb}(t) = \frac{f_{Dy\to Tb}\lambda_{Tb}\, R_{Dy}}{\lambda_{Tb} - \lambda_{Dy}}\big(1 - e^{-\lambda_{Dy} t_{irrad}}\big)e^{-\lambda_{Dy}\Delta t_1}\big(e^{-\lambda_{Dy} t} - e^{-\lambda_{Tb} t}\big). \tag{4.14}$$

These equations are referred to the same timeline ($t > t_1^*$) and allow to constrain the second processing time by taking into account that $A_{Tb}(t)$ can be written in terms of $A_{Dy}(t)$. In particular, considering a new time zero after the first chemical separation, that corresponds to fix $t_1^* = 0$, $A_{Tb}(t)$ is given by the following expression:

$$A_{Tb}(t) = \frac{f_{Dy\to Tb}\lambda_{Tb}}{\lambda_{Tb} - \lambda_{Dy}}\, A_{Dy}(0)\, \big(e^{-\lambda_{Dy} t} - e^{-\lambda_{Tb} t}\big). \tag{4.15}$$

Specializing the situation to ^{155}Tb, for which $f_{Dy\to Tb} = 1$, the growth and decay of the nuclide of interest can be described by means of the ratio between the activity of ^{155}Tb and the activity of its progenitor evaluated at this new time zero:

$$\frac{A_{^{155}Tb}(t)}{A_{^{155}Dy}(0)} = \frac{\lambda_{^{155}Tb}}{\lambda_{^{155}Tb} - \lambda_{^{155}Dy}}\big(e^{-\lambda_{^{155}Dy} t} - e^{-\lambda_{^{155}Tb} t}\big). \tag{4.16}$$

This ratio depends only on the decay constants and on time: no dependence on the irradiation parameters (the presence of the production rate has vanished), thus it is equal for all the three reactions. This function, that is represented in Fig. 4.5, can be studied analytically to detect the presence of a maximum that would correspond to the optimal Δt_2 time. Indeed, the sum of the waiting time after the first chemical separation and the time required for the second

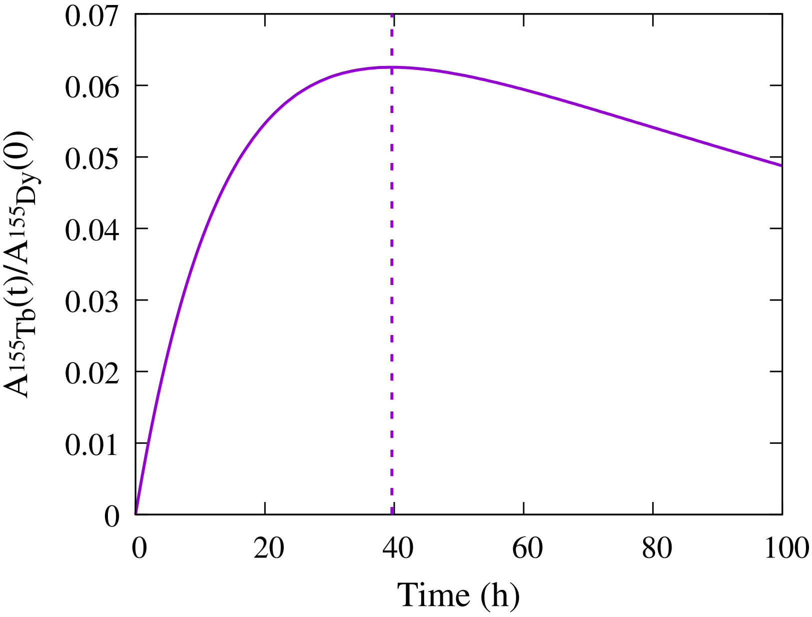

Figure 4.5: Plot of the ratio describing the growth and decay of ^{155}Tb independently of the irradiation conditions. The dotted vertical line indicates the maximum, $t_{max} \simeq 39.6$ h, which corresponds to the value of optimal Δt_2 time.

separation should be around this value. From the study of its first derivative it results that a maximum exists:

$$t_{max} = \frac{\ln \lambda_{^{155}Tb} - \ln \lambda_{^{155}Dy}}{\lambda_{^{155}Tb} - \lambda_{^{155}Dy}} \simeq 39.6 \text{ h}. \tag{4.17}$$

This procedure is general and is always applied in the study of a generator system to identify the optimal Δt_2 time. After these considerations a comparison with the literature can be made.

Comparison with the literature

A comparison with Steyn et al. for protons [40] and Moiseeva et al. for α particles [50] has been performed, while no study has been found for the reaction with deuterons. In particular, the values of some variables, involved in the calculation of the quantities of interest, are not explicitly given in the cited papers. Therefore a meticulous study has been performed to recover their results and discover the used values of the variables.

For the reaction with protons, the authors have performed an estimation of $A_{^{155}Tb}(t)$ starting from a fit of their experimental measurements using specific values for E_{in}, E_{out}, t_{irrad}, Δt_1 and Δt_2 but I_0 is not given. Consequently, in this work the same fit has been performed (Fig. 4.6) and the calculations have been carried out using the same values of the variables and considering $I_0 = 1\mu A$. Since the current is a multiplicative factor in the expression of the

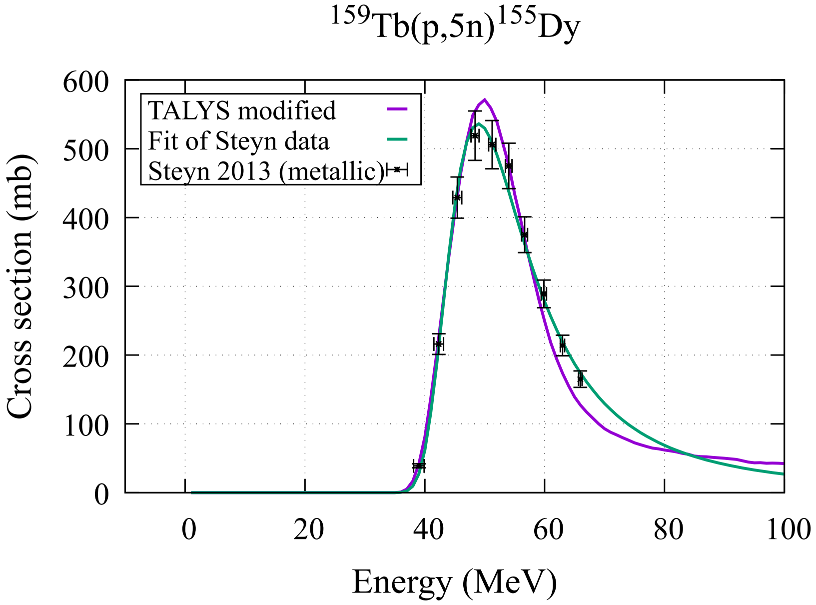

Figure 4.6: Comparison between TALYS modified curve and the fit of Steyn experimental measurements. The calculation of the activity starting from the fitted curve has allowed to determine the probable current that Steyn et al. have used in their paper.

activity, the ratio between the activity calculated by Steyn et al. and the one obtained in this work, with the described method, corresponds to the value of the current that has been considered by the authors of the papers:

$$\frac{A_{\text{Steyn}}}{A_{\text{our fit, }1\mu A}} = \frac{I_0'}{I_0} = \frac{I_0'}{1\mu A} \simeq 106. \tag{4.18}$$

After this step, the TALYS modified cross sections have been finally used and the calculations have been performed within the same conditions reported in the article and with $I_0 = 106\mu A$. The results are shown in Tab. 4.1, and they are in good agreement one each other. The main differences are due to a mild overestimation of the TALYS modified cross section of ^{155}Dy (obtained in this work) in the energy window 50–35 MeV with respect to the fit of only the Steyn experimental measurements, as represented in Fig. 4.6

For the reaction with α particles the situation is more complex since many information extremely useful for the calculations are not clearly reported. In particular the activities seem to have been calculated starting from the thick target yields, but the methods used for their calculations and the outgoing energy (probably fixed to 20 MeV) are not made explicit. Moreover, the final activity of ^{155}Tb has been calculated 40 h after the end of bombardment. Therefore, the specific values of Δt_1 and Δt_2 are not given and many combinations of these times can be considered with the constraint that their sum must be equal to 40 h. Only with the ideal case of $\Delta t_1 = 0$ h and $\Delta t_2 = 40$ h a value for the activity has been found close to the one of Moiseeva et al. as shown in Tab. 4.2, while for other combinations smaller values have been obtained.

With respect to the examples shown in the literature, to have a wider view of different ^{155}Tb production scenarios an analysis have been performed by varying the relevant variables, namely E_{in}, E_{out}, t_{irrad} and Δt_1, while in this work Δt_2 has been fixed to 39.5 h and I_0 has been kept constant to 1 μA.

E_{in}–E_{out}	$t_{irrad} + \Delta t_1 + \Delta t_2$	I_0	This Work	Steyn [40]
50–35 MeV	(10 + 1.5 + 39.5) h	106 μA	40.4 GBq	39.8 GBq

Table 4.1: Comparison of the activity of ^{155}Tb using the same values of the variables of the example found in the literature for the reaction with protons.

E_{in}–E_{out}	$t_{irrad} + \Delta t_1 + \Delta t_2$	I_0	This Work	Moiseeva [50]
60–20 MeV	(12 + 0 + 40) h	50 μA	0.95 GBq	$\sim$ 1 GBq

Table 4.2: Activity of ^{155}Tb in the ideal case of $\Delta t_1 = 0$ h used to compare the value obtained with TALYS modified and the one of the example found in the literature for the reaction with α particles.

4.2 Yield and purities optimization

Before the description of the strategy used for the optimization of ^{155}Tb, also the calculation of the integral physical yields have been carried out for the dysprosium nuclides, using the definition discussed in Chapter 2:

$$\alpha_{phys} = \left.\frac{d(A_i(t)/I_0)}{dt}\right|_{t=0}. \tag{4.19}$$

In particular, since this quantity is evaluated at the beginning of the irradiation, it has to be calculated only for radionuclides that are directly produced, like dysprosium nuclides. Using Eq. 4.4, the physical yield is:

$$\alpha_{phys} = \frac{\lambda_{Dy} R_{Dy}}{I_0}. \tag{4.20}$$

Fixing $E_{out} = 0$, the quantity can be plotted as a function of E_{in} and namely is defined as the “integral physical yield”. It has been calculated for the dysprosium nuclides for each considered reaction and the results are shown in Figs. 4.7–4.9. The reactions with protons and deuterons produce higher quantity of dysprosium nuclides with respect to the reaction with α particles. In particular the yield of ^{157}Dy is higher than the one of ^{155}Dy since ^{157}Dy

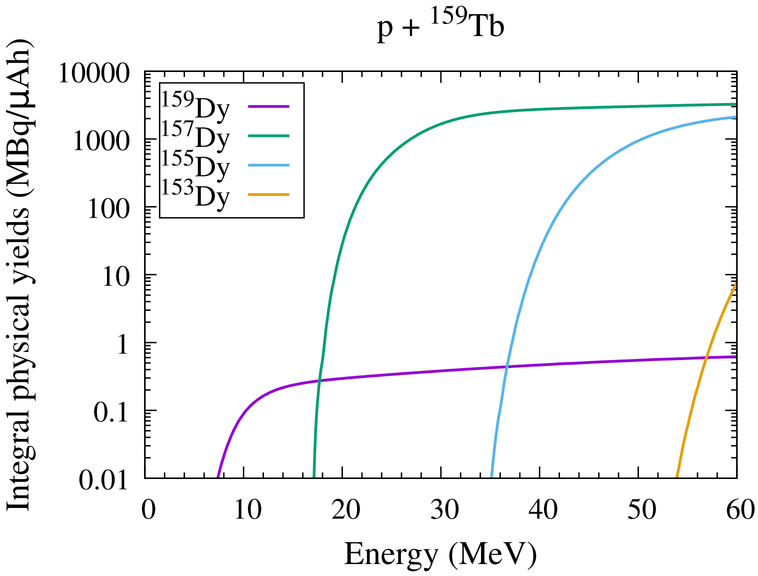

Figure 4.7: Integral physical yield for the different dysprosium radionuclides produced in the reaction with protons, with energy from 0 to the maximum value selected with the cross section ratio.

has a higher cross section, but they show a similar trend because they have comparable half-lives ($T_{1/2}$ = 8.14 h for ^{157}Dy and $T_{1/2}$ = 9.9 h for ^{155}Dy). Unfortunately from the figure it appears evident that an energy window with only the production of ^{155}Dy (that would corresponds to the production only of ^{155}Tb) cannot be found. This confirms the preliminary idea obtained from the study of the cross section ratio. However, despite the presence of other nuclides, it is important to select an energy window in which the derivative of the physical yield of ^{155}Dy is higher than the one of all the other dysprosium nuclides. This would result in a more favourable condition for the production of ^{155}Dy and therefore of the nuclide of interest.

Moreover, until now only the activity (or the yield) has been considered, but also the purities have to be calculated and the suggestion of the European Pharmacopoeia [119] (radionuclidic purity greater than or equal to 99%) has to be taken into account. The situation can be described in terms of different variables (E_{in}, E_{out}, t_{irrad} and Δt_1), from which $A(t)$, $IP(t)$, $RNP(t)$ and also $SA(t)$ have to be calculated, according to their definitions explained in Chapter 2:

$$IP(t) = \frac{N_{^{155}Tb}(t)}{\sum_j N_{^{j}Tb}(t)}, \tag{4.21}$$

$$RNP(t) = \frac{A_{^{155}Tb}(t)}{\sum_j A_{^{j}Tb}(t)}, \tag{4.22}$$

$$SA(t) = \frac{A_{^{155}Tb}(t)}{\sum_j m_{^{j}Tb}}. \tag{4.23}$$

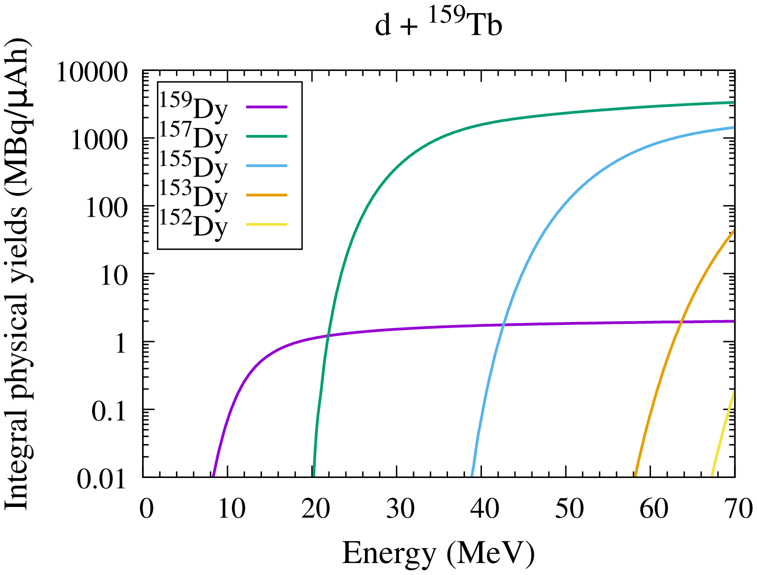

Figure 4.8: Integral physical yield for the different dysprosium radionuclides produced in the reaction with deuterons, with energy from 0 to the maximum value selected with the cross section ratio.

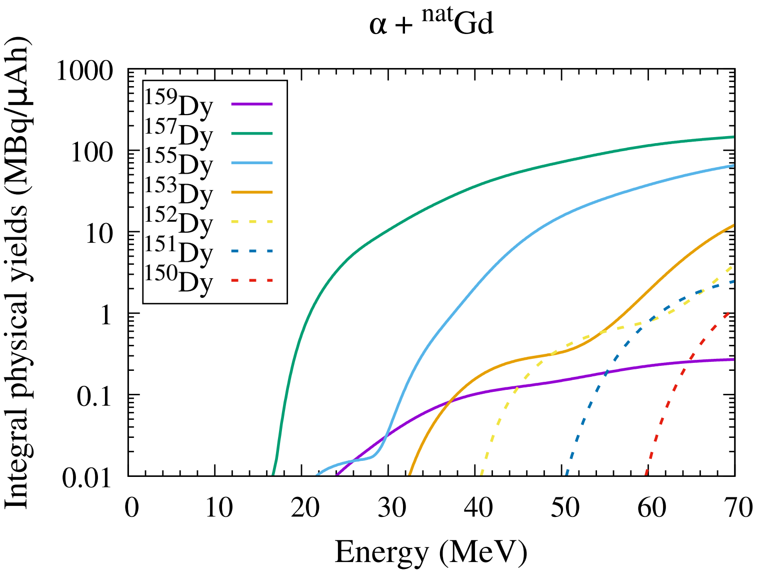

Figure 4.9: Integral physical yield for the different dysprosium radionuclides produced in the reaction with α particles, with energy from 0 to the maximum value selected with the cross section ratio.

4.2.1 Pareto frontier

The presented picture is complex and a strategy has been considered, following in general the multi criteria analysis problems faced for instance in engineering [124], but also in many other different areas (like finance and economics, to cite a few). The goal of these problems is the simultaneous optimization of many functions, namely *multi-objective optimization or Pareto optimization*, to find optimal solution in presence of trade-offs between two or more functions [125]. When considering the maximization of only a function, the maximum can be uniquely found if the function is regular and if a maximum exists. However, when considering the optimization of two or more functions, a single solution can not be determined, but a set of solutions (called “Pareto optimal” or also “non-dominated” solutions) can be identified. They are equally good in the sense that no improvement in value of one objective function can be obtained without worsening the value of one (or more) of the other objective functions. An example of multi-objective optimization problem is the maximization of the performance of a car while minimizing emissions and production cost. Another example is represented by the maximization of the production of a medical radionuclide while minimizing the co-production of its contaminants, that is equivalent to the simultaneous maximization of the activity and of the purities.

Multi-objective optimization problems have been faced for a long time and researchers carry on finding new efficient algorithms to solve them, like *evolutionary algorithm* [126] and *deep learning methods* [127]. Herein a detailed description of the mathematical methodology or of the properties of the algorithms is beyond the goal of this work, and only the important and general aspects are presented and applied in the context of the thesis. The starting point is represented by the analysis of the functions in order to select only the relevant ones. Moreover also the ranges of the variables have to be carefully chosen to avoid the exclusion of possible optimal solutions and to reduce the computational time.

In the context of this work, the maximization of the radionuclidic purity is not necessary and in particular could also be detrimental. Indeed, in the calculations the constraint on this quantity ($RNP \geq 0.99$) has to be respected [119] and it is already close to the highest possible value (the unity).

In addition, another interesting observation can be made regarding the specific activity that can be explicitly written in terms of the number of nuclides and of their molar mass $M_{^jTb}$ as:

$$SA(t) = \frac{\lambda_{^{155}Tb}\, N_{^{155}Tb}(t)}{\sum_j \frac{M_{^jTb} N_{^jTb}}{N_A}}. \tag{4.24}$$

In the ideal case of the production of only the nuclide of interest the previous expression becomes:

$$SA_{NCA}(t) = \frac{\lambda_{^{155}Tb}\, N_{^{155}Tb}(t)}{\frac{M_{^{155}Tb} N_{^{155}Tb}}{N_A}} \tag{4.25}$$

Variable	reaction	range	step
E_{in} and E_{out}	p	35 MeV → 60 MeV	1 MeV
	d	40 MeV → 70 MeV	1 MeV
	α	20 MeV → 70 MeV	1 MeV
T_{irrad}	p, d, α	0.5 h → 10 h	1 h
Δt_1	p, d, α	0.5 h → 100 h	1 h

Table 4.3: Ranges of the variables that have been chosen for the calculations of the activities and purities. Both incoming and outgoing energy have been varied within the same range, considering only the physical cases: $E_{in} > E_{out}$. All the combinations of the values have been explored.

and is referred to as "no-carrier added" (NCA) specific activity [128]. In this field, the ratio between SA and SA_{NCA} gives information about the percentage of ^{155}Tb that is realistically produced with respect to the ideal case (corresponding to its 100% production):

$$\frac{SA(t)}{SA_{NCA}(t)} = \frac{M_{^{155}Tb}\, N_{^{155}Tb}(t)}{\sum_j M_{^jTb}\, N_{^jTb}}. \tag{4.26}$$

The ratio is very similar to the expression of the isotopic purity and has a similar meaning. Consequently it is useless to maximize both IP and SA (or better SA/SA_{NCA}), and in this work the former has been preferred. However the study can be easily carried out also using the latter ratio.

Therefore the multi-objective optimization problem reduces to a "bi-criteria optimization", since the aim now is to maximize simultaneously the activity and the isotopic purity while respecting the constraint $RNP \geq 0.99$. The problem can be expressed mathematically as:

$$\begin{cases} \max A_{^{155}Tb} \\ \max IP \\ RNP \geq 0.99. \end{cases} \tag{4.27}$$

Of course the quantities have to be evaluated at the same time, and the final t_2^* time has been chosen as done similarly in the literature (see for example by Steyn et al. [40]).

To solve this problem, instead of using the modern algorithms cited above, a more "classical" or "traditional" approach has been considered since the complexity of the problem (related essentially to the number of the objective functions) has been reduced.

The first step has been represented by the selection of the ranges of the variables, that are reported in Tab. 4.3 for all the three reactions. Then a database of the quantities A, IP, RNP, SA have been created exploring all the combinations of the variable values within their limits, but considering

E_{in}	E_{out}	t_{irrad}	Δt_1	A	IP	RNP	SA
40	25	1	1	##	##	##	##
40	25	1	2	##	##	##	##
...	...	...	...	...	...	...	...
40	25	10	4	##	##	##	##
...	...	...	...	...	...	...	...
57	47	3	4	##	##	##	##
...	...	...	...	...	...	...	...

Table 4.4: Schematic structure of the created database that contains the values of the variables used for the calculations of the corresponding functions. All the possibilities of Tab. 4.3 have been considered, keeping only the combinations for which $RNP \geq 0.99$.

only those combinations for which $RNP \geq 0.99$. The calculations have been stored with a structure similar to the one shown in Tab. 4.4. Each row of the database contains the values of the variables and the corresponding values of the activities and purities. From this file, the couple of points (A, IP) of each row can be plotted in the $A - IP$ plane. From the plot the optimal set of solutions for this problem, (the set is called also "Pareto frontier"), can be easily found.

All the results are shown in Figs. 4.10–4.12 for the three considered reactions. The blue opened circles represent all the available solutions of the calculations, which have been obtained varying the variables within their limits, and all they respect the condition $RNP \geq 0.99$. The red points, instead, are the Pareto optimal solutions: they actually compose the frontier of the graph, with all the good (A, IP) couples that solve the problem. In particular, among the different non-dominated solutions, for simplicity the attention has been focused on the two extremes (A and C), that represent the best case for the purity and for the activity respectively, and on a compromise solution (B). This trade-off solution has been found considering the intersection between the frontier and the line that connects the worst case (0, 0) to the ideal point (A_{max}, IP_{max}), that corresponds to the one with the best values of activity and purity obtainable with the considered ranges for the variables. When the intersection point is not found, the closest point to the line is chosen. The values of these three points are reported in Tab. 4.5 for the three reactions, indicating not only the activity and the purity of each case, but also the values of the variables used in the calculations as well as the corresponding values of RNP, of SA and of the thickness of the considered target.

In particular, for all the three reactions the case of the maximum purity is obtained with a very small energy range, corresponding to a thin target and this scenario appears not favorable for the production of ^{155}Tb. On the other hand, the case of the maximum activity is obtained with a very short Δt_1 time for the reaction with protons and deuterons, resulting in a probable unrealistic

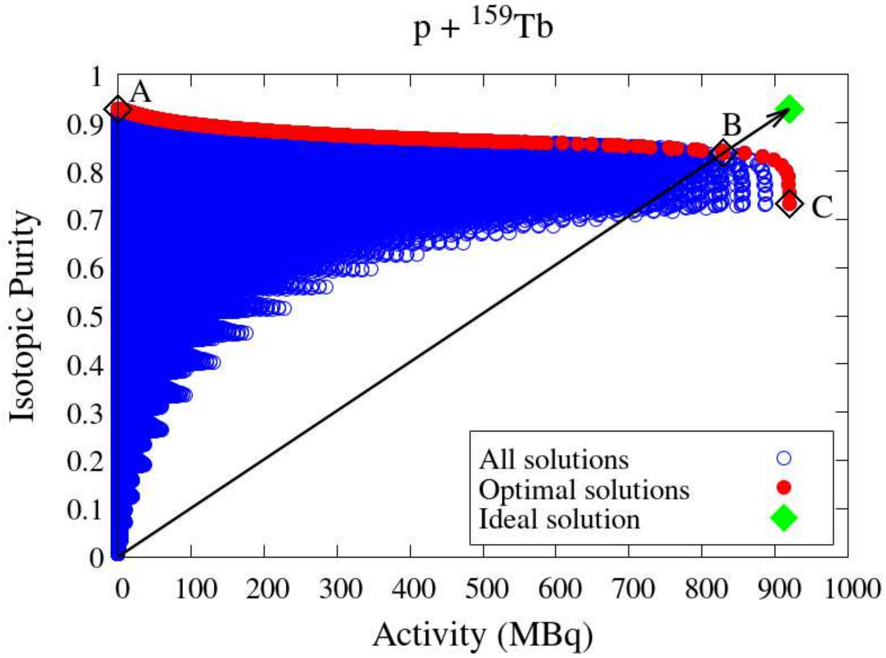

Figure 4.10: Results of the simultaneous maximization of activity and purity with $RNP \geq 0.99$ for the reaction with protons. All the solutions of the calculations are represented with blue opened circles, while the Pareto optimal solutions with red points. The green diamond represents the ideal case with with (A_{max}, IP_{max}) coordinates. Three specific cases are pointed out: A and C refer to the best solutions for the purity and the activity respectively; B refer to a trade-off solution, as described in the text.

scenario: the procedure of the removing of the target from the beamline and the separation of the dysprosium nuclides may be hardly performed in 0.5 h. The trade-off solution instead could represent a more feasible solution.

Anyway all the points of the frontier are equally valid and more realistic scenarios can be found. In this regard, the described approach is powerful since it allows to create a complete database (created only once) which can be used for other bi-criteria analyses. Indeed, for instance, one can solve the problem of the simultaneous maximization of RNP and IP, or of A and SA. On the other hand, the database allows also to apply filters to the columns to select only the combinations with specific values of the variables or of the functions. For instance, colleagues from the radiochemistry and dosimetry groups could suggest to consider particular values for the Δt_1 time or a lower limit for the specific activity. In this way preferences can be expressed and in general the more constraints one fixes on the database the more limited the Pareto frontier will be.

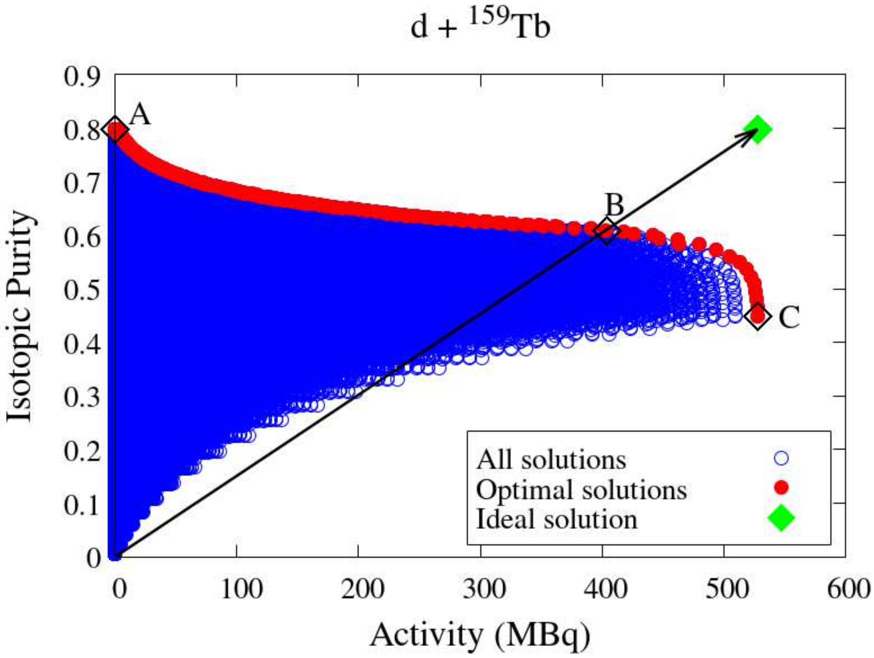

Figure 4.11: Results of the simultaneous maximization of activity and purity with $RNP \geq 0.99$ for the reaction with deuterons. The same notations of the previous figure has been used.

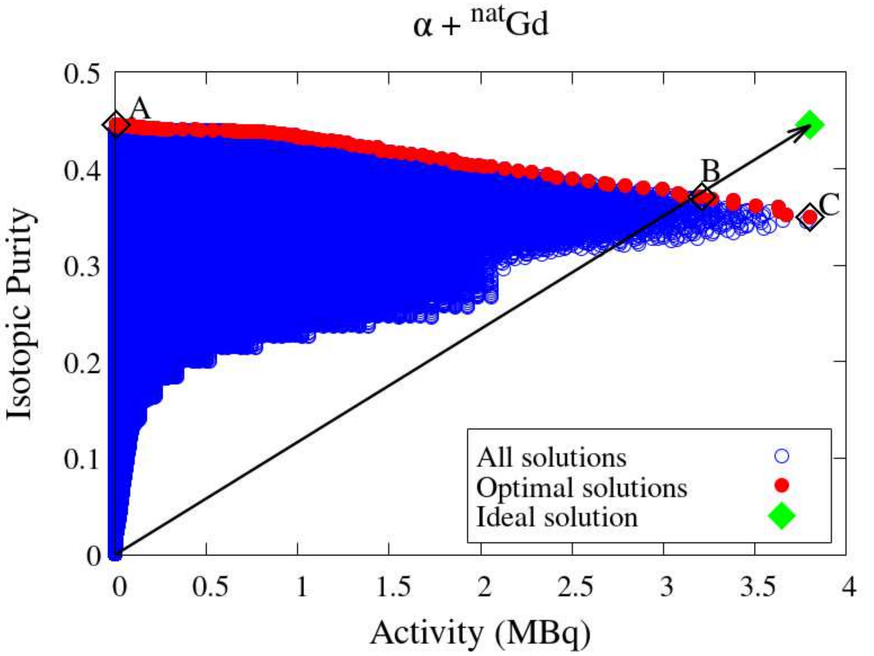

Figure 4.12: Results of the simultaneous maximization of activity and purity with $RNP \geq 0.99$ for the reaction with α particles. The same notations of the previous figure has been used.

reaction	case	E$_{in}$ (MeV)	E$_{out}$ (MeV)	t$_{irrad}$ (h)	Δt_1 (h)	A (MBq)	IP	RNP	SA (MBq/g)	Δx (mm)
p	A	51	50	0.5	62	0.06	0.93	0.9999	5.44×10^9	0.195
	B	60	43	10	1	829	0.84	0.996	4.9×10^9	3.35
	C	60	35	10	0.5	919	0.73	0.9962	4.28×10^9	4.6
d	A	62	61	0.5	72	0.02	0.8	0.9996	4.66×10^9	0.136
	B	66	53	10	1	403	0.61	0.992	3.55×10^9	1.8
	C	66	40	10	0.5	527	0.45	0.993	2.62×10^9	3.16
α	A	49	48	0.5	44.5	0.0025	0.44	0.998	2.6×10^9	0.018
	B	53	45	10	10	3.2	0.37	0.99	2.16×10^9	0.144
	C	52	43	10	8	3.8	0.35	0.99	2.04×10^9	0.16

Table 4.5: Values of the variables and of the functions for the three cases (A, B, C) for each reaction. The thickness of the target has been calculated using the ATIMA web tool developed and maintained by GSI Helmholtz Centre for Heavy Ion Research (https://web-docs.gsi.de/ weick/atima/).

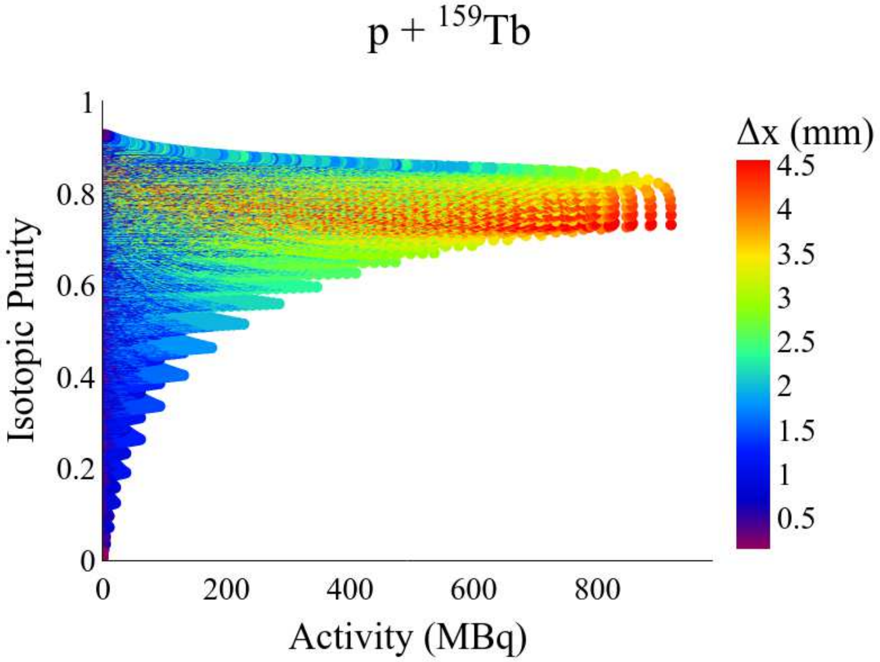

Figure 4.13: This figure represents the same plot of Fig. 4.10, showing, with a colorscale, also the dependence of the thickness of the target (Δx) for each solution.

Moreover, the solutions can also be graphically represented in other ways using, for example, colorbars to show the variability of the solutions with respect to a specific variable or function, or instead with the use of heatmaps. For instance, all the solutions for the reaction with protons can be represented with the dependence on the thickness of the target, as shown in Fig. 4.13. The figure points out that larger targets ($\Delta x > 2$ mm) allow to obtain high values of both activity and isotopic purity. This behaviour is also confirmed by Fig. 4.14 that shows the variability of the SA/SA_{NCA} ratio in the E_{in}–E_{out} plane for the reaction with protons under specific time conditions: $t_{irrad} = 10$ h and $\Delta t_1 = 1.5$ h.

In this work, a particular code has been written that allows to create a dashboard and to interact dynamically with the database, exploring many different possibilities. Needless to say that other ranges could be chosen for the variables, as considering also t$_{irrad}$ even to 100 h, or using smaller time steps.

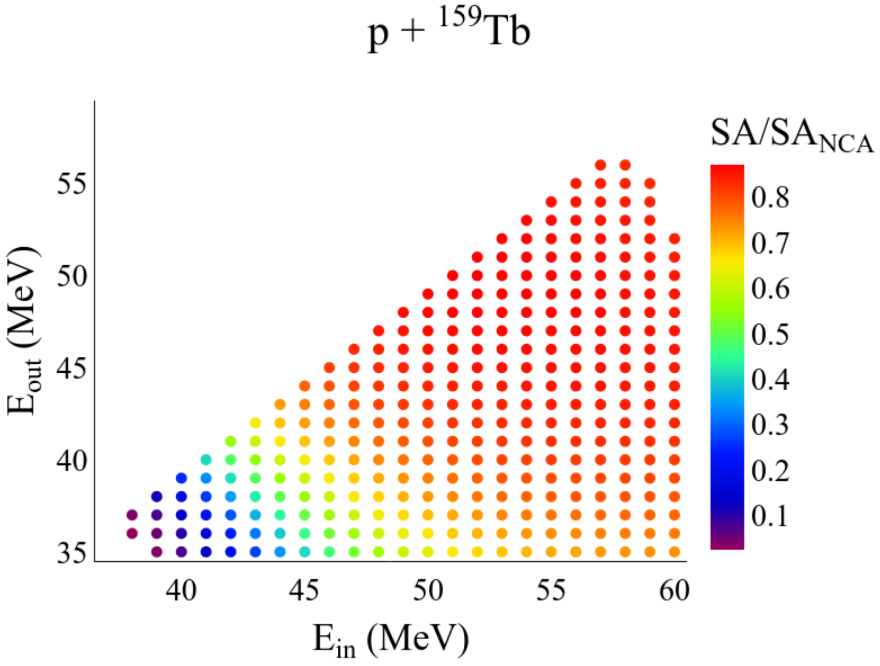

Figure 4.14: Another example of a plot that can be obtained from the database. This figure shows, in the E_{in}–E_{out} plane, all the combinations of the energies for the reaction with protons, with $RNP \geq 0.99$, $t_{irrad} = 10$ h and $\Delta t_1 = 1.5$ h. The colors show the variability of the value of the ratio SA/SA_{NCA}.

The used approach is particularly suitable when only two functions are considered, while for a higher number of functions more complex algorithms should be used. However, the described approach is general and is innovative in this field: it can be used also for the study of other radionuclides, directly or indirectly produced. As an example, in Appendix B the results obtained with this approach are shown for the reaction ^{160}Gd(α, t)^{161}Tb that has been studied by re-scaling the cross section of the ^{nat}Gd(α, x)^{161}Tb reaction, described in Chapter 3.

Finally, from the results shown in the figures and in the table, the reaction with protons seems to represent the most promising route for the production of ^{155}Tb among the three considered generator reactions. However, these routes have been compared with the standard ^{155}Gd(p, x)^{155}Tb reaction whose results have been published very recently [129], as it will be shown in the next chapter.

Chapter 5

Comparative analysis of optimized ^{155}Tb production routes

In the previous chapters, the accurate analysis of the cross sections has led to optimized calculations of activities and purities for ^{155}Tb, for all the three generators. In this chapter, we perform comparative analyses to complete the study of the three indirect production routes. In particular, in the first part of the chapter the comparison with standard calculations (such as the ones provided by the available online tools by IAEA [130] or the simulated data libraries distributed as TENDL, upon which many calculations found in the literature are based) is shown to further assess the effects of the used approach. Then, the three generators are compared to each other in order to find the most promising route for the production of ^{155}Tb.

Finally, in the second part of the chapter we show the problem of the production of the nuclide of interest from a different but complementary point of view, like the one of a *nuclear physician*. The purely theoretical (and physical) description carried out so far is based on the identification of the best parameter values that optimize ^{155}Tb production in each considered reaction. Nevertheless, it is interesting to examine the problem also in a more practical way, for example by considering the need to treat as many patients as possible, with lower activity values and without waiting for too long. This approach will allow to identify and explore additional peculiar features of the three generators.

5.1 Comparison with standard calculations

In Chapter 3 the validation analyses have shown that the TALYS modified curves offer a better description of the cross sections for each generator than the TENDL curves. Additionally, it is now important to evaluate the effects of these improvements on the cross sections by comparing the calculations of activity and purity of ^{155}Tb evaluated using both TALYS modified and TENDL cross sections. In particular, the recent tool developed by IAEA, Medical Isotope Browser (here briefly referred to as ISOTOPIA, which is the name of the webpage) [130, 131, 132], has been considered since it automatically uses by default the TENDL cross sections. In addition, also the Monte Carlo approach has been taken into account and calculations obtained with PHITS are also added to the comparison between TALYS modified and TENDL.

With ISOTOPIA the user can retrieve the calculation of the activities at the end of bombardment for all the products of a reaction by specifying few parameters: the projectile, the target (and eventually also its composition), the incoming energy, the outgoing energy (or the thickness of the target), the current and the irradiation time. Using the PHITS code the same user can proceeds similarly, defining the target as a cylinder of arbitrary radius (e.g. 1 cm) with the desired thickness, considering a pencil beam with specific energy and indicating the current and the irradiation time. However, both ISOTOPIA and PHITS do not allow to study indirect productions, but they provide the activity of the progenitor at the end of bombardment, $A_{Dy}(t_{EOB})$. Consequently, terbium activity can be calculated at the end of the second chemical separation (*i.e.* at $t = t_2^* = t_{irrad} + \Delta t_1 + \Delta t_2$) by using this equation (see Chapter 4):

$$A_{Tb}(t_2^*) = \frac{f_{Dy\to Tb}\,\lambda_{Tb}}{\lambda_{Tb} - \lambda_{Dy}}\,A_{Dy}(t_{EOB})\,e^{-\lambda_{Dy}\Delta t_1}\left(e^{-\lambda_{Dy}\Delta t_2} - e^{-\lambda_{Tb}\Delta t_2}\right). \tag{5.1}$$

The following values have been chosen for simplicity:

- E_{in}–E_{out}=60–35 MeV for protons, E_{in}–E_{out}=66–40 MeV for deuterons and E_{in}–E_{out}=52–43 MeV for α particles;
- I_0=1 μA, t_{irrad}=1 h and Δt_1=11.5 h for each reaction.

The results are shown in Tab. 5.1 and confirm what has been observed with the analysis of the cross sections: the TALYS modified curves used in this work allow to obtain greater values of activities and purities with respect to the one based on the TENDL curves. Moreover, the cross section improvements are more evident especially for the reaction with protons, while for the other two the results of this work and ISOTOPIA are similar. On the other hand, PHITS gives a description similar to ISOTOPIA only for the reaction with protons, while it shows a very different behaviour with the other two generators. In particular, it probably underestimates the cross section of ^{155}Dy with the reaction with deuterons, while overestimating it for the one with α particles. Regarding the latter reaction, the agreement between TALYS modified and the experimental estimations performed by Moiseeva et al. [50], shown in the previous chapter in Tab. 4.2, confirms the choice to use the TALYS modified cross section in this study. Moreover, in general, both ISOTOPIA and PHITS do not satisfy the RNP requirement and the explanation relies on a higher production of contaminants, in particular of ^{153}Dy, as shown in Tab. 5.2. Indeed, as described in the previous chapters, among all the other dysprosium

Reaction	Code	A (MBq)	IP	RNP	SA (MBq/μA)
p	This work	57.15	0.75	0.997	4.4×10^9
	ISOTOPIA	47.2	0.71	0.976	4.15×10^9
	PHITS	41.6	0.7	0.986	4.07×10^9
d	This work	32.8	0.48	0.995	2.77×10^9
	ISOTOPIA	30.9	0.40	0.977	2.33×10^9
	PHITS	16.5	0.40	0.980	2.28×10^9
α	This work	0.4	0.35	0.990	2.03×10^9
	ISOTOPIA	0.4	0.36	0.980	2.08×10^9
	PHITS	2.1	0.39	0.950	2.25×10^9

Table 5.1: Comparison of the results obtained in this work with the standard calculations of ISOTOPIA and PHITS.

Reaction	This work	ISOTOPIA	PHITS
p	7.30 MBq	51.47 MBq	26.89 MBq
d	7.48 MBq	32.3 MBq	14.82 MBq
α	0.16 MBq	0.37 MBq	5.2 MBq

Table 5.2: Comparison of the activity of ^{153}Dy at t=t$_{EOB}$ = 1 h. In this work the lowest values are obtained and this reflects to a higher prediction of RNP.

nuclides ^{153}Dy is the main contaminant of ^{155}Dy and an overestimation of its cross section (see Fig. 3.7) clearly have radical effects on the purity of the final product.

Consequently, the results of ISOTOPIA and PHITS, that are not based on a careful analysis and tuning on experimental data of the cross section, would suggest to exclude all the three generators as not promising for clinical applications of ^{155}Tb, due to insufficient RNP. This further reinforces the cross section analysis performed in this work and makes the calculations based on TALYS modified more accurate than the other ones.

5.2 A promising reaction for ^{155}Tb production?

5.2.1 Comparison of generators

In the field of production of medical radionuclides, reactions are usually compared using the integral physical yield (Eq. 4.19), but for generators this definition loses its meaning since it is evaluated at the beginning of the irradiation. Therefore this quantity is suitable in studies of radionuclides that are directly produced, while with generators a new method must be found. The study described in the previous chapter has showed that for each reaction there are several possibilities for the production of ^{155}Tb, but to compare them from a theoretical point of view, it is useful to take the expression of the activity per unit current evaluated at the end of the second chemical separation, *i.e.* at $t = t_2^*$:

$$\frac{A_{Tb}(t_2^*)}{I_0} = \frac{f_{Dy\to Tb}\,\lambda_{Tb}\,R'_{Dy}}{\lambda_{Tb} - \lambda_{Dy}}\left(1-e^{-\lambda_{Dy}t_{irrad}}\right)e^{-\lambda_{Dy}\Delta t_1}\left(e^{-\lambda_{Dy}\Delta t_2}-e^{-\lambda_{Tb}\Delta t_2}\right), \quad (5.2)$$

where R'_{Dy} indicates the production rate per unit of current. On the basis of Eq. 2.17, its expression is given by:

$$R'_{Dy} = \frac{R}{I_0} = \frac{1}{z_{proj}|e|}\frac{N_A}{A}\int_{E_{out}}^{E_{in}} \sigma(E)\left(\frac{dE}{\rho_t dx}\right)^{-1} dE. \quad (5.3)$$

and it is calculated with a specific energy window that corresponds to a target thickness such that the beam is completely stopped inside it, representing therefore an "integral yield", using the definitions presented in Chapter 2. More specifically, E_{out} is set at the threshold energy of each reaction, while E_{in} is identified in the range previously found ([35–60] for protons, [40–70] for deuterons and [20–70] for α particles) in order to maximize the activity, always respecting the condition RNP$\geq$0.99.
Then, we can consider the ideal case discussed in Chapter 4 for the production of ^{155}Tb (long irradiation time and instantaneous chemical separation process, Eq. 4.12) that can be described by the following limit:

$$\lim_{\substack{t_{irrad}\to+\infty \\ \Delta t_1\to 0}} \frac{A_{Tb}(t_2^*)}{I_0} = \frac{f_{Dy\to Tb}\,\lambda_{Tb}\,R'_{Dy}}{\lambda_{Tb} - \lambda_{Dy}}\left(e^{-\lambda_{Dy}\Delta t_2} - e^{-\lambda_{Tb}\Delta t_2}\right) = a_{sat}^{int}. \quad (5.4)$$

In this way, Eq. 5.4 expresses a "saturation integral yield" (in MBq/μA unit), in accordance with the definitions described in Chapter 2 and in Ref. [118], and makes it possible to compare reactions under similar conditions.

The results are compared in Tab. 5.3, where it is evident that among the reactions the one with protons appears clearly as the best in terms both of yield and purities. This is due to the considered energy window that corresponds to a very thick target ($\sim$ 4.5 mm), able to tolerate also high current values and capable of a higher production of ^{155}Tb, by a factor of approximately 100 with respect to the reaction with α and 1.66 with respect to the one with deuterons. Moreover from 60 MeV to 35 MeV fewer contaminants are produced in this reaction than in the other two. Indeed, the reaction with deuterons allows to obtain a high yield, but a very low isotopic purity, due to a higher production of the stable ^{159}Tb from the decay of its progenitor ^{159}Dy.

On the other hand, the reaction with α particles offers the lowest yield of ^{155}Tb and does not satisfy the RNP$\geq$0.99 requirement. Indeed, the varied composition of natural gadolinium (discussed in Chapter 3) results in a greater

reaction	p	d	α
E_{in}–E_{th} (MeV)	60–35	67–38	53–12
Δx (mm)	4.6	3.5	0.55
$\mathbf{a_{sat}^{int}}$ (MBq/$\boldsymbol{\mu}$A)	**1891**	**1139**	**19**
IP	0.7	0.41	0.07
RNP	0.997	0.992	0.98
SA (MBq/g)	4.07×10^9	2.37×10^9	4.27×10^8

Table 5.3: Comparison of the three reactions by means of the saturation integral yields explained in the text. Regarding the energies, E_{th} refers to the threshold energy, while for the thickness of the target the ATIMA web tool has been used (https://web-docs.gsi.de/ weick/atima/).

production of contaminants and Δt_1 must be greater than zero in order to reach higher values of radionuclidic purity. A deeper study of this route has allowed to verify that $\Delta t_1 = 15$ h is the minimum value of the first processing separation time for which RNP= 0.99 in the energy range 53–12 MeV, but with this choice the saturation integral yield and also the isotopic purity decrease with respect to the ideal case: $A = 6.67$ MBq/μA and $IP \sim 0.03$.

To improve the results with α we have also considered the use of an enriched gadolinium target in an attempt to get new insights and refine the comparison. Consequently, a further study has been performed by rescaling the TALYS modified cross sections of the ^{nat}Gd(α, x) reaction to simulate the ^{155}Gd(α, x) reaction, where the target is 100% enriched. This represents an ideal picture currently not experimentally feasible, even if targets with lower ^{155}Gd enrichment are commercially available, as the one used by Dellepiane et al. (its composition is reported in Tab. 5.4) to study the direct production of ^{155}Tb with the ^{155}Gd(p, x) reaction [129], which will be considered in the next section. In this thesis, both enrichment cases have been explored and the results of their saturation integral yields are shown in Tab. 5.5. These two reactions allow to obtain higher values of yield than the one with ^{nat}Gd, and in terms of purities they compete with the reaction with protons. Nevertheless, the achievable yield is still the lowest in comparison with the other two reactions that are based on the use of a natural target. In addition, taking also into account the possible higher costs for the target enrichment and for the beam current, these routes are less advantageous with respect to the one with protons, which still is the most promising.

5.2.2 Comparison with direct production on enriched targets

As also mentioned in the previous chapters, generators are not the only way to produce radionuclides, and many studies of direct production can be found in the literature. The three reactions studied in this work allow also the direct

	^{152}Gd	^{154}Gd	^{155}Gd	^{156}Gd	^{157}Gd	^{158}Gd	^{160}Gd
natural	0.002	0.0218	0.1418	0.2047	0.1565	0.2484	0.2186
^{155}Gd-enr	<0.0002	0.005	0.919	0.0587	0.0081	0.0065	0.0027

Table 5.4: Comparison of the composition of natural gadolinium and the commercially available target (http://www.isoflex.com/), enriched in ^{155}Gd, used in Ref. [129].

reaction	α + ^{155}Gd (100% enr.)	α + ^{155}Gd (91.9% enr.)
E_{in}–E_{th} (MeV)	59–34	59–28
Δx (mm)	0.42	0.5
a_{sat}^{int} (MBq/μA)	**136**	**127**
IP	0.914	0.74
RNP	0.992	0.991
SA (MBq/g)	5.35 $\times 10^9$	4.32 $\times 10^9$

Table 5.5: Comparison of the reactions with α particles on ^{155}Gd 100% enriched and with the commercially available enrichment [129].

production of ^{155}Tb, as shown in Chapter 3 with the cross sections plots. Nevertheless, in addition to the nuclide of interest also many other terbium nuclides are produced, that can affect the purities. Specifically, among them the worst contaminant is represented by ^{156}Tb due to its half-life ($T_{1/2}$ = 5.35 d) that is almost equal to the one of ^{155}Tb ($T_{1/2}$ = 5.32 d). If the cross sections of the contaminants are comparable with that of ^{155}Tb, the final product does not satisfy the RNP$\geq$0.99 requirement. This is precisely the case with the considered reactions and therefore other nuclear reactions, based on highly enriched targets, have to be carefully investigated for the direct production of ^{155}Tb.

As stated before, the ^{155}Gd(p, x) reaction has been selected as a promising route and very recently the first experimental measurements of cross sections and integral physical yields have been performed [129, 133] in the energy range from 5 MeV to 18 MeV, covering the region of the ^{155}Tb cross section peak. This reaction is particularly interesting since it allows the production of ^{155}Tb using low-energy cyclotrons, like the ones available in hospitals. Another advantage is represented by the use of a high enriched target in ^{155}Gd, which should increase the production of ^{155}Tb while reducing the presence of the contaminants.

Different estimations of the ^{155}Tb yield have been performed also to study the feasibility of this route with medical cyclotrons and the obtained yield is around 3.3 MBq/μAh. Using the definitions of yields [118], from this yield the saturation activity can be evaluated:

$$a_{sat} = \frac{\alpha_{phys}}{\lambda} \sim 608 \text{ MBq}/\mu\text{A}. \tag{5.5}$$

This value indicates that, considering the same enriched target, the ^{155}Gd(p, x) direct reaction is more advantageous than the ^{155}Gd(α, x) indirect reaction. Indeed, even if the cross sections are high in both cases, the total range of α particles is much shorter than that of protons. This effect produces fewer nuclides in the ^{155}Gd(α, x) reaction and therefore a smaller yield with respect to the reaction induced by protons [134]. Nevertheless the ^{155}Gd(p, x) reaction does not allow to respect the RNP constraint: the purity ranges from around 50% at the end of bombardment to 94% at 96 h after the beginning of the irradiation. Unfortunately, this is mainly caused by the presence of ^{156}Tb which can not be removed from the sample due to its half-life [129].

Probably higher enrichments may provide the desired RNP, and consequently further studies are demanded in this context to find the minimal percentage in the enrichment of the target to fulfill the requirement on the radionuclidic purity. Moreover, theoretical studies for the reproduction of the cross sections, as done in this work (see Chapters 2 and 3), will help to evaluate more precisely the activities and the purities, and also dosimetry studies will establish the impact of ^{156}Tb if administered to a patient.

In summary, as emerged from this last comparison, the main problem for the direct production of ^{155}Tb is its main contaminant, ^{156}Tb, with similar half-life. With the generators, ^{156}Tb can not be produced at all by the decay of the isolated dysprosium: ^{156}Dy is stable, as many other dysprosium nuclides. This explain the high RNP values obtained with all the three reactions studied in this work.

Therefore from these results at the moment the generator reactions are the more favourable for the production of ^{155}Tb and the one with protons seems currently the best route, that allows to obtain 115 MBq with IP=0.7 and RNP=0.996 at the final time t= $1 + 1.5 + 39.5$ h= 42 h considering the energy range E$_{in}$–E$_{out}$=60–35 MeV and I$_0$=1 μA for the beam current.

5.3 Additional analysis in a realistic scenario

So far the comparison has been made from a theoretical point of view considering the optimum value for the second processing time $\Delta t_2 = 39.5$ h. However, the problem of producing ^{155}Tb could also be seen from the point of view of a *nuclear physician*, who is focused on a different optimization: instead of having an optimal activity with a single extraction, the aim may be to perform as many extractions as possible from the same generator, obtaining ^{155}Tb more often even if characterized by a lower activity. Indeed, the main advantage of a generator is the possibility to have an apparatus that can deliver the nuclide of interest constantly and for a long time. In this way it can be used in the

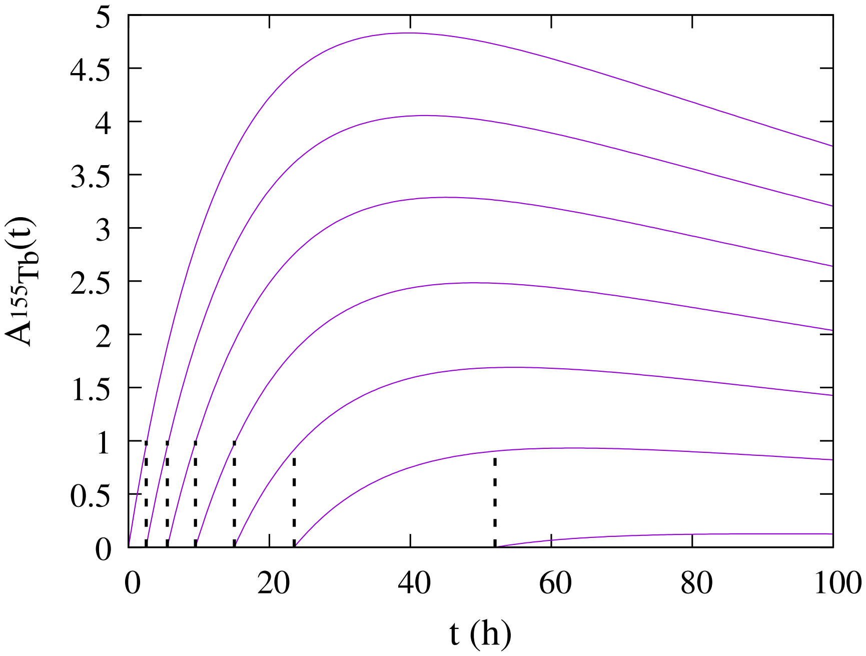

Figure 5.1: Example of the re-evaluation of the activity of ^{155}Tb as a result of many extractions with A∼ 0.9–1 GBq each. The times for the extractions are indicated by the grey dotted lines and their values are reported in Tab. 5.6 together with the corresponding values of activity and purities.

clinic for many days and for many patients, each of which may require the administration of different values of activity depending on the organ to scan and also on the weight of the patient [135, 136].

Therefore the results and the equations obtained in this work could help physician to plan the diagnostic and/or therapeutic treatment of patients, since a nuclear physicist can select the most promising reaction and then can provide the physicians with a "timetable" for the extractions of ^{155}Tb, according to needs.

Here in the following a short example shows a way of "milking" the generator as much as possible, referring to the milking analogy of the Ra-Rn generator mentioned in Chapter 1 [137].

One can consider the generator with protons using the following irradiation parameters that could describe a realistic production scenario: $t_{irrad} = 1$ h, I_0=50 μA, E_{in}–E_{out}=60–35 MeV and $\Delta t_1 = 4$ h. Indeed, the experimental studies of Steyn et al. have shown calculations with higher current and irradiation time, while in the work of Moiseeva et al. a shorter time have been used experimentally for the first chemical separation ($\Delta t_1 = 1.5$ h). Therefore the selected values can be considered more than adequate for a realistic production of ^{155}Tb with the generator.

At the end of the first chemical separation (at $t = 5$ h), the available

t* (h)	Δt_2 (h)	A (GBq)	IP	RNP
2.5	2.5	0.96	0.73	0.993
5.5	3	0.94	0.74	0.994
9.5	4	0.98	0.75	0.995
15	5.5	0.97	0.76	0.996
23.5	8.5	0.92	0.78	0.997
52	28.5	0.9	0.80	0.998

Table 5.6: Example of times of extractions of ^{155}Tb with the corresponding values of its activity and purities, with reference to Fig.5.1. In particular, regarding the Δt_2 time, for the first extraction it corresponds to the optimal time t*, while for the other case is given by the difference between the corresponding optimal time and the previous one.

quantity of ^{155}Dy is A $\sim$ 77 GBq from which the optimal value of the activity of ^{155}Tb is A$\sim$ 4.83 GBq, obtainable at $t = t_2^* = 5 + 39.5$ h. If the physicians need a particular value of the activity, different extractions can be performed considering these steps:

1. the activity of ^{155}Tb as a function of the time after the first chemical separation has to be taken into account. As done in the previous chapter, for simplicity, a new time zero can be fixed at t=t_1^* = 5 h;
2. looking to the trend of the function, the time corresponding to the desired activity, t^* can be identified for the first extraction of terbium from the isolated dysprosium. This corresponds exactly to a new Δt_2 time.
3. At this time, inside the apparatus, of course, terbium is no more present and the activities of the dysprosium nuclides decrease by $e^{\lambda_{Dy} t^*}$.
4. Consequently, from this time forward, the activities of terbium have to be re-evaluated considering the new values of A$_{Dy}$ and then all these steps can be repeated again.

An example of this procedure, considering the same timeline, is shown in Fig. 5.1 that describes the activity of ^{155}Tb after each separation. The values of the optimal times and the corresponding activities and purities are reported in Tab. 5.6 where also the Δt_2 times are indicated. In particular, since the curves are shown with the same timeline, for the first extraction Δt_2 corresponds exactly to the optimal time t*, while for the other ones it is obtained from the difference between the corresponding optimal time and the previous one. The values of the table indicate that 6 patients could be treated with A $\sim$ 0.9 GBq each for a total amount of $\sim$ 5.7 GBq, higher than the optimal value obtainable with a single separation. For $t > 52$ h similar values of the activity can no longer be achieved, as suggested by the last line in the figure that remains

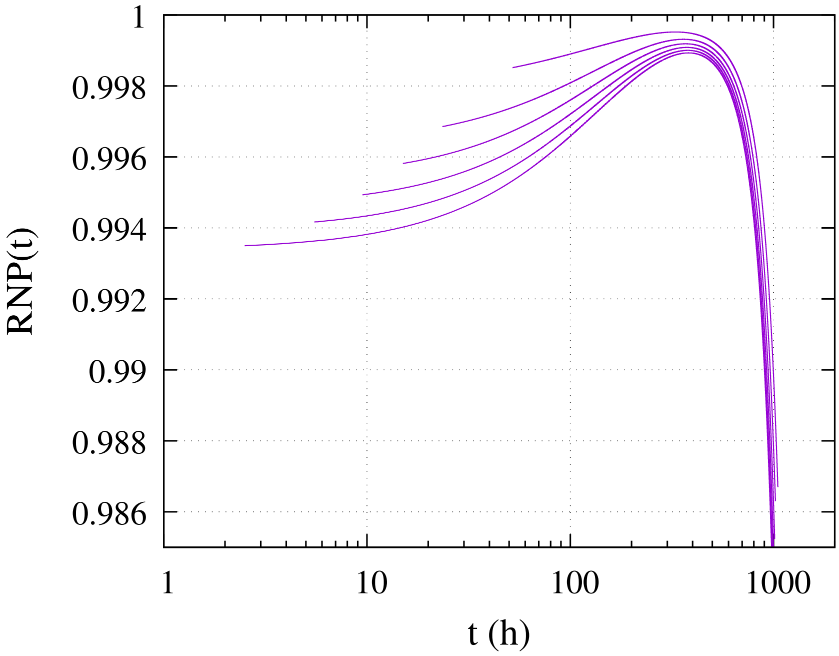

Figure 5.2: Time dependence of the radionuclidic purity for the six cases reported in Tab. 5.6.

below 0.5 GBq, but many other extractions with very low values ($\lesssim$ 100 MBq) can be performed if needed. On the other hand, of course, different timetables can be planned if higher or lower values of activities are required. In this way, the desired values of the activity can be obtained with high purities without waiting for days. Indeed, as indicated in Tab. 5.6, the first five extractions can be made in a single day.

Moreover, in view of the clinical use of ^{155}Tb, it is interesting to monitor how long the radionuclidic purity remains over 0.99. For this reason, one can study the time dependence of the radionuclidic purity of the six cases of Tab. 5.6, starting when each nuclide is extracted from the generator. The obtained curves are shown in Fig. 5.2 where the rise is due to the decay of ^{153}Tb which vanishes faster than ^{155}Tb, while the decrease of the curves is the result of the presence of the long half-life contaminant (^{157}Tb, $T_{1/2}$ ~71 y) and of the decay of ^{155}Tb. From the figure it is evident that RNP remains over 0.99 for ~37.5 days (900 hours), i.e. about 7 times the half-life of ^{155}Tb, which ensures the use of this radionuclide also to study long biological processes. In addition, this result confirms the possibility to perform further multiple (low-activity) extractions of ^{155}Tb with RNP$\geq$0.99 for about a month.

Therefore, on this basis, generators prove to be excellent instruments to be used in nuclear medicine, and those described in this work seem to be interesting to increase the availability of ^{155}Tb for its clinical applications.

Conclusions

This thesis presented a simulation study of three generator–based nuclear reactions on natural targets for the production of ^{155}Tb. The work extends the recent studies of these generators, from the description of the cross sections to the calculations of activity and purities of the final product.

For the cross sections, an attempt has been made to give a description of the problem driven mainly by physical principles: this allowed, for each reaction, to give a theoretically consistent and strong representation of the cross sections of the main dysprosium nuclides. In particular, the inclusion of rotational effects and the variation of the pre-equilibrium parameters, together with the use of an equidistant binning for the de-excitation energy and the optimization of the ^{153}Dy level density, have improved the agreement of the cross sections with the experimental data, as also verified by the calculation of the total chi-square. Remarkable results have been obtained for the reaction with protons and deuterons, while a slight enhancement have been achieved for the one with α particles.

Thereafter, a study was conducted to understand the dependence of the activities and purities on the incoming and outgoing energies and on irradiation and radiochemical separation timings. In particular, starting from the new cross sections, activity and purity have been calculated considering accurately the decay schemes. More specifically, the optimal time for the extraction of terbium from the isolated dysprosium has been determined ($\Delta t_2 = 39.6$ h) by considering the decay characteristics of ^{155}Tb and of its progenitor. From this step, an optimization study has been performed by exploring different combinations of E_{in}, E_{out}, t_{irrad} and Δt_1, and the comparison with the experimental estimations found in the literature (based on empirical interpolations of the experimental data) confirms and reinforces the reliability of the work done on the cross sections.

In this analysis, an original approach has been used for the first time in this field, obtaining the so-called Pareto frontier: a set of many solutions that simultaneously maximize both activity and isotopic purity, while at the same time respecting the condition on radionuclidic purity (RNP>0.99). The method is so general that it can also be applied to direct production studies, and moreover, the codes of this work have been written with a general formalism so that they can also be used in other studies for the production of further innovative medical radionuclides.

From the analysis of the three production routes

$$p + {}^{nat}\mathrm{Tb} \quad \rightarrow \quad {}^{155}\mathrm{Dy} + 5n \quad \rightarrow \quad {}^{155}\mathrm{Tb}, \tag{5.6}$$

$$d + {}^{nat}\mathrm{Tb} \quad \rightarrow \quad {}^{155}\mathrm{Dy} + 6n \quad \rightarrow \quad {}^{155}\mathrm{Tb}, \tag{5.7}$$

$$\alpha + {}^{nat}\mathrm{Gd} \quad \rightarrow \quad {}^{155}\mathrm{Dy} + xx \quad \rightarrow \quad {}^{155}\mathrm{Tb}. \tag{5.8}$$

conclusions can be drawn. In general all the three reactions are interesting for the indirect production of ^{155}Tb. The generator with protons, is the most promising one since it allows to achieve very high values of activity and purities, much better than those obtainable with standard production routes based on the use of enriched targets. Regarding the reaction with deuterons, this thesis shows for the first time the calculations of activities and purities and indicates quantitatively that is a very interesting route, but also that new experimental measurements are needed, in particular for ^{153}Dy, to better assess all the calculations. The reaction with α particles seems the least promising, but higher purities and activities can be obtained using enriched targets, obviously increasing the costs.

In conclusion this study has shown the possibility to use these generators to produce ^{155}Tb, in realistic scenarios, and that the indirect production via the ^{159}Tb(p, 5n) reaction is a significant improvement, both in terms of yield and purity, with respect to the other channels and to the low energy ^{155}Gd(p, n) direct production.

Appendix A

Schematic description of the decay graphs

I have developed two Python scripts to create graphs that represent the production and decay of nuclides specified by the user. The starting point is represented by the use of a recent nuclear database [117] (available at this webpage `https://www-nds.iaea.org/amdc/ame2020/nubase_4.mas20.txt`), whose structure is shown in Tab A1. The first script works on this database, mainly with *pandas* and *numpy* libraries, to generate a new file with the needed information, as represented in Tab. A2.

The second script is based on the *pandas, numpy, pygraphviz* libraries and allows to fulfill different tasks. It can be used to automatically:

- plot graphs of decay chains of desired nuclides, (therefore the children nuclei) but also the possible parent nuclides that decaying can naturally produce the specified nucleus (see Fig. A1–A2);
- combine the previous point with the output of the TALYS code (see Fig. A3).

The graphs are produced with a continuous search in the Tab. A2: the nuclide of interest is firstly searched in the "Nuclide" column retrieving the corresponding child, which in turn is searched in the first column, to complete the decay chain until a stable child is found. Similarly, to plot also all the progenitors of the nuclide of interest, initially the script looks for the nucleus in the "Child" column retrieving the corresponding parent (that is found in the first column), which in turn is searched in the "Child" column again, and so on.

Concerning the last point, in the energy range used in the TALYS calculations, only certain nuclides are produced depending on their energy thresholds and the code produces many different files in a single run. In particular, the file regarding the residual nuclei production cross sections are indicated as *rpZZZAAA.tot* for total and ground state cross section if no metastable state exists, or *rpZZZAAA.LMM* on the contrary where Z is the atomic number, A

the mass number and M is the number of the metastable state.

001	0000	1n	8071.3181	0.0004	609.8	s	0.6	1/2+*	06	1932	B-=100
001	0010	1H	7288.971064	0.000013	stbl			1/2+*	06	1920	IS=99.9855 78
002	0010	2H	13135.722895	0.000015	stbl			1+*	03	1932	IS=0.0145 78
003	0010	3H	14949.81090	0.00008	12.32	y	0.02	1/2+*	00	1934	B-=100
003	0020	3He	14931.21888	0.00006	stbl			1/2+*	98	1934	IS=0.0002 2
003	0030	3Li	28670#	2000#	p-unst			3/2-#	98		p ?
004	0010	4H	24620	100	139	ys	10	2-	98	1981	n=100

Table A1: Excerpt relative to the lightest nuclei of the nuclear database available at the webpage `https://www-nds.iaea.org/amdc/ame2020/nubase_4.mas20.txt`. The columns refer respectively to: the mass numer (AAA), the atomic number (ZZZi) specifying also the metastable states, the name of the isotope, the mass, its uncertainty, the half-life, its unit, its uncertainty, the spin and parity of the nuclide, the Evaluated Nuclear Structure Data File year, the year of the discovery, the decay mode with the branching ratio or the isotopic abundance. The # symbol indicates that the information is obtained from systematics.

Nuclide	T12	Lambda	Branch	Child	Thalf	Mode
1H	stable	0.0	99.9855	stable	stable	IS
2H	stable	0.0	0.0145	stable	stable	IS
3H	3.8852e+08	1.7840546192929202e-09	100	3He	12.32 y	β^-
4H	1.3900e-22	4.986670363740614e+21	100	3H	139.0 ys	n
5H	8.6000e-23	8.059850936743551e+21	100	3H	86.0 ys	2n
3He	stable	0.0	0.0002	stable	stable	IS
4He	stable	0.0	99.9998	stable	stable	IS

Table A2: Portion of the file obtained with the first python script that manipulates the database shown in the table above.

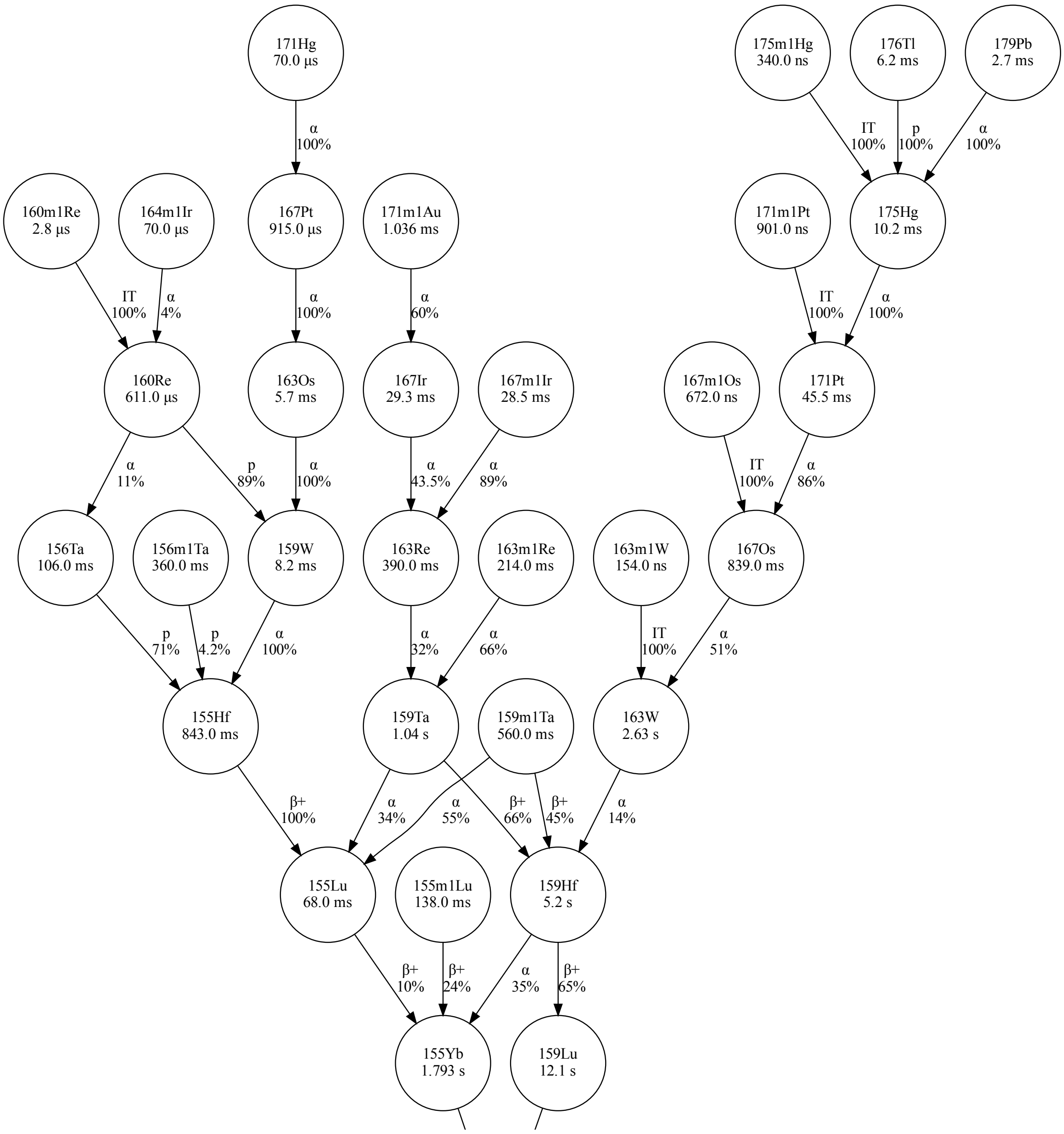

Figure A1: This picture shows the decay of ^{155}Dy (circled in red) and its production by the decay of other nuclei in nature (part 1). The plot is automatically created by the Python script.

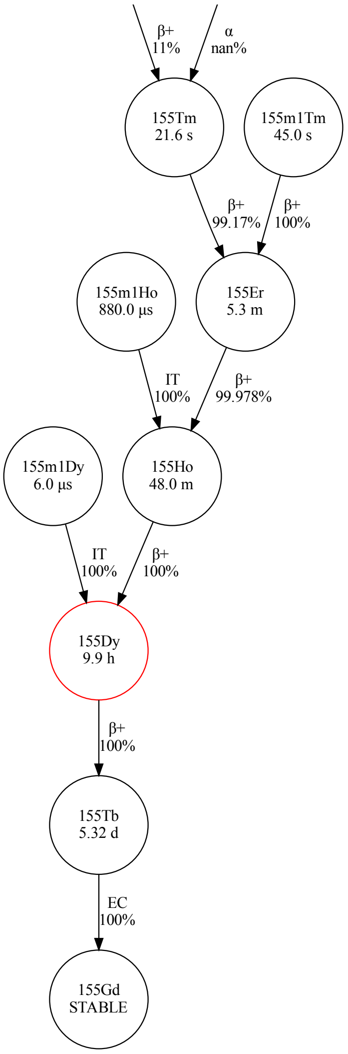

Figure A2: This picture shows the decay of ^{155}Dy (circled in red) and its production by the decay of other nuclei in nature (part 2, continued from Fig. A1). The plot is automatically created by the Python script.

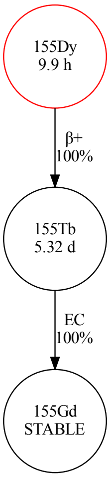

Figure A3: Production and decay chain of ^{155}Dy considering only the nuclei produced in the reaction with proton on ^{159}Tb. This graph is obtained combined the one of the previous figure with the output of the TALYS code.

The Python script reads the output of the code and creates the graphs verifying whether among the nuclides produced in the reaction there are parents of the specified nucleus. Therefore the final graphs represent not only the decay but also the production of specific nuclei in a given reaction. The second script allows also to obtain the matrix of the decay constants corresponding to a specific graph. For instance, the script generates automatically Fig. A3 and the following matrix:

$$\begin{pmatrix} -35640 & 0 & 0 \\ 1*35640 & -459650 & 0 \\ 1*35640 & 1*459650 & 0 \end{pmatrix} \tag{5.9}$$

that with symbols corresponds exactly to the matrix of the graph Fig. A3:

$$\begin{pmatrix} -\lambda_{155Dy} & 0 & 0 \\ +f_{155Dy\rightarrow 155Tb}\,\lambda_{155Dy} & -\lambda_{155Tb} & 0 \\ +f_{155Dy\rightarrow 155Tb}\,\lambda_{155Dy} & +f_{155Tb\rightarrow 155Gd}\,\lambda_{155Tb} & 0 \end{pmatrix} \tag{5.10}$$

The matrix is extremely useful for the calculations and solutions of the Bateman equations for the production and decay of the several nuclides produced in a given reaction.
Therefore the code allows to perform this tedious tasks automatically replacing the manual search of the needed information, easing and speeding up all the work.

Appendix B

In the following all the decay schemes of the different dysprosium nuclides (from ^{149}Dy to ^{164}Dy) produced in the considered reactions are shown. The plots have been obtained using the programs described in Appendix A.

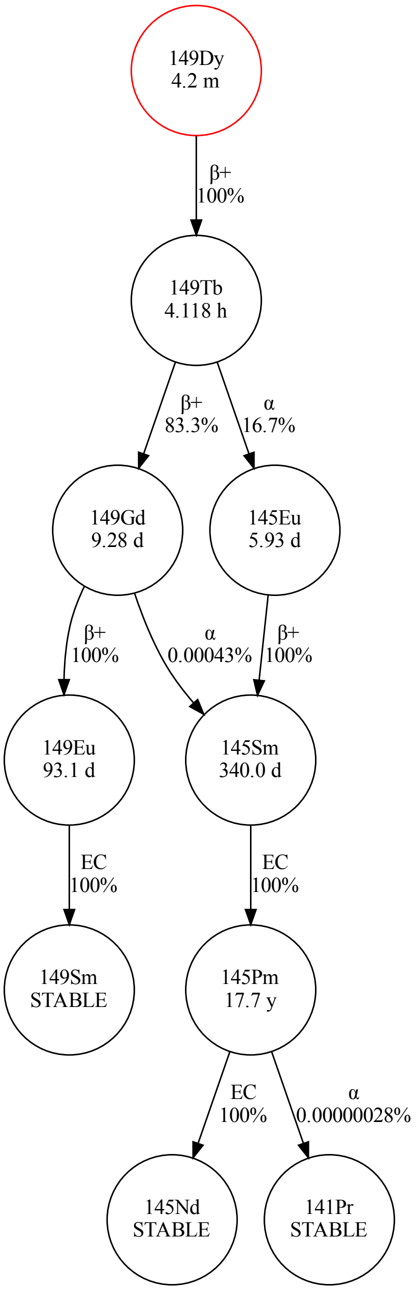
149Dy
4.2 m
β+
100%
149Tb
4.118 h
β+
83.3%
α
16.7%
149Gd
9.28 d
145Eu
5.93 d
β+
100%
α
0.00043%
β+
100%
149Eu
93.1 d
145Sm
340.0 d
EC
100%
EC
100%
149Sm
STABLE
145Pm
17.7 y
EC
100%
α
0.00000028%
145Nd
STABLE
141Pr
STABLE

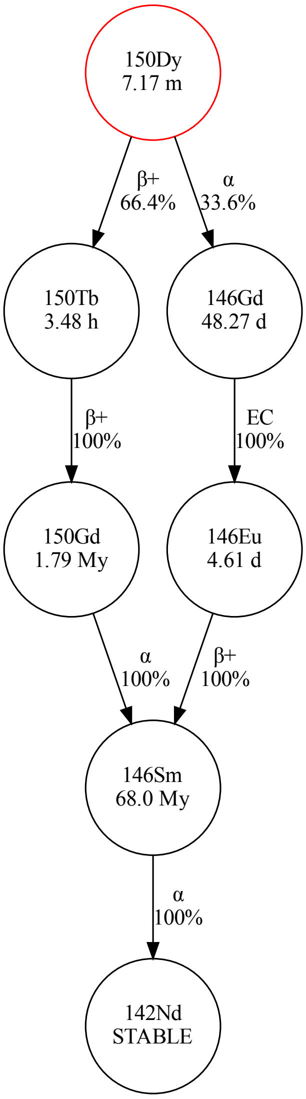
150Dy
7.17 m
β+
66.4%
α
33.6%
150Tb
3.48 h
146Gd
48.27 d
β+
100%
EC
100%
150Gd
1.79 My
146Eu
4.61 d
α
100%
β+
100%
146Sm
68.0 My
α
100%
142Nd
STABLE

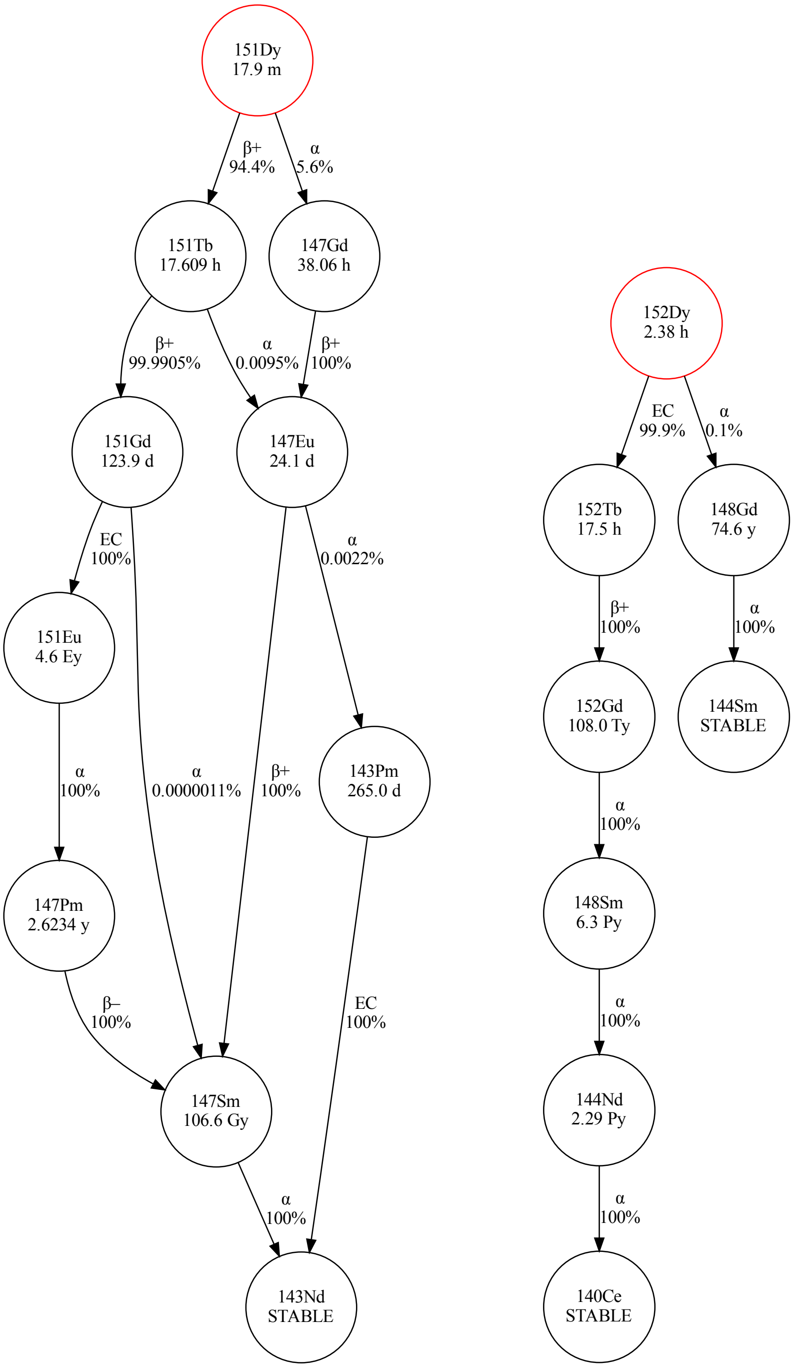
151Dy
17.9 m
β+
94.4%
α
5.6%
151Tb
17.609 h
147Gd
38.06 h
β+
99.9905%
α
0.0095%
β+
100%
151Gd
123.9 d
147Eu
24.1 d
EC
100%
α
0.0022%
151Eu
4.6 Ey
α
100%
α
0.0000011%
β+
100%
143Pm
265.0 d
147Pm
2.6234 y
β–
100%
EC
100%
147Sm
106.6 Gy
α
100%
143Nd
STABLE
152Dy
2.38 h
EC
99.9%
α
0.1%
152Tb
17.5 h
148Gd
74.6 y
β+
100%
α
100%
152Gd
108.0 Ty
144Sm
STABLE
α
100%
148Sm
6.3 Py
α
100%
144Nd
2.29 Py
α
100%
140Ce
STABLE

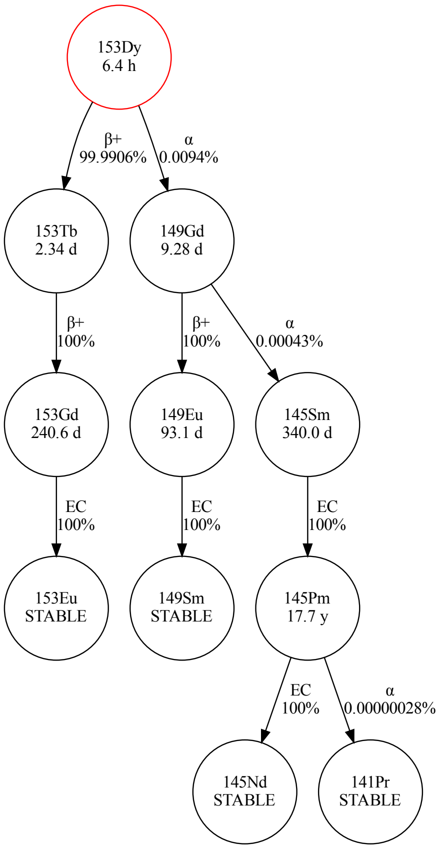
153Dy
6.4 h
β+
99.9906%
α
0.0094%
153Tb
2.34 d
149Gd
9.28 d
β+
100%
β+
100%
α
0.00043%
153Gd
240.6 d
149Eu
93.1 d
145Sm
340.0 d
EC
100%
EC
100%
EC
100%
153Eu
STABLE
149Sm
STABLE
145Pm
17.7 y
EC
100%
α
0.00000028%
145Nd
STABLE
141Pr
STABLE

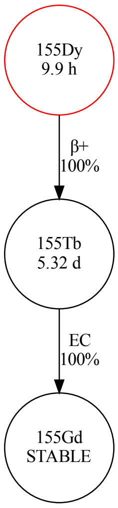
155Dy
9.9 h
β+
100%
155Tb
5.32 d
EC
100%
155Gd
STABLE

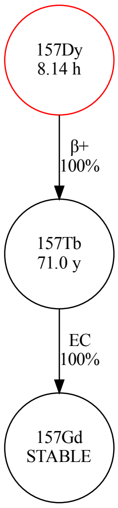
157Dy
8.14 h
β+
100%
157Tb
71.0 y
EC
100%
157Gd
STABLE

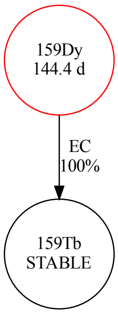
159Dy
144.4 d
EC
100%
159Tb
STABLE

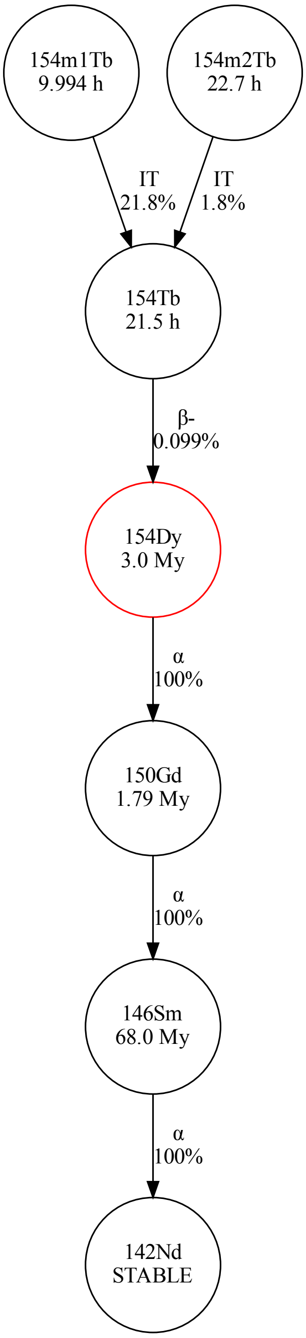
154m1Tb
9.994 h
154m2Tb
22.7 h
IT
21.8%
IT
1.8%
154Tb
21.5 h
β-
0.099%
154Dy
3.0 My
α
100%
150Gd
1.79 My
α
100%
146Sm
68.0 My
α
100%
142Nd
STABLE

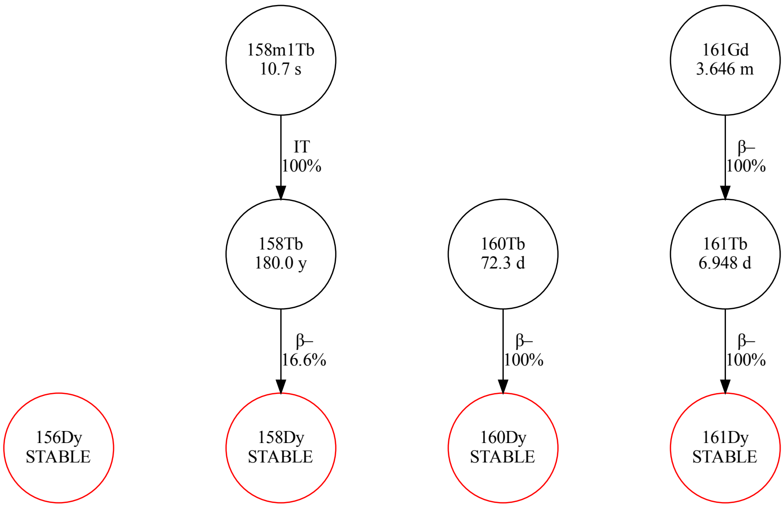
158m1Tb
10.7 s
IT
100%
158Tb
180.0 y
β–
16.6%
161Gd
3.646 m
β–
100%
160Tb
72.3 d
β–
100%
161Tb
6.948 d
β–
100%
156Dy
STABLE
158Dy
STABLE
160Dy
STABLE
161Dy
STABLE

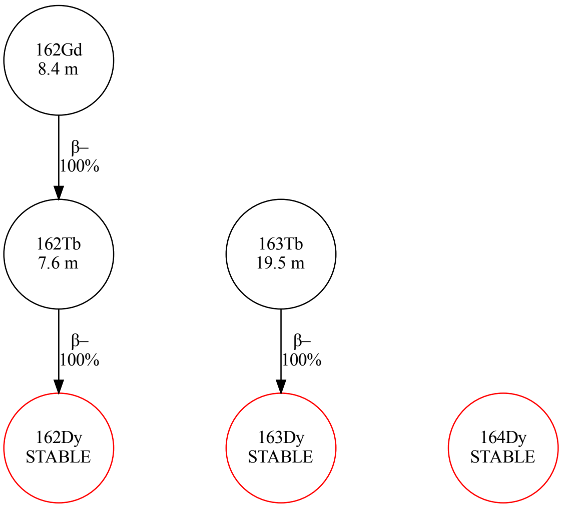
162Gd
8.4 m
β–
100%
162Tb
7.6 m
β–
100%
163Tb
19.5 m
β–
100%
162Dy
STABLE
163Dy
STABLE
164Dy
STABLE

Production of ^{161}Tb

As discussed in Chapter 3, also ^{161}Tb has been considered, since it can be produced with the reaction $\alpha{+}^{nat}Gd$. The cross section of the terbium nuclides have been re-scaled considering the reaction with an enriched target: $\alpha +^{160} Gd$. From the study of the cross section, the energy window 20–40 MeV is interesting to be explored since the production of ^{161}Tb is higher than the one of ^{160}Tb, its main contaminant, as shown in the following figures.

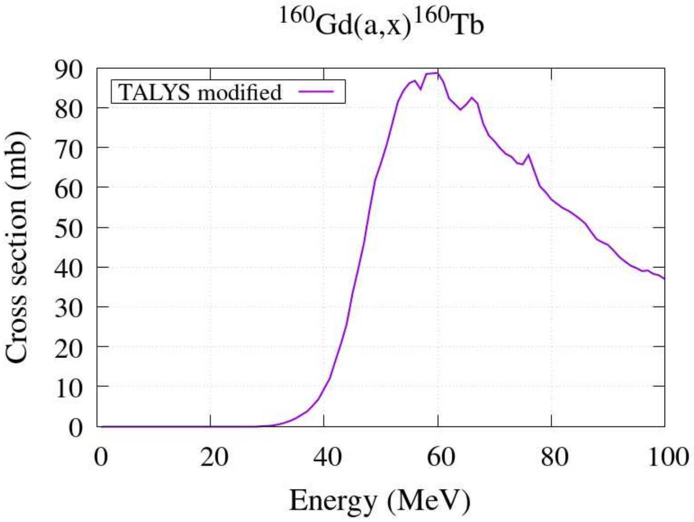

Figure B.1: Cross section of ^{160}Tb from the $\alpha +^{160} Gd$ reaction.

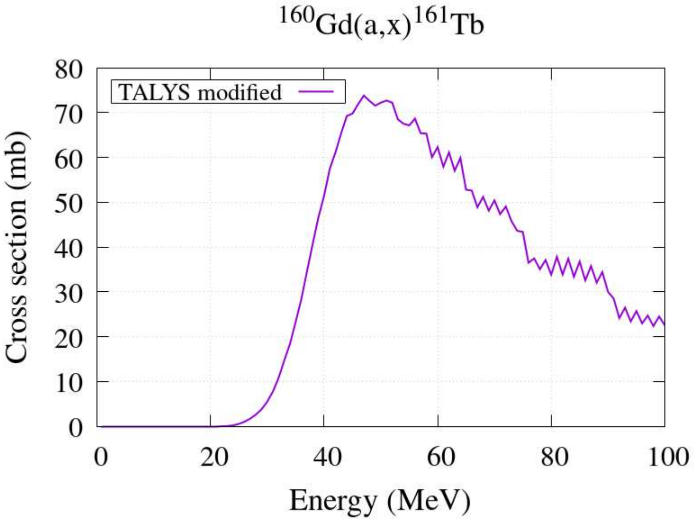

Figure B.2: Cross section of ^{161}Tb from the $\alpha +^{160} Gd$ reaction.

Variable	range	step
E_{in} and E_{out}	20 MeV → 40 MeV	1 MeV
T_{irrad}	0.5 h → 10 h	1 h
Δt_1	0.5 h → 100 h	1 h

Table B.1: Ranges of the variables that have been chosen for the calculations of the activities and purities, as presented in Chapter 4.

Moreover, this route allows also to exhibit the use of the innovative technique for the simultaneous maximization of A and IP in a direct production of a medical radionuclides. Therefore the same procedure described in Chapter 4 has been used also here.

In Tab. B.1 the ranges of the variables used in the calculations are shown. The following figure includes the results of all the calculations and the values of the three solutions are reported in the next table. Unfortunately, it seems that this route is actually not so promising for the production of ^{161}Tb, even if it is more favourable than other routes, like the ones with deuterons on natural dysprosium [138] or with deuterons on ^{160}Gd [123], because from the case of maximum activity the corresponding integral physical yields can be calculated: 0.09 MBq/μAh or 25 MBq/C.

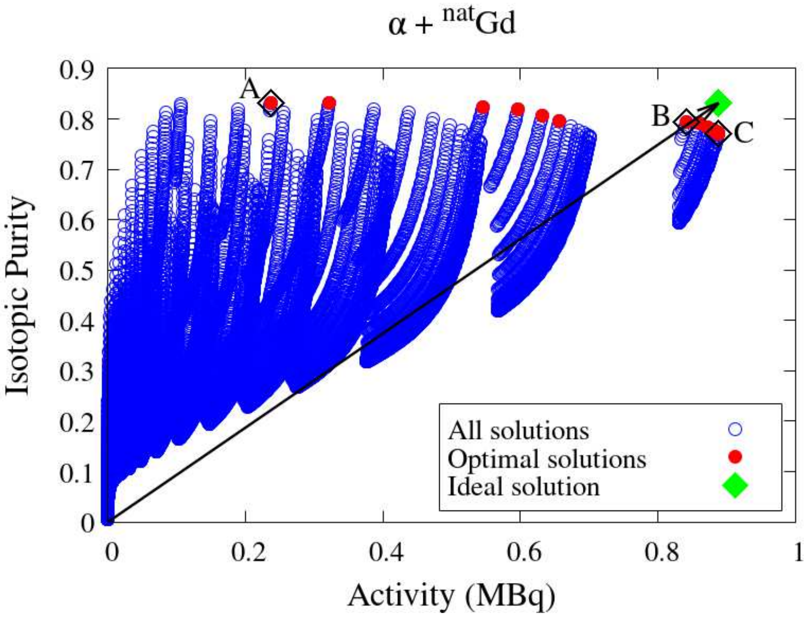

Figure B.3: Solutions of the calculations for the optimal production of ^{161}Tb from the $\alpha +^{160} Gd$ reaction, where for simplicity t_{irrad} has been fixed to 10 h.

case	E_{in} (MeV)	E_{out} (MeV)	t_{irrad} (h)	Δt_1 (h)	A (MBq)	IP	RNP	SA (MBq/g)	Δx (mm)
A	37	35	10	5	0.24	0.83	0.99	3.6×10^9	0.03
B	39	30	10	5	0.84	0.79	0.99	3.43×10^9	0.13
C	39	20	10	4.5	0.89	0.77	0.99	3.33×10^9	0.25

Table B.2: Values of the variables and of the functions for the four case represented in the previous figure, moving from left to right, for descending IP values. The thickness of the target has been calculated using the ATIMA web tool (https://web-docs.gsi.de/ weick/atima/).

Bibliography

[1] R. Capote *et al.*, "IAEA coordinated research project on nuclear data for charged-particle monitor reactions and medical isotope production," in *EPJ Web of Conferences*, vol. 146, p. 08007, EDP Sciences, 2017.

[2] K. Herrmann *et al.*, "Joint EANM, SNMMI and IAEA enabling guide: how to set up a theranostics centre," *European Journal of Nuclear Medicine and Molecular Imaging*, vol. 49, no. 7, pp. 2300–2309, 2022.

[3] S. M. Qaim, "Medical radionuclide production," in *Medical Radionuclide Production*, De Gruyter, 2019.

[4] D. Schardt, T. Elsässer, and D. Schulz-Ertner, "Heavy-ion tumor therapy: Physical and radiobiological benefits," *Reviews of modern physics*, vol. 82, no. 1, p. 383, 2010.

[5] S. M. Qaim, B. Scholten, and B. Neumaier, "New developments in the production of theranostic pairs of radionuclides," *Journal of Radioanalytical and Nuclear Chemistry*, vol. 318, pp. 1493–1509, 2018.

[6] N. Naskar and S. Lahiri, "Theranostic terbium radioisotopes: challenges in production for clinical application," *Frontiers in medicine*, vol. 8, p. 675014, 2021.

[7] "Terbium: a new "swiss army knife" for nuclear medicine," *CERN Courier*, pp. 10–11, 2013. Available online at https://cerncourier.com/a/terbium-a-new-swiss-army-knife-for-nuclear-medicine/.

[8] C. Müller *et al.*, "A unique matched quadruplet of terbium radioisotopes for PET and SPECT and for α-and β–radionuclide therapy: an in vivo proof-of-concept study with a new receptor-targeted folate derivative," *Journal of nuclear medicine*, vol. 53, no. 12, pp. 1951–1959, 2012.

[9] "NuDat3.0." `https://www.nndc.bnl.gov/nudat3/`.

[10] C. Müller *et al.*, "Scandium and terbium radionuclides for radiotheranostics: current state of development towards clinical application," *The British journal of radiology*, vol. 91, no. 1091, p. 20180074, 2018.

[11] S. K. Imam, "Advancements in cancer therapy with alpha-emitters: a review," *International Journal of Radiation Oncology* Biology* Physics*, vol. 51, no. 1, pp. 271–278, 2001.

[12] C. Müller *et al.*, "Alpha-PET with terbium-149: evidence and perspectives for radiotheragnostics," *EJNMMI radiopharmacy and chemistry*, vol. 1, no. 1, pp. 1–5, 2017.

[13] C. Müller *et al.*, "Preclinical in vivo application of ^{152}Tb-DOTANOC: a radiolanthanide for PET imaging," *EJNMMI research*, vol. 6, no. 1, pp. 1–10, 2016.

[14] C. Müller *et al.*, "Preclinical investigations and first-in-human application of ^{152}Tb-PSMA-617 for PET/CT imaging of prostate cancer," *EJNMMI research*, vol. 9, no. 1, pp. 1–10, 2019.

[15] D. Filosofov, E. Kurakina, and V. Radchenko, "Potent candidates for Targeted Auger Therapy: Production and radiochemical considerations," *Nuclear Medicine and Biology*, vol. 94, pp. 1–19, 2021.

[16] R. P. Baum *et al.*, "First-in-humans application of ^{161}Tb: A feasibility study using ^{161}Tb-DOTATOC," *Journal of Nuclear Medicine*, vol. 62, no. 10, pp. 1391–1397, 2021.

[17] A. Walter *et al.*, "Correlated multimodal imaging in life sciences: expanding the biomedical horizon," *Frontiers in Physics*, p. 47, 2020.

[18] P. P. Bruyant, "Analytic and Iterative Reconstruction Algorithms in SPECT," *Journal of Nuclear Medicine*, vol. 43, no. 10, pp. 1343–1358, 2002.

[19] S. R. Cherry *et al.*, *Physics in nuclear medicine*, vol. 3. Soc Nuclear Med, 2003.

[20] C. Müller *et al.*, "Future prospects for SPECT imaging using the radiolanthanide terbium-155—production and preclinical evaluation in tumor-bearing mice," *Nuclear medicine and biology*, vol. 41, pp. e58–e65, 2014.

[21] S. Carlson, "A glance at the history of nuclear medicine," *Acta oncologica*, vol. 34, no. 8, pp. 1095–1102, 1995.

[22] J. G. Hamilton and M. H. Soley, "Studies in iodine metabolism of the thyroid gland in situ by the use of radio-iodine in normal subjects and in

patients with various types of goiter," *American Journal of Physiology-Legacy Content*, vol. 131, no. 1, pp. 135–143, 1940.

[23] T. Van den Wyngaert *et al.*, "SPECT/CT: standing on the shoulders of giants, it is time to reach for the sky!," *Journal of Nuclear Medicine*, vol. 61, no. 9, pp. 1284–1291, 2020.

[24] N. A. Gharibkandi *et al.*, "Nanostructures as radionuclide carriers in auger electron therapy," *Materials*, vol. 15, no. 3, p. 1143, 2022.

[25] A. Ku *et al.*, "Auger electrons for cancer therapy–a review," *EJNMMI radiopharmacy and chemistry*, vol. 4, no. 1, pp. 1–36, 2019.

[26] M. Parsi *et al.*, "PSMA: A game changer in the diagnosis and treatment of advanced prostate cancer," *Medical Oncology*, vol. 38, pp. 1–20, 2021.

[27] N. Daems *et al.*, "Gold nanoparticles meet medical radionuclides," *Nuclear Medicine and Biology*, vol. 100, pp. 61–90, 2021.

[28] "ISOLPHARM website." `https://isolpharm.pd.infn.it/web/?page_id=967`.

[29] J. Esposito *et al.*, "LARAMED: a laboratory for radioisotopes of medical interest," *Molecules*, vol. 24, no. 1, p. 20, 2018.

[30] Z. Talip *et al.*, "A step-by-step guide for the novel radiometal production for medical applications: Case studies with ^{68}Ga, ^{44}Sc, ^{177}Lu and ^{161}Tb," *Molecules*, vol. 25, no. 4, p. 966, 2020.

[31] C. Duchemin *et al.*, "CERN-MEDICIS: a unique facility for the production of non-conventional radionuclides for the medical research," *JACoW IPAC*, vol. 2020, no. CERN-ACC-2021-010, p. THVIR13, 2021.

[32] P. V. Grundler *et al.*, "The metamorphosis of radionuclide production and development at Paul Scherrer Institute," *Chimia*, vol. 74, no. 12, pp. 968–975, 2020.

[33] N. P. van der Meulen, "The Use of PSI's High Intensity Proton Accelerator (HIPA) Complex Towards Medical-Radionuclide Development," tech. rep., 2022.

[34] C. Magni, *Scuola di Dottorato di Ricerca in Fisica.* PhD thesis, University of Pavia.

[35] S. Cisternino *et al.*, "Upgrade of the HIVIPP Deposition Apparatus for Nuclear Physics Thin Targets Manufacturing," *Instruments*, vol. 6, no. 3, p. 23, 2022.

[36] "EXFOR database website." `https://www-nds.iaea.org/exfor/`.

[37] "IAEA Data Explorer." `https://nds.iaea.org/dataexplorer`.

[38] E. Lebowitz and M. Greene, "The production of ^{157}Dy for medical use," *The International journal of applied radiation and isotopes*, vol. 22, no. 12, pp. 789–793, 1971.

[39] H. Hassan *et al.*, "Proton induced reactions on ^{159}Tb and ^{139}La for producing ^{159}Dy and ^{139}Ce," 2008.

[40] G. F. Steyn *et al.*, "Cross sections of proton-induced reactions on ^{152}Gd, ^{155}Gd and ^{159}Tb with emphasis on the production of selected Tb radionuclides," *Nuclear Instruments and Methods in Physics Research Section B: Beam Interactions with Materials and Atoms*, vol. 319, pp. 128–140, 2014.

[41] J. W. Engle *et al.*, "Nuclear excitation functions from 40 to 200 mev proton irradiation of terbium," *Nuclear Instruments and Methods in Physics Research Section B: Beam Interactions with Materials and Atoms*, vol. 366, pp. 206–216, 2016.

[42] F. Tárkányi *et al.*, "Activation cross-sections of longer lived radioisotopes of proton induced nuclear reactions on terbium up to 65 MeV," *Applied Radiation and Isotopes*, vol. 127, pp. 7–15, 2017.

[43] F. Tárkányi *et al.*, "Activation cross-sections of longer-lived radioisotopes of deuteron induced nuclear reactions on terbium up to 50 MeV," *Nuclear Instruments and Methods in Physics Research Section B: Beam Interactions with Materials and Atoms*, vol. 316, pp. 183–191, 2013.

[44] T. Duc, J. Tousset, and M. Perrin, "Excitation function of reactions induced on terbium by 26.9 MeV deuterons," *C. R. Ser. B Phys.*, vol. 266, p. 100 – 102, 1968. Cited by: 3.

[45] L. N. SNTL and S. Nassiff, "Excitation Functions for ^{159}Tb(d, p)^{160}Tb and ^{159}Tb(d, 4n)^{157}Dy Reactions," *Radiochimica Acta*, vol. 14, no. 3-4, pp. 159–160, 1970.

[46] D. Ichinkhorloo *et al.*, "Activation cross sections of dysprosium-157,159 and terbium-160 radioisotopes from the deuteron-induced reactions on terbium-159 up to 24 MeV," *Nuclear Instruments and Methods in Physics Research Section B: Beam Interactions with Materials and Atoms*, vol. 461, pp. 102–104, 2019.

[47] M. Thakur and S. Waters, "Production and separation of cyclotron produced dysprosium-157," *Journal of Inorganic and Nuclear Chemistry*, vol. 35, no. 6, pp. 1787–1791, 1973.

[48] R. Gayoso, A. Sonzogni, and S. Nassiff, "(α, pxn) reactions on natural gadolinium," *Radiochimica Acta*, vol. 72, no. 2, pp. 55–60, 1996.

[49] D. Ichinkhorloo *et al.*, "Production cross sections of dysprosium, terbium and gadolinium radioisotopes from the alpha-particle-induced reactions on natural gadolinium up to 50 MeV," *Nuclear Instruments and Methods in Physics Research Section B: Beam Interactions with Materials and Atoms*, vol. 499, pp. 46–52, 2021.

[50] A. N. Moiseeva *et al.*, "New method for production of ^{155}Tb via ^{155}Dy by irradiation of ^{nat}Gd by medium energy alpha particles," *Nuclear Medicine and Biology*, vol. 106, pp. 52–61, 2022.

[51] A. J. Koning, S. Hilaire, and M. C. Duijvestijn, "Talys-1.0," in *International Conference on Nuclear Data for Science and Technology*, pp. 211–214, EDP Sciences, 2007.

[52] C. A. Bertulani, "Nuclear reactions," *arXiv preprint arXiv:0908.3275*, 2009.

[53] K. S. Krane, *Introductory nuclear physics.* John Wiley & Sons, 1991.

[54] C. Bertulani and P. Danielewicz, *Introduction to nuclear reactions.* CRC Press, 2021.

[55] G. R. Satchler, "Direct nuclear reactions," 1983.

[56] A. Koning, S. Hilaire, and S. Goriely, "Talys: modeling of nuclear reactions," *The European Physical Journal A*, vol. 59, no. 6, p. 131, 2023.

[57] G. R. Satchler and G. Satchler, *Introduction to nuclear reactions.* Springer, 1990.

[58] N. Bohr, "Neutron capture and nuclear constitution," *Uspekhi Fizicheskikh Nauk*, vol. 16, no. 4, pp. 425–435, 1936.

[59] S. N. Ghoshal, "An experimental verification of the theory of compound nucleus," *Physical Review*, vol. 80, no. 6, p. 939, 1950.

[60] W. Hauser and H. Feshbach, "The inelastic scattering of neutrons," *Physical review*, vol. 87, no. 2, p. 366, 1952.

[61] L. Canton and A. Fontana, "Nuclear physics applied to the production of innovative radiopharmaceuticals," *The European Physical Journal Plus*, vol. 135, no. 9, p. 770, 2020.

[62] S. Hilaire, "TALYS: A tool to go from theoretical modeling of nuclear reactions to evaluations," *CEA, DAM, DIF F-91297 Arpajon, France*, 2014.

[63] E. Gadioli and P. E. Hodgson, *Pre-equilibrium nuclear reactions.* No. 15, Oxford University Press on Demand, 1992.

[64] C. Cline and M. Blann, “The pre-equilibrium statistical model: description of the nuclear equilibration process and parameterization of the model,” *Nuclear Physics A*, vol. 172, no. 2, pp. 225–259, 1971.

[65] C. K. Cline, “Extensions to the pre-equilibrium statistical model and a study of complex particle emission,” *Nuclear Physics A*, vol. 193, no. 2, pp. 417–437, 1972.

[66] A. Koning and J. Delaroche, “Local and global nucleon optical models from 1 keV to 200 MeV,” *Nuclear Physics A*, vol. 713, no. 3-4, pp. 231–310, 2003.

[67] J. P. Jeukenne, A. Lejeune, and C. Mahaux, “Optical-model potential in nuclear matter from Reid’s hard core interaction,” *Physical Review C*, vol. 10, no. 4, p. 1391, 1974.

[68] J. P. Jeukenne, A. Lejeune, and C. Mahaux, “Optical-model potential in finite nuclei from Reid’s hard core interaction,” *Physical Review C*, vol. 16, no. 1, p. 80, 1977.

[69] J.-P. Jeukenne, A. Lejeune, and C. Mahaux, “Microscopic calculation of the symmetry and Coulomb components of the complex optical-model potential,” *Physical Review C*, vol. 15, no. 1, p. 10, 1977.

[70] S. Watanabe, “High energy scattering of deuterons by complex nuclei,” *Nuclear Physics*, vol. 8, pp. 484–492, 1958.

[71] W. W. Daehnick, J. D. Childs, and Z. Vrcelj, “Global optical model potential for elastic deuteron scattering from 12 to 90 MeV,” *Physical Review C*, vol. 21, no. 6, p. 2253, 1980.

[72] L. McFadden and G. R. Satchler, “Optical-model analysis of the scattering of 24.7 MeV alpha particles,” *Nuclear Physics*, vol. 84, no. 1, pp. 177–200, 1966.

[73] J. Bojowald *et al.*, “Elastic deuteron scattering and optical model parameters at energies up to 100 MeV,” *Physical Review C*, vol. 38, no. 3, p. 1153, 1988.

[74] P. Demetriou, C. Grama, and S. Goriely, “Improved global α-optical model potentials at low energies,” *Nuclear Physics A*, vol. 707, no. 1-2, pp. 253–276, 2002.

[75] Y. Han, Y. Shi, and Q. Shen, “Deuteron global optical model potential for energies up to 200 MeV,” *Physical Review C*, vol. 74, no. 4, p. 044615, 2006.

[76] H. An and C. Cai, "Global deuteron optical model potential for the energy range up to 183 MeV," *Physical Review C*, vol. 73, no. 5, p. 054605, 2006.

[77] V. Avrigeanu, M. Avrigeanu, and C. Mănăilescu, "Further explorations of the α-particle optical model potential at low energies for the mass range A$\simeq$ 45–209," *Physical Review C*, vol. 90, no. 4, p. 044612, 2014.

[78] M. Nolte, H. Machner, and J. Bojowald, "Global optical potential for α particles with energies above 80 MeV," *Physical Review C*, vol. 36, no. 4, p. 1312, 1987.

[79] V. Avrigeanu, P. E. Hodgson, and M. Avrigeanu, "Global optical potentials for emitted alpha particles," *Physical Review C*, vol. 49, no. 4, p. 2136, 1994.

[80] A. J. Koning *et al.*, "TENDL: complete nuclear data library for innovative nuclear science and technology," *Nuclear Data Sheets*, vol. 155, pp. 1–55, 2019.

[81] J. Raynal, "Notes on ECIS94," *CEA Saclay report CEA-N-2772*, 1994.

[82] J. Raynal, "ECIS-06, Coupled Channel, Statistical Model, Schroedinger and Dirac Equation, Dispersion Relation," 2007.

[83] M. B. Fox *et al.*, "Investigating high-energy proton-induced reactions on spherical nuclei: Implications for the preequilibrium exciton model," *Physical Review C*, vol. 103, no. 3, p. 034601, 2021.

[84] J. Dobeš and E. Běták, "Two-component exciton model," *Zeitschrift für Physik A Atoms and Nuclei*, vol. 310, no. 4, pp. 329–338, 1983.

[85] "Geometry Dependent Hybrid model website."

[86] M. Blann, "Importance of the nuclear density distribution on preequilibrium decay," *Physical Review Letters*, vol. 28, no. 12, p. 757, 1972.

[87] M. Blann and H. Vonach, "Global test of modified precompound decay models," *Physical Review C*, vol. 28, no. 4, p. 1475, 1983.

[88] M. Blann, "New precompound decay model," *Physical Review C*, vol. 54, no. 3, p. 1341, 1996.

[89] M. Blann, "ALICE-91: Statistical model code system with fission competition," *RSIC code package PSR-146*, 1991.

[90] A. Y. Konobeyev *et al.*, "Implementation of the geometry dependent hybrid model in talys," *J. Korean Phys. Soc*, vol. 59, p. 935, 2011.

[91] M. Blann and J. Bisplinghoff, “ALICE/LIVERMORE82. Precompound Compound Decay,” tech. rep., Lawrence Livermore National Lab.(LLNL), Livermore, CA (United States), 1982.

[92] J. R. Oppenheimer, “The disintegration of the deuteron by impact,” *Physical Review*, vol. 47, no. 11, p. 845, 1935.

[93] S. Dancoff, “Disintegration of the deuteron in flight,” *Physical Review*, vol. 72, no. 11, p. 1017, 1947.

[94] R. Serber, “The production of high energy neutrons by stripping,” *Physical Review*, vol. 72, no. 11, p. 1008, 1947.

[95] R. J. Glauber, “Deuteron stripping processes at high energies,” *Phys. Rev.*, vol. 99, p. 1515, 1955.

[96] C. Kalbach, “Preequilibrium reactions with complex particle channels,” *Physical Review C*, vol. 71, no. 3, p. 034606, 2005.

[97] M. Avrigeanu and V. Avrigeanu, “Deuteron breakup effects on activation cross sections at low and medium energies,” in *Journal of Physics: Conference Series*, vol. 205, p. 012014, IOP Publishing, 2010.

[98] M. Avrigeanu and V. Avrigeanu, “Role of breakup and direct processes in deuteron-induced reactions at low energies,” *Physical Review C*, vol. 92, no. 2, p. 021601, 2015.

[99] M. Avrigeanu and V. Avrigeanu, “Additive empirical parametrization and microscopic study of deuteron breakup,” *Physical Review C*, vol. 95, no. 2, p. 024607, 2017.

[100] R. Capote *et al.*, “RIPL–reference input parameter library for calculation of nuclear reactions and nuclear data evaluations,” *Nuclear Data Sheets*, vol. 110, no. 12, pp. 3107–3214, 2009.

[101] A. Colombi *et al.*, “Improvement of nuclear reaction modeling for the production of ^{47}Sc on natural vanadium targets for medical applications,” in *EPJ Web of Conferences*, vol. 261, p. 05008, EDP Sciences, 2022.

[102] F. Barbaro *et al.*, “New results on proton-induced reactions on vanadium for ^{47}Sc production and the impact of level densities on theoretical cross sections,” *Physical Review C*, vol. 104, no. 4, p. 044619, 2021.

[103] Los Alamos Monte Carlo Group, *MCNP: A General Monte Carlo Code for Neutron and Photon Transport.* Los Alamos National Laboratory, 1981.

[104] A. Ferrari *et al.*, *FLUKA: A multi-particle transport code (Program version 2005).* No. CERN-2005-10, Cern, 2005.

[105] S. Agostinelli *et al.*, "GEANT4—a simulation toolkit," *Nuclear instruments and methods in physics research section A: Accelerators, Spectrometers, Detectors and Associated Equipment*, vol. 506, no. 3, pp. 250–303, 2003.

[106] T. Sato *et al.*, "Features of particle and heavy ion transport code system (PHITS) version 3.02," *Journal of Nuclear Science and Technology*, vol. 55, no. 6, pp. 684–690, 2018.

[107] A. Boudard *et al.*, "New potentialities of the Liège intranuclear cascade model for reactions induced by nucleons and light charged particles," *Physical Review C*, vol. 87, no. 1, p. 014606, 2013.

[108] S. Furihata, "Statistical analysis of light fragment production from medium energy proton-induced reactions," *Nuclear Instruments and Methods in Physics Research Section B: Beam Interactions with Materials and Atoms*, vol. 171, no. 3, pp. 251–258, 2000.

[109] S. Furihata, "The GEM code-The Generalized Evaporation Model and the fission model," in *Advanced Monte Carlo for Radiation Physics, Particle Transport Simulation and Applications: Proceedings of the Monte Carlo 2000 Conference, Lisbon, 23–26 October 2000*, pp. 1045–1050, Springer, 2001.

[110] T. Hayakawa, Y. Hatsukawa, and T. Tanimori, "^{95g}Tc and ^{96g}Tc as alternatives to medical radioisotope ^{99m}Tc," *Heliyon*, vol. 4, no. 1, 2018.

[111] K. Tsukada *et al.*, "Anomalous radioisotope production for ^{68}ZnO using polyethylene by accelerator neutrons," *journal of the physical society of japan*, vol. 89, no. 3, p. 034201, 2020.

[112] B. S. Rattyananda *et al.*, "Computation Study of Radioisotopes Gallium-68 (^{68}Ga) Production using Long-lived & High Activity methods," *Jurnal Sains dan Teknologi Nuklir Indonesia (Indonesian Journal of Nuclear Science and Technology)*, vol. 22, no. 2, 2022.

[113] Y. Nagai, "Production scheme for diagnostic-therapeutic radioisotopes by accelerator neutrons," *Proceedings of the Japan Academy, Series B*, vol. 97, no. 6, pp. 292–323, 2021.

[114] W. R. Leo, *Techniques for nuclear and particle physics experiments: a how-to approach.* Springer Science & Business Media, 2012.

[115] H. Bateman, "The solution of a system of differential equations occurring in the theory of radioactive transformations," in *Proc. Cambridge Philos. Soc.*, vol. 15, pp. 423–427, 1910.

[116] L. Moral and A. F. Pacheco, “Algebraic approach to the radioactive decay equations,” *American Journal of Physics*, vol. 71, no. 7, pp. 684–686, 2003.

[117] F. G. Kondev *et al.*, “The NUBASE2020 evaluation of nuclear physics properties ,” *Chinese Physics C*, vol. 45, p. 030001, mar 2021.

[118] N. Otuka and S. Takács, “Definitions of radioisotope thick target yields,” *Radiochimica Acta*, vol. 103, no. 1, pp. 1–6, 2015.

[119] EANM, “EANM 2019 Radiopharmacy: An Update. Published by European Association of Nuclear Medicine.” `https://www.eanm.org/publications/technologists-guide`, 2019.

[120] E. Alhassan *et al.*, “In search of the best nuclear data file for proton induced reactions: varying both models and their parameters,” in *EPJ Web of Conferences*, vol. 239, p. 13005, EDP Sciences, 2020.

[121] A. J. Koning, “Bayesian Monte Carlo method for nuclear data evaluation,” *The European Physical Journal A*, vol. 51, pp. 1–16, 2015.

[122] P. R. Bevington *et al.*, *Data reduction and error analysis for the physical sciences.* McGraw-Hill, 1992.

[123] E. Nigron *et al.*, “Can we reach suitable ^{161}Tb purity for medical applications using the ^{160}Gd(d, n) reaction?,” *Applied Radiation and Isotopes*, p. 110927, 2023.

[124] A. Jahan, K. L. Edwards, and M. Bahraminasab, *Multi-criteria decision analysis for supporting the selection of engineering materials in product design.* Butterworth-Heinemann, 2016.

[125] S. Nayak, *Fundamentals of optimization techniques with algorithms.* Academic Press, 2020.

[126] P. A. Vikhar, “Evolutionary algorithms: A critical review and its future prospects,” in *2016 International conference on global trends in signal processing, information computing and communication (ICGTSPICC)*, pp. 261–265, IEEE, 2016.

[127] A. Navon *et al.*, “Learning the pareto front with hypernetworks,” *arXiv preprint arXiv:2010.04104*, 2020.

[128] J. J. M. De Goeij and M. L. Bonardi, “How do we define the concepts specific activity, radioactive concentration, carrier, carrier-free and no-carrier-added?,” *Journal of radioanalytical and nuclear chemistry*, vol. 263, no. 1, pp. 13–18, 2005.

[129] G. Dellepiane *et al.*, "Cross section measurement of terbium radioisotopes for an optimized ^{155}Tb production with an 18 MeV medical PET cyclotron," *Applied radiation and isotopes*, vol. 184, p. 110175, 2022.

[130] "Medical Isotope Browser." `https://www-nds.iaea.org/relnsd/isotopia/isotopia.html`.

[131] J. W. Engle *et al.*, "Recommended nuclear data for the production of selected therapeutic radionuclides," *Nuclear Data Sheets*, vol. 155, pp. 56–74, 2019.

[132] A. J. Koning *et al.*, *Trends in Radiopharmaceuticals (ISTR-2019).* Proceedings Series, Vienna: INTERNATIONAL ATOMIC ENERGY AGENCY, 2020.

[133] C. Favaretto *et al.*, "Cyclotron production and radiochemical purification of terbium-155 for SPECT imaging," *EJNMMI Radiopharmacy and Chemistry*, vol. 6, no. 1, pp. 1–17, 2021.

[134] S. M. Qaim, I. Spahn, B. Scholten, and B. Neumaier, "Uses of alpha particles, especially in nuclear reaction studies and medical radionuclide production," *Radiochimica acta*, vol. 104, no. 9, pp. 601–624, 2016.

[135] M. Ferrari *et al.*, "SPECT/CT radiation dosimetry," *Clinical and Translational Imaging*, vol. 2, pp. 557–569, 2014.

[136] C. Marcassa *et al.*, "Temporal evolution of administered activity in cardiac gated SPECT and patients' effective dose: analysis of an historical series," *European journal of nuclear medicine and molecular imaging*, vol. 40, pp. 325–330, 2013.

[137] M. Brucer, "William Duane and the radium cow: an American contribution to an emerging atomic age," *Med Phys*, vol. 20, Nov-Dec 1993.

[138] M. Colucci *et al.*, "Excitation functions of deuteron induced nuclear reactions on dysprosium targets for the production of the theranostic relevant isotopes of terbium," *The European Physical Journal Plus*, vol. 137, no. 10, p. 1180, 2022.

Ringraziamenti

I want to thank Dr. Lembit Sihver and Dr. Vincenzo Patera, who were the referees of my thesis, for their contribution and for the time they spent in reading and evaluating this work.

Ringrazio il Dr. Andrea Fontana per il suo prezioso aiuto e per la sua costante guida che mi ha accompagnato in tutti questi anni, fin dalla Laurea Triennale.

Ringrazio la Professoressa Francesca Ballarini e il Dr. Mario Pietro Carante per la loro disponibilità e per l'aiuto quando c'è stato bisogno.

Ringrazio tutti i colleghi che ho conosciuto in questi anni: ognuno a modo suo mi ha insegnato qualcosa. Farò certamente tesoro di quanto ho appreso.

Ringrazio tutti i miei amici per i bei momenti trascorsi assieme: siete stati un prezioso aiuto per distogliere la mente dallo studio e dal lavoro e godere degli attimi divertenti della vita.

Tra le persone che hanno fatto parte della mia vita voglio ringraziare chi non c'è più, nonno Delio e nonna Teresa. Voglio riassumere le tante cose "non dette" che mi avete insegnato con la frase che Albus Silente dice ad Harry (in Harry Potter e i Doni della Morte): *"Non provare pietà per i morti, Harry. Prova pietà per i vivi e soprattutto per coloro che vivono senza amore."*.

Ringrazio la mia famiglia che mi è stata vicino, sempre. Con questo si conclude un lungo percorso, durante il quale la vita ci ha riservato tante sorprese. Questi ultimi anni sono stati difficili e sofferti e sono grato di tutto il supporto che mi avete dato. Grazie per tutto quello che mi avete insegnato: mi ha permesso di essere la persona che sono.

Ora finalmente si chiude il cerchio... chissà cosa riserverà il futuro...
una cosa è certa: *tüt cos va par sò pé!*